THE ENVIRONMENTAL IMPACT OF HIGH- AND LOW-MASS STARS: FROM FORMATION TO MAIN SEQUENCE

BY

IAN WILLIAM STEPHENS

DISSERTATION

Submitted in partial fulfillment of the requirements
for the degree of Doctor of Philosophy in Astronomy
in the Graduate College of the
University of Illinois at Urbana-Champaign, 2013

Urbana, Illinois

Doctoral Committee:

Associate Professor Leslie W. Looney, Chair
Professor You-Hua Chu
Professor Emeritus Richard M. Crutcher
Associate Professor Tony Wong

Abstract

Throughout the entire lifetime of a star, it continuously alters the environment. Diverse processes are involved which complicates studies of stellar interaction. This thesis focuses on two different physical phenomena associated with stars: (1) the interplay of magnetic fields and collapsing clouds, and (2) the effects of radiation from massive stars. We first compare polarization measurements of 52 Galactic star-forming regions with their locations in the Galaxy. In particular, we find that there is no correlation between the average magnetic field direction of star-forming molecular clouds and the Galaxy, indicating that star formation may eventually become its own process independent of the Galaxy. Secondly, we observe the coupling of the magnetic field with the low-mass protostar L1157-mm by creating polarimetric maps at resolutions from ∼300 to 2500 AU. The inferred magnetic field lines show a well-defined hourglass morphology centered about the core – only the second of such morphology discovered around a low-mass protostar. Next, we focus on radiation from massive stars in the Large Magellanic Cloud. We first present a survey of H II regions around massive young stellar objects (YSOs) and explore numerous relationship between parameters measured through observations of free-free and infrared emission. In particular, we find that YSO mass is a crucial consideration when exploring almost any relationship. Finally, we analyze how massive stars process dust in two classical H II regions and two superbubbles. We find that PAH emission is highest in the presence of molecular clouds with a low radiation field and that emission from very small grains are particularly high at locations where the radiation field is very strong.

Table of Contents

List of Tables

List of Figures

Chapter 1

Introduction

The research presented herein includes a diverse study of molecular clouds, protostars, young stellar objects (YSOs), and massive stars. Since stars have many phases of development and depend strongly on their mass, they have a diverse interplay with their surrounding environments. However, the exact physics underlying the formation and environmental impact of stars is not clearly understood. Thus, observations are prudent in discerning what physical processes are important during a stars lifetime. For the study presented here, we primarily look at two facets concerning stars: (1) magnetic fields during the early stages of star formation, and (2) the impact of radiation due to massive YSOs and main sequence stars.

As observations have indicated, even before the onset of star formation, molecular clouds show structured magnetic field lines. As clouds collapse in the process of creating new stars, magnetic field lines often remain organized, coupling with the core. Given these observations, magnetic fields likely play a role in the star formation process. However, the importance of magnetic fields during the star formation process is controversial amongst the community. Two chapters concerning star formation and magnetic fields are presented in this research.

In Chapter 2, we investigate the effect of the Milky Way's magnetic field in star forming regions using archived 350 μm polarization data on 52 Galactic star formation regions from the Hertz polarimeter module. The polarization angles and percentages for individual telescope beams were combined in order to produce a large-scale average for each source and for complexes of sources. In more than 80% of the sources, we find a statistically significant mean magnetic field direction, implying the existence of an ordered magnetic field component at the scale of these sources. The average polarization angles were analyzed with respect to the Galactic coordinates in order to test for correlations between polarization percentage, polarization angle, intensity, and Galactic location. No correlation was found, which suggests that the magnetic field in dense molecular clouds is decoupled from the large-scale Galactic magnetic field. Finally, we show that the magnetic field directions in the complexes are consistent with a random distribution on the sky.

In Chapter 3, we present the first detection of polarization around the Class 0 low-mass protostar L1157-mm at two different wavelengths. We show polarimetric maps at large scales (10″ resolution at

350 μm) from the SHARC-II Polarimeter and at smaller scales (1.2″-4.5″ at 1.3 mm) from the Combined Array for Research in Millimeter-wave Astronomy (CARMA). The observations are consistent with each other and show that the inferred magnetic field lines are aligned with the outflow. The CARMA observations suggest a full hourglass magnetic field morphology centered about the core; this is only the second well-defined hourglass detected around a low-mass protostar to date. We apply two different methods to CARMA polarimetric observations to estimate the plane-of-sky magnetic field magnitude, finding values of 1.4 and 3.4 mG.

When discussing the environmental impact of stars, the more massive the star, the more impact it has on the environment. For stars above about 8 $M_{\odot}$, the formation processes and the stars interaction with their surroundings becomes considerably different from low-mass stars. Notably, massive stars have tremendous accretion rates, strong winds, and immense radiation capable of ionizing hydrogen and helium. Massive stars even have a drastically different ending – supernova explosions which dump heavy elements in the environment.

Well before a massive star finishes its accretion, hydrogen fusion begins and produces harsh photons. This YSO quickly ionizes the surrounding medium, producing H II regions. Throughout the rest of a massive star's lifetime, it will eventually create a larger H II region, often combining with other H II regions to produce a massive H II complex. The radiation of massive stars can also modify dust grain populations in a region through a variety of mechanisms. However, the importance of each mechanism depends on the conditions of the region, and observations can provide evidence of which processes are important. This study devotes two chapters analyzing the strong radiation of massive stars within H II regions.

In Chapter 4, we survey H II free-free emission at 3 and 6 cm around 102 spectroscopically confirmed young stellar objects (YSOs) in the Large Magellanic Cloud. From the *Spitzer Space Telescope*'s Infrared Spectograph and photometric observations, we have estimates of the evolutionary stage and mass of each YSO and can compare these values to observational parameters of the free-free emission. Based on mass estimates from SED fitting and ATCA detection limits, we find that most massive YSOs that were detected by Spitzer at 5.8 μm are in HII regions detectable with our ATCA data, regardless of age. H II regions associated with more embedded (i.e., likely younger) massive YSOs are much less likely to be resolved and are more dense than less embedded YSOs, indicating evolving H II regions. We also find indications that the YSO's H II region is likely better modeled by a prolate spheroid rather than a sphere. We find that YSO extended H II regions typically have dynamical ages $\geq 10^5$ yr, which is consistent with other studies. Additionally, we explore several other relationships between the spectral and free-free emission parameters and provide generalized fits of each comparison.

Finally in Chapter 5, we show how dust properties change across H II regions of the LMC. Massive stars can alter physical conditions and properties of their ambient interstellar dust grains via radiative heating and shocks. The H II regions in the LMC offer ideal sites to study the stellar energy feedback effects on dust because stars can be resolved, and the galaxy's nearly face-on orientation allows us to unambiguously associate H II regions with their ionizing massive stars. The *Spitzer* survey of the LMC provides multi-wavelength (3.6 to 160 μm) photometric data of all H II regions. To investigate the evolution of dust properties around massive stars, we have analyzed spatially-resolved IR dust emission from two classical H II regions and two simple superbubbles in the LMC. We produce photometric spectral energy distributions (SEDs) of numerous small subregions for each region based on its stellar distributions and nebular morphologies. We use `DustEM` dust emission model fits to characterize the dust properties. Color-color diagrams and model fits are compared with the radiation field (estimated from photometric and spectroscopic surveys). Strong radial variations of SEDs can be seen throughout the regions, reflecting the available radiative heating. Emission from very small grains drastically increases at locations where the radiation field is the highest, while PAHs appear to be destroyed. PAH emission is the strongest in the presence of molecular clouds, provided that the radiation field is low.

Chapter 2

The Galactic Magnetic Field's Effect in Star-Forming Regions

2.1 Introduction

Magnetic fields are known to play an important role in star formation (e.g., Mouschovias & Ciolek 1999; McKee & Ostriker 2007). The line-of-sight component of the magnetic field is often measured using the Zeeman effect or Faraday rotation (e.g., Crutcher et al. 2003). The angle of the magnetic field with respect to the plane of the sky can be deduced through continuum polarization measurements. Far-infrared continuum polarization is due to emission from elongated dust grains that align perpendicularly to the magnetic field (e.g., Hildebrand 1988). For the same reason, optical light that has undergone partial absorption by dust grains exhibits polarization parallel to the magnetic field (e.g., Davis & Greenstein 1951).

In general the magnetic field lines of the Milky Way follow the direction of the spiral arms (often measured via Faraday rotation of pulsar signals; e.g., Han et al. 2006). Since dust polarization vectors are orthogonal to magnetic field lines, the Galactic magnetic field should induce a tendency for mapped polarization angles to be perpendicular to the Galactic disk. External galaxies also show magnetic fields following the spiral arms (e.g., Sofue et al. 1986), but on small scales (about 20 pc in the case of NGC 6946) localized processes (e.g., star formation) dominate, tangling magnetic field lines (Beck 2007).

The 350 μm Hertz polarimeter module was located at the Caltech Submillimeter Observatory and operated from 1994 to 2003. The Hertz polarimeter was well-suited for polarization measurements that probe the dense environments around forming stars, specifically clumps and cores. Since the decommissioning of Hertz, Dotson et al. (2010) have published an archive of 56 different objects, 52 of which are Galactic star forming regions. In this paper, we use this relatively large data set of star-forming regions to calculate a single large-scale (up to an angular diameter of about 10 arcmin) average degree of polarization (P, percentage of wave that is polarized), position angle (θ), and flux density (I) for each of the 52 star-forming Hertz data

This chapter was previously published as "The Galactic Magnetic Field's Effect in Star-forming Regions" in the Astrophysical Journal as Stephens, I. W., Looney, L. W., Dowell, C. D., Vaillancourt, J. E., & Tassis, K. 2011, ApJ, 728, 99.

sets. The data are then explored to test whether the magnetic fields of these regions have any statistical relationship to the Galactic magnetic field.

Eritsian & Pogossian (1996) applied a similar analysis on visible polarization of 3000 stars (from the Mathewson & Ford 1970 data set) that are in the Galactic plane. They found that the measured optical polarization angles from most stars, particularly those at further distances, are parallel to the Galactic magnetic field. Fosalba et al. (2002) found that optical polarization measurements had a sinusoidal dependence with respect to Galactic longitude.

However, we note that the observations probe very different physical regions: submillimeter observations probe dense regions ($A_V \gtrsim 30$) while optical observations probe diffuse regions ($A_V \lesssim 5$). Although dust polarization of star formation regions has been compared to the Galactic plane magnetic field before, the studies have been limited to small sample sizes. Continuum polarimetry at $\lambda = 0.8$ and 1.3 mm of approximately 10 star formation sources (at scales of $\sim 1'$) revealed no correlation for the magnetic field direction with respect to the Galactic plane (Glenn et al. 1999). On the other hand, Li et al. (2006) analyzed the dust polarization of four giant molecular clouds (capturing most of the clouds on scales of $\sim 10'$) at 450 μm and found that three of these have a significant field aligned within 15° of the Galactic plane. Our data set probes similar regions, but we have a much larger sample size that will constrain, with much higher confidence, the relationship of the magnetic field to the Galactic plane.

Our results do not show any similar correlation for degree of polarization or angle with Galactic location. An in-depth analysis was applied for θ by binning data based on Galactic longitude and spiral arm locations, again suggesting no correlation.

This paper is organized as follows: in Section 2.2 we discuss our data and the analysis methods used. It also shows that a single polarization angle for each data set is typically meaningful. Our results are presented in Section 2.3 and discussed in Section 2.4.

2.2 Observational Data and Analysis

For the 52 analyzed Hertz data sets[1], there were an average of about 90 telescope beams per object. For each telescope beam, the following values were of interest: degree of polarization (P), polarization position angle (θ), flux density (I), and the uncertainties on each. Outliers were removed for measurements with $\sigma_\theta \geq 76°$, which is the 2σ point of a Gaussian distribution with a 90° full width at half maximum (most data sets have this or better). After these cuts, the average and median telescope beams per cloud were 82 and 56 respectively.

[1]Data available online (Dotson et al. 2010).

For each object, P, θ, and I values were used to calculate the Stokes parameters Q and U. These were then summed to find the large-scale average, converting back to mean Ps and θs. Uncertainties were propagated. A similar technique was used in Tassis et al. (2009). The mean angles were rotated from equatorial to Galactic coordinates.

2.2.1 Stokes Parameters, Ps, and θs

Since we are not able to measure circular polarization with Hertz, the Stokes parameter V is assumed to be 0; it is expected to actually be near this value. Circular polarization is also not relevant for average field direction. From I_i, P_i, and θ_i, measured at a beam location (i) in a source map, the following formulae were used to find the corresponding Q_i and U_i.

$$Q_i = I_i P_i \cos 2\theta_i \tag{2.1}$$

$$U_i = I_i P_i \sin 2\theta_i \tag{2.2}$$

From here, unweighted sums of Q_i and U_i were calculated in order to obtain $Q_{\text{tot}} = \sum Q_i$ and $U_{\text{tot}} = \sum U_i$. Similarly, an unweighted sum for intensity, $I_{\text{tot}} = \sum I_i$, was found. These quantities are not weighted by standard deviation and represent the sums as if the clouds were observed with a larger telescope beam.

By using error propagation to calculate σ_{Q_i} and σ_{U_i}, it is found:

$$\sigma_{Q_i}^2 = (P_i \sigma_{I_i} \cos 2\theta_i)^2 + (I_i \sigma_{P_i} \cos 2\theta_i)^2 + (2 I_i P_i \sigma_{\theta_i} \sin 2\theta_i)^2, \tag{2.3}$$

$$\sigma_{U_i}^2 = (P_i \sigma_{I_i} \sin 2\theta_i)^2 + (I_i \sigma_{P_i} \sin 2\theta_i)^2 + (2 I_i P_i \sigma_{\theta_i} \cos 2\theta_i)^2, \tag{2.4}$$

The variances for Q_{tot} and U_{tot} were found by summing the variances of each beam measurement:

$$\sigma_{Q_{\text{tot}}}^2 = \sum_{i=1}^{n} \sigma_{Q,i}^2. \tag{2.5}$$

This method of calculating the standard deviation accounts for errors due to measurement in uncorrelated linear data sets. The variance for I_{tot} was calculated similarly.

From Q_{tot}, U_{tot}, and I_{tot}, $\langle P \rangle$ and $\langle \theta \rangle$ can now be calculated. $\langle P \rangle$ is seen below:

$$\langle P \rangle = \frac{\sqrt{(Q_{\text{tot}})^2 + (U_{\text{tot}})^2}}{I_{\text{tot}}}. \tag{2.6}$$

The calculation of $\langle \theta \rangle$ is more complicated. $\langle \theta \rangle$ must always be positive, and the arctangent term does

not discriminate on which Qs and Us are negative. The following formulae successfully determine the proper $\langle\theta\rangle$:

$$\langle\theta\rangle' = \begin{cases} 0.5 \arctan \frac{U_{\rm tot}}{Q_{\rm tot}} & : \arctan \frac{U_{\rm tot}}{Q_{\rm tot}} \geq 0 \\ 0.5 \left(\pi + \arctan \frac{U_{\rm tot}}{Q_{\rm tot}}\right) & : \arctan \frac{U_{\rm tot}}{Q_{\rm tot}} < 0 \end{cases} \tag{2.7}$$

$$\langle\theta\rangle = \begin{cases} \langle\theta\rangle' & : U_{\rm tot} \geq 0 \\ \langle\theta\rangle' + \pi/2 & : U_{\rm tot} < 0. \end{cases} \tag{2.8}$$

In order to calculate the variances for $\langle P\rangle$ and $\langle\theta\rangle$, propagation of error was used again:

$$\sigma^2_{\langle P\rangle} = \frac{Q^2_{\rm tot}\sigma^2_{Q_{\rm tot}} + U^2_{\rm tot}\sigma^2_{U_{\rm tot}}}{I^2_{\rm tot}(Q^2_{\rm tot} + U^2_{\rm tot})} + \frac{(Q^2_{\rm tot} + U^2_{\rm tot})\sigma^2_{I_{\rm tot}}}{I^4_{\rm tot}} \tag{2.9}$$

$$\sigma^2_{\langle\theta\rangle} = \frac{Q^2_{\rm tot}\sigma^2_{U_{\rm tot}} + U^2_{\rm tot}\sigma^2_{Q_{\rm tot}}}{4(Q^2_{\rm tot} + U^2_{\rm tot})^2}. \tag{2.10}$$

It is important to note that Equations (3), (4), (9), and (10) do not incorporate the non-diagonal (correlation) terms of covariance matrices, which are necessary for proper propagation of error. The Dotson et al. (2010) data sets do not report correlation terms from their original coordinate transformation of I, Q, and U to P and θ. Additionally, other correlation terms exist, such as observational correlations and correlations between adjacent beams. More accurate calculations of uncertainties are not motivated for the analysis and conclusions of this paper, but it should be noted that without the correlation terms, uncertainties are approximate.

Our results for a large-scale average are consistent with the polarimetric maps in Dotson et al. (2010). Although de-biasing $\langle P\rangle$, as discussed by Vaillancourt (2006), is an important part in the analysis of $\langle P\rangle$ implied by $\sigma_{\langle P\rangle}$, it was not done on these data since it does not modify the polarization angle (the primary focus for results in this paper).

The Hertz averages were analyzed in three ways: (1) investigating each of the 52 Hertz sources separately; (2) separating the sources by Galactic arm; and (3) combining nearby databases (i.e., data within 5° in Galactic longitude and less than 200 pc apart along the line of sight). The last technique reduces the amount of total data sets to 22 "complexes."

2.2.2 Mean Angle Significance

To investigate whether a meaningful mean direction of the magnetic field exists or whether, instead, angles in the Hertz data sets are random (follow a uniform angle distribution) we used a Kolmogorov–Smirnov (K-S) test. Out of the 52 data sets, 42 were inconsistent with a random distribution of angles at a 90% confidence level. By looking at the polarimetric maps in Dotson et al., the 10 data sets that exhibited a scatter consistent with a random distribution were maps that had poor signal-to-noise or had "circular-like" morphology (e.g., W75N). In this paper, our analysis was conducted in three ways: keeping these 10 data sets, omitting these datasets, and analyzing these data sets by themselves. In all cases, we arrived at consistent conclusions.

Similarly, for the 22 complexes, 17 were inconsistent with a random distribution of angles at a 90% confidence level. Thus, the data have a meaningful large-scale average angle that is inconsistent with random processes for >80% of the sources and >77% of the complexes with 90% confidence.

A similar conclusion can also be obtained by using the normalized Stokes parameters[2]:

$$q' = \cos 2\theta \,, \tag{2.11}$$

$$u' = \sin 2\theta \,. \tag{2.12}$$

The values of the normalized Stokes parameters q' and u' at each pointing position within a cloud must be in the range [−1,+1]. Random samples drawn from a uniform distribution of angles should have an average q' and u' of 0. With a finite number of samples we can only expect that average to reach zero within some uncertainty. With approximately 56 samples per cloud, from a uniform distribution of angles we expect $\langle q' \rangle$ approximately 0 ± 0.09. For the Hertz sample of 52 clouds, $\langle q' \rangle$ and $\langle u' \rangle$ are in the range -0.90 to 0.74, significantly above the expectations for a uniform distribution of angles.

When taking the averages of the magnitudes of $\langle q' \rangle$ and $\langle u' \rangle$ for the clouds and complexes, a similar argument holds. We define $q_{\rm cloud} = \langle |\langle q' \rangle| \rangle$ and $u_{\rm cloud} = \langle |\langle u' \rangle| \rangle$ (i.e., the average magnitudes of $\langle q' \rangle$ and $\langle u' \rangle$) for the 52 clouds. The uncertainty due to the finite sample of 52 clouds is slightly increased from the previous paragraph. That is, for a uniform random distribution of angles we expect $q_{\rm cloud}$ and $u_{\rm cloud}$ to have a standard deviation of 0.10. The actual values for our data set are $q_{\rm cloud} = 0.284$ and $u_{\rm cloud} = 0.322$, significantly larger than what could be expected from a uniform random distribution. For the 22 complexes a uniform distribution gives a standard deviation of 0.15. The actual values for our data set are $q_{\rm complex} = 0.196$ and $u_{\rm complex} = 0.226$, which are both significant at an 80% confidence level.

[2]The primes denote the difference between the typical definition of normalized Stokes parameters, i.e., $q = Q/I$ and $u = U/I$.

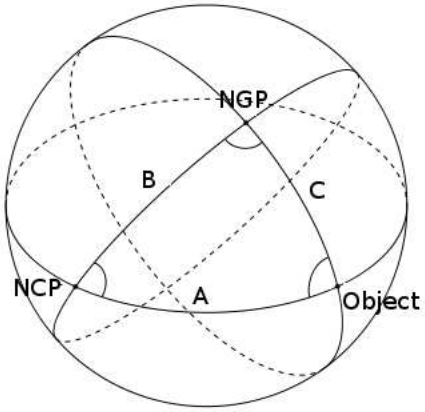

Figure 2.1 Spherical trigonometry required to convert equatorial position angles θ into Galactic position angles $\langle\theta_G\rangle$.

2.2.3 The Equatorial to Galactic Angle Transformation

In order to compare the average magnetic field of star-forming clouds to the Galactic magnetic field, we must convert the equatorial position angles (measured east from the north celestial pole (NCP)) to Galactic position angles (measured toward increasing longitude from the NGP). This conversion makes use of Galactic coordinates l and b. The location of the NCP (B1950) is exactly $l_n = 123^\circ$ and $b_n = 27.^\circ4$. By definition, the NGP is at $b_{\rm ngp} = 90^\circ$.

Let l_1 and b_1 be the location of an individual object. The rotation of the equatorial angle θ into a Galactic angle θ_G is simply the angle created at the object by lines from the NGP and NCP, as shown in Figure 2.1, $\angle$Object ($\angle O$). We see that the angle of arc B is always $b_{\rm ngp} - b_n = 90^\circ - 27.^\circ4 = 62.^\circ6$. Similarly, arc C is $90^\circ - b_1$, but it is unimportant with knowledge of the declination. $\angle$NGP is $l_n - l_1$. From the law of cosines, we could use B and C to find arc A, but this is simply 90° minus the B1950 declination, δ. Therefore, $A = 90^\circ - \delta$. Now, from the law of sines we can derive an equation for $\angle$O:

$$\frac{\sin\angle O}{\sin B} = \frac{\sin\angle{\rm NGP}}{\sin A} \tag{2.13}$$

$$\angle O = \arcsin\left[\frac{\sin(123 - l_1)\sin 62.^\circ6}{\sin(90^\circ - \delta)}\right] \tag{2.14}$$

$$\langle\theta_G\rangle = \angle O + \langle\theta\rangle, \tag{2.15}$$

where $\angle$O will either be positive or negative and is added to $\langle\theta\rangle$ to get the Galactic polarization angle,

$\langle\theta_G\rangle$. Since polarization vectors are "headless" (have no preferred direction), 180° is added or subtracted to the final value to make $\langle\theta_G\rangle$ between 0° and 180°. Databases such as Mathewson & Ford (1970) and Klare & Neckel (1977) have used this standard in the past, and this rotation method agrees with those databases to the tenth of a degree.

2.3 Results

In this section we present an extensive examination of possible correlations between Galactic coordinates (l and b), degree of polarization ($\langle P\rangle$), Galactic polarization angle ($\langle\theta_G\rangle$; transformation from $\langle\theta\rangle$ is discussed in Section 2.2.3), and intensity ($\langle I\rangle$). Section 2.3.1 focuses on correlations with Galactic coordinates. Section 2.3.2 bins data based on Galactic arms. In both cases no relationship between location and $\langle\theta_G\rangle$ was established. Table 1 shows the data for each individual object and its associated complex; note that large clouds (e.g., OMC-1 for the fourth complex in Table 1) may be dominant for the calculated Galactic angle for a complex. Table 2 summarizes the coefficient of determination (i.e., the square of the Pearson product–moment correlation coefficient), R^2, for most of the comparisons done. Finally, Section 2.3.3 examines correlation orthogonal to the Milky Way's magnetic field.

Table 2.1. Galactic Star-Forming Regions Observed with Hertz

Source[a]	α (2000) (h:m:s)	δ (2000) (d:m:s)	l (deg)	b (deg)	$\langle I \rangle$ (Jy)	$\sigma_{\langle I \rangle}$ (Jy)	$\langle P \rangle$ (%)	$\sigma_{\langle P \rangle}$ (%)	$\langle \theta \rangle$ (deg)	$\langle \theta_G \rangle$ (deg)	$\sigma_{\langle \theta \rangle}$ (deg)	$\langle \theta_G \rangle^{\rm b}_{\rm co}$ (deg)	$\sigma^{\rm b}_{\langle \theta \rangle_{\rm co}}$ (deg)	Spiral Arm	Dist.[c] (kpc)
W3[1]	02:25:40.7	62:05:52	133.71	1.22	142.1	1.3	0.69	0.04	71.4	50.9	1.8	50.9	1.8	Perseus	1.95±0.04(1)
NGC 1333[2]	03:29:03.7	31:16:03	158.35	–20.56	19.8	0.3	0.36	0.43	84.9	48.1	34.3	48.1	34.3	Local	0.318±0.027(2)
L1551[3]	04:31:34.2	18:08:05	178.93	–20.05	17.2	1.6	1.23	0.62	41.6	170.9	14.3	170.9	14.3	Local	0.14±0.01(3)
IRAS 05327–0457[4]	05:35:14.4	–04:57:38	208.57	–19.18	19.3	0.2	3.02	0.28	143.3	80.6	2.1	143.6	0.2	Local	0.4(4)
OMC-1[4]	05:35:14.5	–05:22:32	208.99	–19.38	213.7	1.1	1.86	0.01	27.6	144.8	0.2			Local	0.4(4)
OMC-2[4]	05:35:26.7	–05:10:00	208.82	–19.25	56.8	0.7	0.54	0.05	138.8	76.1	2.7			Local	0.4(4)
OMC-3[4]	05:35:23.5	–05:01:32	208.68	–19.19	42.5	0.1	1.72	0.07	135.6	72.9	1.3			Local	0.4(4)
OMC-4[4]	05:35:08.2	–05:35:56	209.19	–19.51	24.0	2.7	1.13	0.17	167.7	104.8	4.3			Local	0.4(4)
L1641N[4]	05:36:18.8	–06:22:11	210.06	–19.59	24.2	1.9	0.66	0.24	36.3	153.1	10.1			Local	0.4(4)
NGC 2023[5]	05:41:25.4	–02:18:06	206.86	–16.60	19.1	3.8	1.30	0.35	129.1	67.0	7.8	84.4	1.6	Local	0.4(4)
NGC 2024[5]	05:41:43.0	–01:54:22	206.53	–16.36	174.2	2.4	0.51	0.03	154.8	92.8	1.8			Local	0.4(5)
HH24MMS[5]	05:46:08.4	–00:10:43	205.49	–14.57	10.8	1.2	1.19	0.45	90.5	28.8	10.8			Local	0.4(5)
NGC 2068 LBS 17[5]	05:46:28.0	–00:00:54	205.38	–14.42	8.2	0.4	0.76	0.35	49.0	167.4	13.2			Local	0.4(5)
NGC 2068 LBS 10[5]	05:46:50.2	00:02:01	205.38	–14.32	16.8	0.4	3.24	0.14	128.2	66.5	1.2			Local	0.4(5)
NGC 2071[5]	05:47:04.8	00:21:47	205.11	–14.11	44.1	1.0	0.46	0.07	147.4	85.9	4.6			Local	0.4(5)
Mon R2[6]	06:07:46.6	06:23:16	213.71	–12.60	140.8	3.7	0.59	0.04	30.7	147.4	1.8	164.9	2.5	Local	0.83±.05(6)
GGD12[6]	06:10:50.4	–06:11:46	213.88	–11.84	95.0	3.6	0.86	0.07	90.8	27.6	2.2			Local	1(7)
S269[7]	06:14:36.6	13:49:35	196.45	–1.68	18.8	2.1	1.76	0.46	37.1	155.9	7.4	155.9	7.4	Perseus	3.8(8)
AFGL 961[8]	06:34:37.7	04:12:44	207.27	–1.81	10.7	1.0	1.14	0.36	160.9	98.6	9.0	98.6	9.0	Perseus	1.7(9)
Mon OB1 27[9]	06:40:58.3	10:36:54	202.30	2.53	5.8	0.7	0.52	0.46	157.0	94.4	24.9	56.4	3.7	Local	0.8(10)
Mon OB1 25[9]	06:41:03.7	10:15:07	202.63	2.38	16.5	4.1	1.93	0.67	116.8	54.2	9.8			Local	0.8(10)
Mon OB1 12[9]	06:41:06.1	09:34:09	203.24	2.08	21.6	0.1	1.42	0.14	138.7	76.1	2.9			Local	0.8(10)
NGC 2264[9]	06:41:10.3	09:29:27	203.32	2.06	64.6	1.1	0.57	0.04	81.1	18.6	2.2			Local	0.8(10)
ρ Oph[10]	16:26:27.5	–24:23:54	353.08	16.91	46.6	4.0	1.24	0.07	161.0	29.4	1.6	27.1	2.2	Local	0.139±0.006(11)
IRAS 16293–2422[10]	16:32:22.8	–24:28:36	353.94	15.84	33.9	0.1	0.41	0.12	90.4	139.6	8.1			Local	$0.178^{+0.018}_{-0.037}$(12)
CB68[11]	16:57:19.5	16:09:21	4.50	16.34	3.8	0.5	0.51	0.34	55.9	110.2	19.1	110.2	19.1	Local	0.16(13)
NGC 6334V[12]	17:19:57.4	–35:57:46	351.16	0.70	193.9	7.0	0.21	0.05	105.9	160.7	6.2	100.0	1.1	Sagittarius	1.74±0.31(14)

Table 2.1 (cont'd)

Source[a]	α (2000) (h:m:s)	δ (2000) (d:m:s)	l (deg)	b (deg)	$\langle I \rangle$ (Jy)	$\sigma_{\langle I \rangle}$ (Jy)	$\langle P \rangle$ (%)	$\sigma_{\langle P \rangle}$ (%)	$\langle \theta \rangle$ (deg)	$\langle \theta_G \rangle$ (deg)	$\sigma_{\langle \theta \rangle}$ (deg)	$\langle \theta_G \rangle^{b}_{co}$ (deg)	$\sigma^{b}_{\langle \theta \rangle_{co}}$ (deg)	Spiral Arm	Dist.[c] (kpc)
NGC 6334A[12]	17:20:19.1	–35:54:45	351.25	0.67	187.0	2.8	1.19	0.04	68.8	123.6	1.1			Sagittarius	1.74±0.31(14)
NGC 6334I[12]	17:20:53.4	–35:47:00	351.42	0.65	487.8	7.2	0.70	0.03	36.5	91.4	1.2			Sagittarius	1.74±0.31(14)
M-0.13-0.08[13]	17:45:37.3	–29:05:40	359.87	–0.08	156.5	3.6	0.86	0.06	107.1	165.4	2.0	140.9	0.9	Gal. center	8(15)
Sgr A East[13]	17:45:41.5	–29:00:09	359.95	–0.05	132.3	1.2	1.12	0.03	92.1	150.4	0.8			Gal. center	8(15)
CO 000.02-00.02[13]	17:45:42.1	–28:56:05	0.01	–0.01	139.7	5.8	1.08	0.03	53.5	111.8	0.7			Gal. center	8(15)
M-0.02-0.07[13]	17:45:51.6	–28:59:09	359.99	–0.07	127.0	2.8	1.96	0.10	80.9	139.3	1.4			Gal. center	8(15)
M+0.07-0.08[13]	17:46:04.3	–28:54:45	0.07	–0.07	82.3	3.0	0.58	0.08	37.5	95.8	3.9			Gal. center	8(15)
M+0.11-0.08[13]	17:46:10.2	–28:53:06	0.11	–0.08	144.8	4.6	0.09	0.05	132.2	10.5	16.9			Gal. center	8(15)
M+0.25+0.01[13]	17:46:10.5	–28:42:17	0.26	0.02	135.9	11.8	0.36	0.06	93.5	151.9	4.7			Gal. center	8(15)
M+0.34+0.06[13]	17:46:13.2	–28:36:53	0.34	0.05	87.5	3.8	1.02	0.11	42.5	100.9	3.1			Gal. center	8(15)
Sickle (G0.18-0.04)[13]	17:46:14.9	–28:48:03	0.19	–0.05	99.9	9.7	1.48	0.23	114.8	173.2	4.5			Gal. center	8(15)
M+0.40+0.04[13]	17:46:21.4	–28:35:41	0.38	0.04	75.2	2.1	1.11	0.13	160.2	38.6	3.4			Gal. center	8(15)[d]
Sgr B1[13]	17:46:47.2	–28:32:00	0.48	–0.01	172.5	4.1	1.00	0.04	128.4	6.9	1.1			Gal. center	8(15)
Sgr B2[13]	17:47:20.2	–28:23:06	0.67	–0.04	1013.2	3.5	0.36	0.01	77.1	135.6	1.0			Gal. center	8(15)
W33 C (G12.8-0.2)[14]	18:14:13.4	–17:55:32	12.81	–0.20	206.3	2.3	0.21	0.03	41.7	102.9	4.3	114.0	26.2	Scutum-Crux[e]	4.5(16)
W33 A[14]	18:14:38.9	–17:52:04	12.91	–0.26	83.5	1.7	0.57	0.07	129.1	10.3	3.4			Scutum-Crux[e]	4.5(16)
L483[15]	18:17:29.8	–04:39:38	24.88	5.38	9.2	0.3	0.32	0.19	163.3	45.1	16.8	45.1	16.8	Local	0.2(17)
M 17[16]	18:20:24.5	–16:13:02	15.01	–0.69	276.3	5.6	0.82	0.02	164.0	45.6	0.8	45.6	0.8	Sagittarius	$1.6^{+0.3}_{-0.1}$(18)
W43-MM1[17]	18:47:46.9	–01:54:29	30.82	–0.06	154.3	4.4	0.80	0.17	178.9	61.4	6.1	61.4	6.1	Scutum-Crux[f]	7.0±0.9(19)
G34.3+0.2[18]	18:53:18.5	01:14:59	34.26	0.15	206.6	15.6	0.51	0.16	109.3	171.9	8.8	171.9	8.8	Scutum-Crux[g]	3.7(20)
W49 A[19]	19:10:13.6	09:06:17	43.17	0.01	153.1	5.7	0.45	0.03	56.7	119.0	2.0	119.0	2.0	Perseus	11.4±1.2(21)
W51 A (G49.5-0.4)[20]	19:23:44.0	14:30:32	49.49	–0.39	241.8	1.3	0.47	0.02	44.2	105.7	0.9	105.7	0.9	Sagittarius[h]	7±1.5(22)
IRAS 20126+4104[21]	20:14:29.4	41:13:34	78.13	3.62	16.6	1.6	0.49	0.37	33.0	89.2	21.4	89.2	21.4	Local	1.5±0.5(23)
W75 N[22]	20:38:36.4	42:37:35	81.87	0.78	158.8	4.1	0.22	0.09	80.0	132.3	11.0	61.1	1.0	Local[i]	2–3(24)(25)
DR21[22]	20:39:01.0	42:19:31	81.68	0.54	131.0	3.2	1.05	0.03	8.0	60.2	0.8			Local[i]	2–3(24)(25)

Note. — Angles given represent the *E*-field. 8 kpc was quoted for objects in Galactic Center.

[a] Numeric exponents denote the "complex" groupings for each source.

[b] $\langle \theta_G \rangle$ and uncertainties for the object's associated complex. Values listed only once for each complex.

[c] Distances are from (1) Xu et al. 2006; (2) de Zeeuw et al. 1999; (3) Kenyon et al. 1994; (4) Menten et al. 2007; (5) Anthony-Twarog 1982; (6) Herbst & Racine 1976; (7) Rodriguez et. al. 1982; (8) Moffat et. al. 1979; (9) Park & Sung 2002; (10) Walker 1956; (11) Mamajek 2008; (12) Imai et al. 2007; (13) Launhardt & Henning 1997; (14) Neckel 1978; (15) distances for objects in the Galactic center were all taken to be 8 kpc; (16) Helfand et al. 2007; (17) Dame & Thaddeus 1985; (18) Povich et al. 2007; (19) Wilson et al. 1970; (20) Wink et al. 1983; (21) Gwinn et al. 1992; (22) Genzel et al. 1981; (23) Shinnaga et al. 2008; (24) Campbell et al. 1982; and (25) Odenwald & Schwartz 1993.

[d] Kinematic distance is reported to be 10.0 kpc by (Walsh et al. 1997), but 8 kpc was adopted here.

[e] Uncertainties may place these objects in the near 3 kpc arm.

[f] Uncertainties may place this object in the far 3 kpc arm or the long bar.

[g] Uncertainties may place this object in the outer arm.

[h] Uncertainties may place this object in the Perseus arm.

[i] There is much discussion on the exact distance to these objects. Uncertainties may place these objects just outside Local arm toward the Perseus arm.

Table 2.2. Correlation Values for Comparisons

R^2 Comparison[a]	All Data	Complexes	$-9 < l < 82$	$196 < l < 214$	Gal. Center	Local Arm
$\langle\theta_G\rangle$ vs. l	<0.01	0.06	<0.01	<0.01	0.12	<0.01
$\langle\theta_G\rangle$ vs. b	<0.01	0.13	<0.01	0.04	0.05	0.04
$\langle P\rangle$ vs. l	0.12	0.23	0.06	0.02	0.08	0.11
$\langle P\rangle$ vs. b	0.09	0.07	<0.01	<0.01	<0.01	0.08
$\langle I\rangle$ vs. l	0.16	0.23	0.02	0.18	0.36[b]	<0.01
$\langle I\rangle$ vs. b	0.02	<0.01	0.10	0.08	<0.01	0.02
$\langle\theta_G\rangle$ vs. $\langle I\rangle$	0.02	0.02	0.03	0.03	0.02	0.03
$\langle\theta_G\rangle$ vs. $I_{\rm tot}$	0.02	0.06	0.01	0.09	0.02	0.05
$\langle P\rangle$ vs. $\langle I\rangle$	0.06	0.04	0.03	0.04	0.13	0.01
$\langle P\rangle$ vs. $I_{\rm tot}$	<0.01	<0.01	0.02	0.01	0.12	0.03

Note. — For the reported comparisons, $\langle\theta_G\rangle$'s were kept between 0° and 180°. Values of Galactic coordinate l that were above 350° were made negative.

[a]Values for each comparison are the Pearson product–moment correlation coefficient, R^2.

[b]Sgr B2 has a very large intensity that is a definite outlier. Removing it causes R^2 to decrease to 0.04.

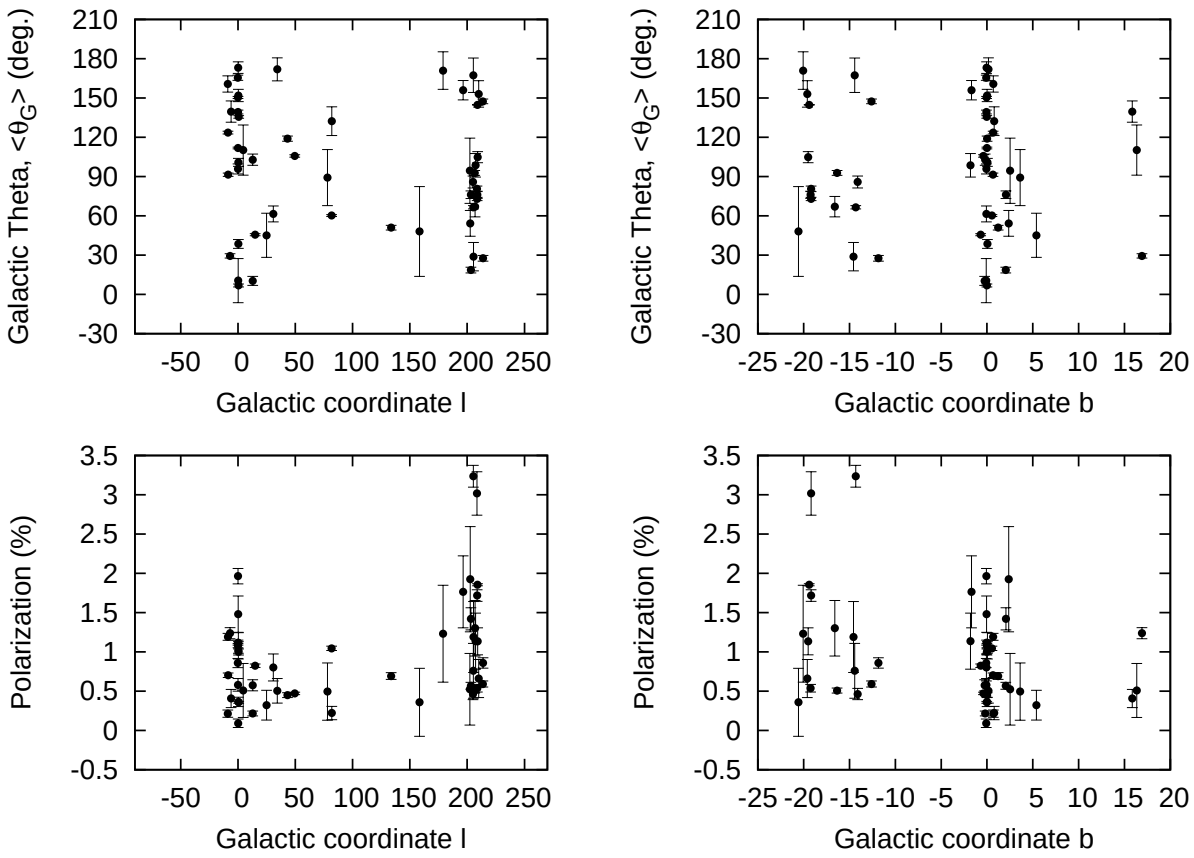

Figure 2.2 $\langle\theta_G\rangle$ and polarization versus Galactic coordinates, all data. Error bars are 1σ.

2.3.1 Polarization and Position Angles Versus Galactic Coordinates

Figure 2.2 shows four scatter plots for the 52 Galactic Hertz data sets: polarization and $\langle\theta_G\rangle$ versus both Galactic coordinates. There is no correlation in these graphs. As expected, in plots involving the Galactic latitude b, most objects cluster around $|b| \sim 0°$, as clouds lie within the Galactic plane. Those with values of b that are not near 0° are all objects in the Local arm (determination of spiral arm is discussed in Section 2.3.2). Note that polarization measurements with $\sigma_{\langle P\rangle} \geq \langle P\rangle$ are not significant.

There is a sufficient gap in data points between $l \simeq 82°$ and $l \simeq 196°$ as well as between $l \simeq 214°$ and $l \simeq 351°$. Binning data into the two prevalent set of points (i.e., around $l \simeq 0°$ and $l \simeq 200°$) still does not yield a correlation. Furthermore, analysis of $\langle\theta_G\rangle$ and $\langle P\rangle$ versus $\langle I\rangle$ and $I_{\rm tot}$ was made in attempt to see if brighter objects affect $\langle\theta_G\rangle$ and $\langle P\rangle$. No relationship was found here either.

Data were also separated into 22 complexes and analyzed in the same way as above. Figure 2.3 shows the same plots as Figure 2.2, but with the data sets reduced to 22 complexes. Again, no correlations were found in any of the relationships.

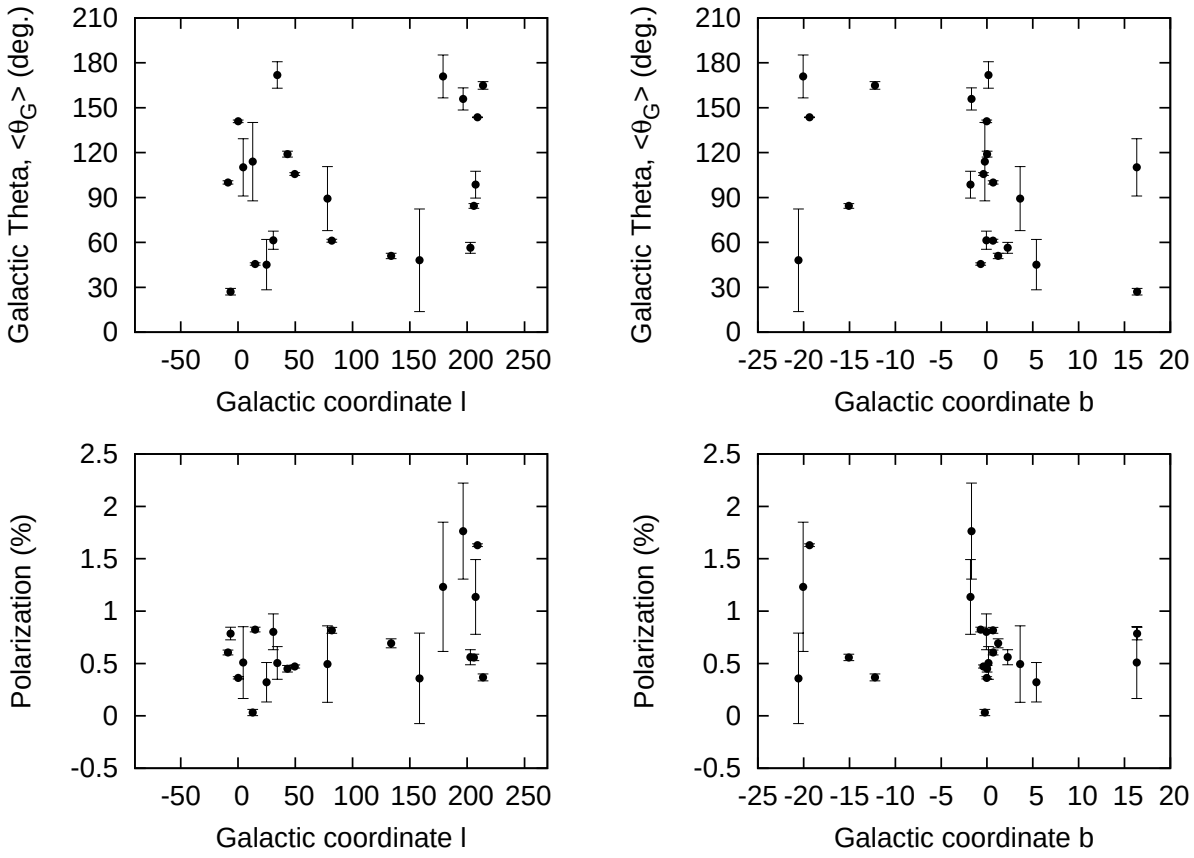

Figure 2.3 $\langle\theta_G\rangle$ and polarization vs. Galactic coordinates, complexes. Error bars are 1σ.

Table 2.3. Number of Objects Per Spiral Arm

Spiral Arm	Number of Hertz Clouds
Perseus	4
Local	27
Sagittarius	5
Scutum-Crux	4
Galactic center	12

2.3.2 Binning Galactic l According to Spiral Arms

The final attempt to find correlations between location and the resulting large-scale angle averages was to plot values based on the Galactic arm in which each object is located. In order to find the corresponding object and its relevant Galactic arm, knowledge of the distance to each object is required. We used SIMBAD to confirm that the distances found in the literature for each object (see Table 1) corresponded to the correct objects. By using a graphical grid of the Milky Way (Reid et al. 2009) and basic trigonometry from distances and Galactic coordinates l and b, the correct spiral arms were ascertained. Table 3 shows the approximate distribution of data contained within each spiral arm, while Table 1 indicates the corresponding spiral arm for each object. The spiral "arms" containing the most data points are the Local arm and the Galactic center. The arms with insufficient amounts of data were not thoroughly analyzed, though they seemed relatively random as well.

Once again, the same analysis as in Section 2.3.1 showed no significant correlations within spiral arm bins.

2.3.3 Area of Avoidance

The Galactic magnetic field is thought to follow the spiral arms. Along the line of sight, the electric field of the radiation will be orthogonal to the magnetic field, i.e., pointing toward the north Galactic pole (NGP). Since $\langle\theta_G\rangle$ is measured from the NGP, it is expected that a Galactic effect on the polarization would tend to point towards 0° and avoid 90° (i.e., orthogonal to the Milky Way's magnetic field). However, this trend is *not* seen in Figure 2.4. For both large and small polarization percentages, many objects lie very near or on top of this "area of avoidance".

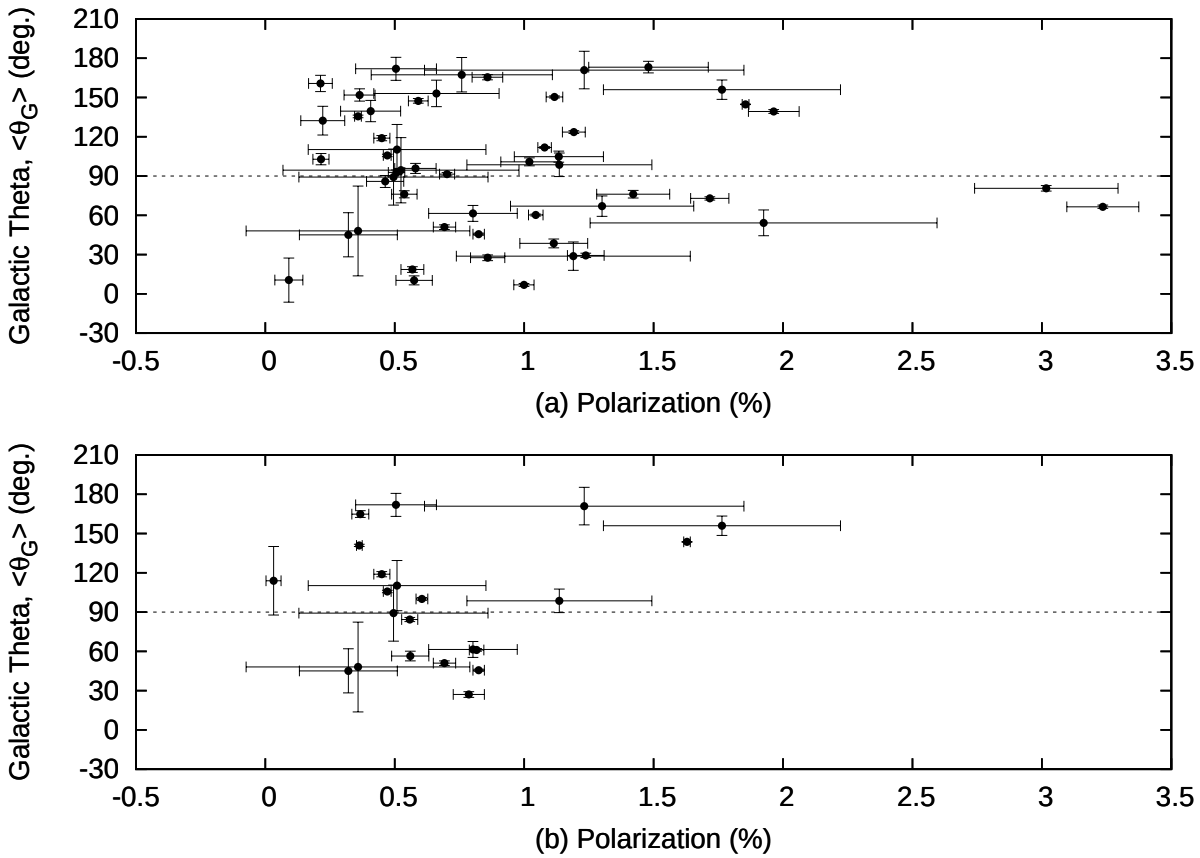

Figure 2.4 $\langle\theta_G\rangle$ vs. Polarization. (a) all data (b) complexes. Error bars are 1σ. The dashed line indicates the expected Galactic angle of avoidance at $\langle\theta_G\rangle = 90°$. It does not seem that the data try to avoid this particular angle.

2.3.4 Distribution of Polarization Angles

The Heiles catalog (Heiles 2000) has optical polarization measurements toward over 9000 stars. Those with $P > 0.2\%$ and distance >140 pc are seen in black in Figure 2.5. The inferred magnetic field vectors are shown in white for the 52 Hertz clouds in Figure 2.5(a) and the 22 Hertz complexes in Figure 2.5(b). For the most part, the submillimeter angles look randomly distributed; no obvious correlation can be seen with respect to the Galactic plane. While the B-vectors of the optical data tend to be parallel to the disk of the Galaxy, the submillimeter dust polarization in star-forming regions appears to have no directional preference. A detailed comparison of Hertz data to spatially co-located Heiles data is discussed in Li et al. (2009).

It should also be noted that polarimetric maps from $WMAP$, which are likely dominated by dust at 94 GHz, show dust magnetic field lines parallel to the Galactic magnetic field (Hinshaw et al. 2009).

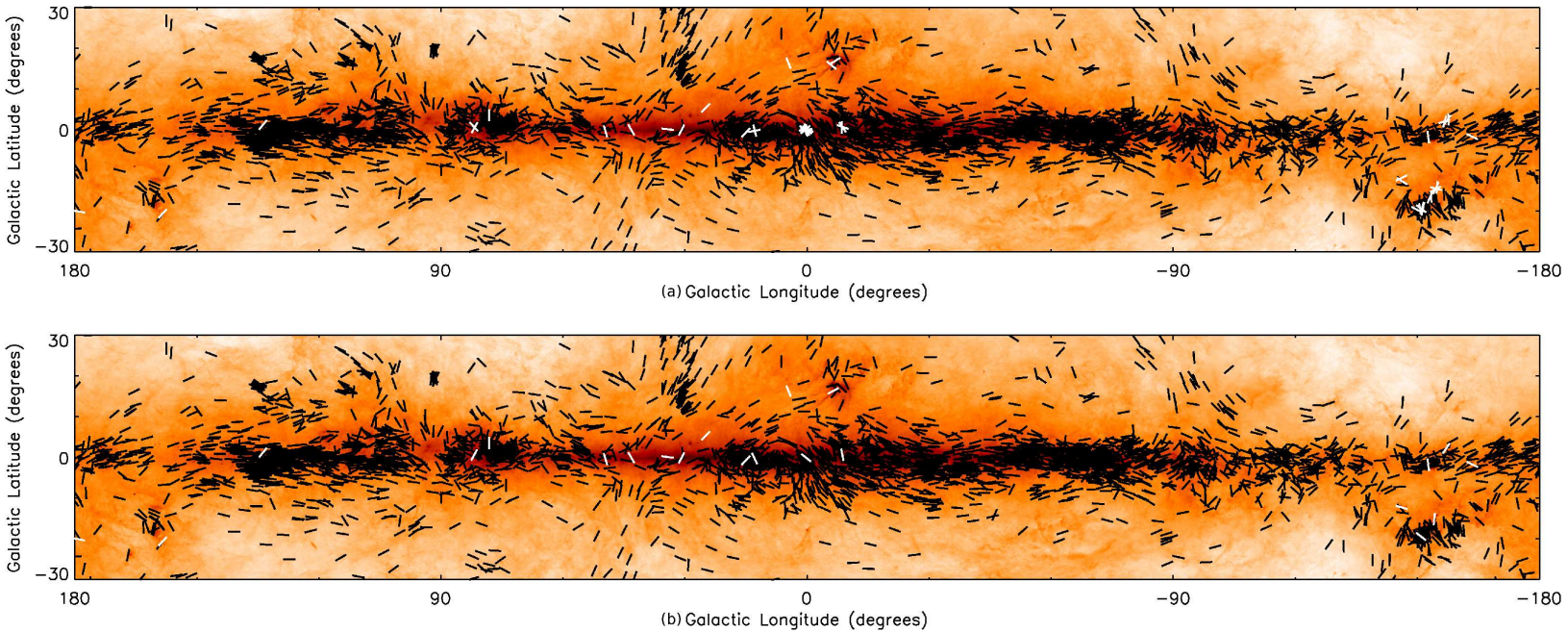

Figure 2.5 Inferred magnetic field orientations plotted in Galactic coordinates. Data from Hertz data sets (in white, with (a) all data; and (b) complexes) are shown along with background starlight polarization from the Heiles (2000) catalog (black lines, $P > 0.2\%$, distance > 140 pc). The gray scale shows the IRAS 100 μm intensity data on a logarithmic scale (Miville-Deschênes & Lagache 2005).

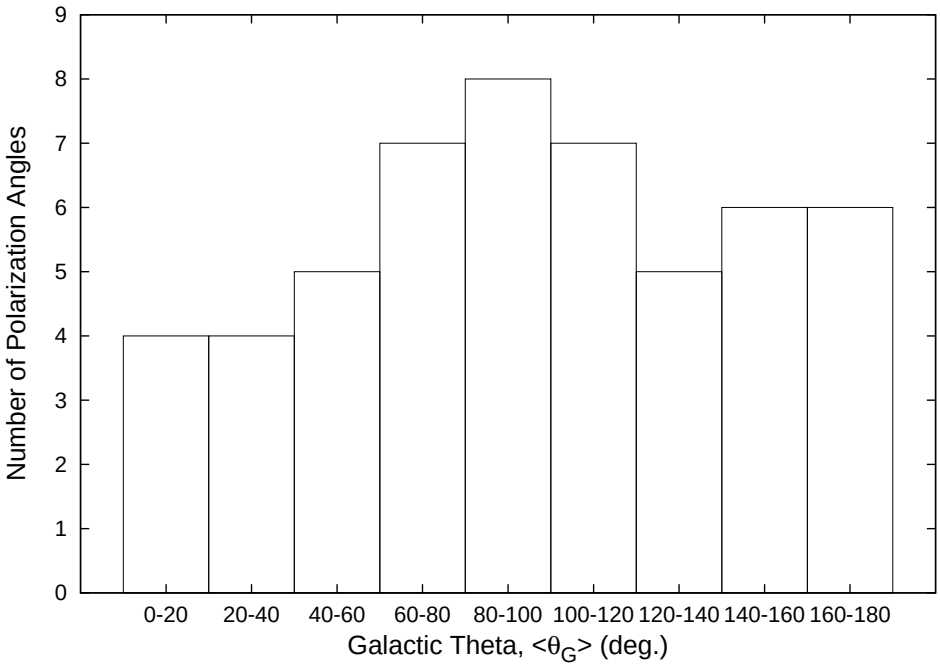

Figure 2.6 Histogram of polarization angles for the 52 data sets with 20° wide bins.

A histogram of $\langle\theta_G\rangle$ for all 52 data sets is seen in Figure 2.6 and on inspection appears consistent with a uniform distribution. A uniform distribution for angles between 0° and 180° has standard deviation of 52.°0. Table 4 summarizes results that test whether the sources and their complexes are uniform. The standard deviations are close to 52.°0. Rows 2 and 4 are perhaps more valid because these remove data sets that appeared "random" as discussed in Section 2.2.2. The K-S test was used to compare each distribution to a uniform distribution. The p-values of these tests are shown in Table 4; high p-value indicates consistency with a uniform distribution. Since all p-values are high, there is no preferred direction in the sky.

As a comparison to the distribution of Hertz angles, a histogram of the Heiles data with $P > 0.2\%$ and distance > 140 pc is shown in Figure 2.7. These cuts were chosen because all Hertz data sets except one (M+0.11-0.08 at $P = 0.09\%$) fit this criterion. There is overwhelming evidence that the data are a non-uniform distribution centered around a polarization position angle of 0°. Plotting Heiles angles without cuts show similar graphs. Additional filtering was done based on larger P and extinction cuts ($E(B-V)$ in the Heiles database) because these areas generally probe denser regions. These cuts tighten the distribution around 0°.

Table 2.4. Consistency with a Uniform Distribution

Data Analyzed	$\sigma_{\rm dist}$ (deg)	K-S Test P-value
All data sets (52)	48.6	0.69
K-S test accepted data sets (42)	47.7	0.69
All complexes (22)	45.5	0.28
K-S test accepted complexes (17)	47.5	0.51

Note. — The value in parentheses indicates the number of data sets.

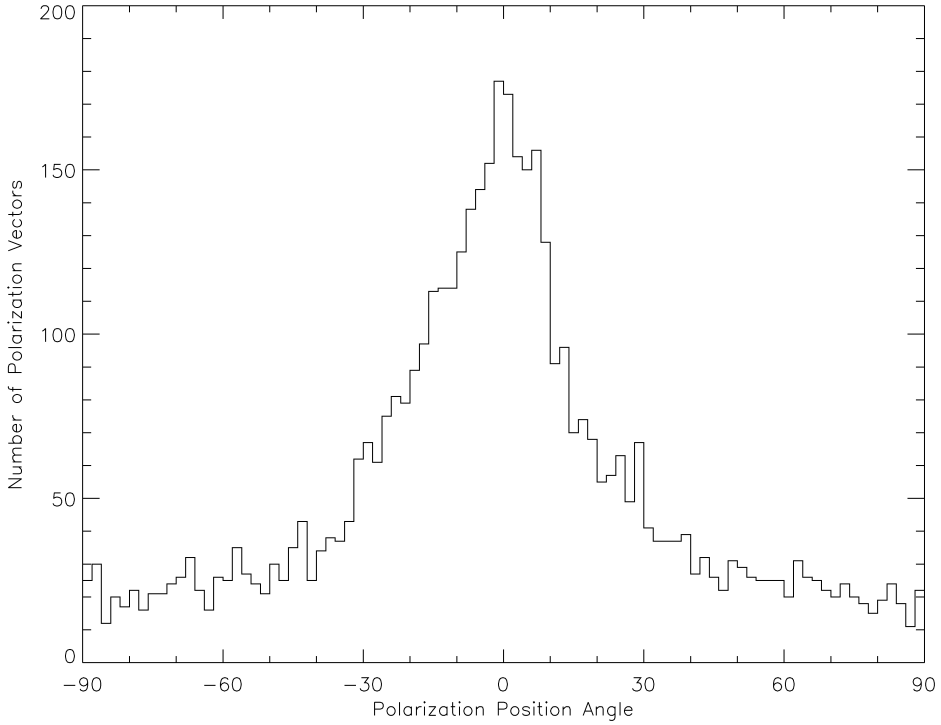

Figure 2.7 Histogram of Heiles polarization angles (with respect to Galactic coordinates) with $P > 0.2\%$ and distance > 140 pc.

2.4 Discussion and Conclusion

We have used Hertz (Dotson et al. 2010) polarization measurements in dense, star-forming clouds, to investigate whether the ordered component of the magnetic field in these clouds is correlated with location in the Galaxy. In order to obtain a single polarization percentage, angle, and intensity for each of the 52 Hertz objects (as well as the 22 complexes), the polarization information for each beam was combined into a large-scale average. With each object represented by these values, correlations with respect to location in the Galaxy (both by Galactic coordinates and spiral arm locations) were investigated.

There are three primary results for this paper.

- A meaningful polarization angle can be determined for most objects and complexes.
- No evidence was found in our data for a correlation between the polarization angle and location within the galaxy.
- The polarization angle for an object or a complex on the sky is consistent with a random distribution.

The fact that a meaningful mean direction can be identified for the magnetic field in most objects implies the existence of an ordered, large scale component of the field *within* the dense, star-forming clouds we have studied. This is consistent with the continuity of magnetic field direction on different scales within these clouds, discussed by Li et al. (2009). However, since these are star-forming clouds, feedback processes from newly formed stars can generate appreciable scatter in the magnetic field directions within each object. This may be, in part, the source of the observed angle dispersion within each data set.

We have found that there is no significant evidence for the existence of any correlation between mean polarization angle and location, which is consistent with the results by Glenn et al. (1999, see Section 2.1). The fact that objects do not seem to avoid polarization angles aligned with the Galaxy's magnetic field implies that the polarization angles detected are almost entirely created by the analyzed object rather than a large-scale, external field. This suggests that complexes as a whole may become their own dynamical system that is separate from the Galaxy. The results in this paper imply that cloud cores usually have a meaningful net field (which may correlate with other cores in the same complex; Li et al. 2009) that has no preferred direction within the Galaxy, yet are embedded in a diffuse medium in an ordered, Galactic large-scale field.

Fish et al. (2003) did a similar analysis as this paper, but with a different methodology. They analyzed the line-of-sight magnetic fields through Zeeman splitting of OH masers in massive star-forming regions; on sub-kiloparsec scales (about 0.5 kpc), two sources often had opposite line-of-sight field directions, suggesting

that multiple cores in a complex tangle the magnetic fields. In some areas of the Galaxy, Fish et al. found some line-of-sight field alignment in parts of the Sagittarius arm and Norma arm on scales of about 2 kpc. Still, they also found no evidence for correlations of magnetic field directions in star-forming regions with the Galactic field or with the spiral arms on larger scales.

The cloud formation process involves instabilities on Galactic scales (Shetty & Ostriker 2008; Mouschovias et al. 2009; Tasker & Tan 2009), which are responsible for the accumulation of enough mass to form the clouds. At the same time, these instabilities generate turbulence in the interstellar medium of the Galaxy. The cloud magnetic field is thus expected to decouple from the Galactic field during the cloud formation process. Stellar feedback is an additional mechanism driving the cloud magnetic field away from alignment with the Galactic field direction. These effects are likely responsible for the dichotomy between the arm/interarm regions in terms of the ratio of strengths between the ordered and tangled components of the magnetic field observed in external galaxies (Beck 2005).

Part of this work was carried out at the Jet Propulsion Laboratory, California Institute of Technology, under a contract with the National Aeronautics and Space Administration. This research has made use of the SIMBAD database, operated at CDS, Strasbourg, France. L.W.L. acknowledges support from the National Science Foundation under grant no. AST-07-09206. We also acknowledge Richard M. Crutcher for extensive discussions.

Chapter 3

The Magnetic Field Morphology of the Class 0 Protostar L1157-mm

3.1 Introduction

Alignment of dust grains by magnetic fields causes the thermal emission from dust to be polarized (e.g., Hildebrand 1988). The angles of dust polarization measurements at millimeter and submillimeter wavelengths are generally considered to be perpendicular to the magnetic field due to a number of alignment mechanisms (particularly radiative torques, Lazarian 2007), allowing for an estimate of the magnetic field direction in the plane of the sky.

Magnetic pressure can support clouds against collapse, though other processes, e.g., ambipolar diffusion, can allow gravity to eventually overwhelm magnetic support. The importance of magnetic fields in star formation is not well understood (e.g., weak- versus strong-field models, Crutcher 2012), but observations of the plane-of-sky magnetic field morphology can provide insight into the coupling of magnetic fields with cores, disks, and outflows. Although flux-freezing during gravitational collapse is expected to create an hourglass morphology in the magnetic field lines, there has only been one detection of a full hourglass around a low-mass protostar to date (e.g., Girart et al. 2006). However, several high-mass star formation regions have clear hourglass detections (e.g., Schleuning 1998; Girart et al. 2009; Tang et al. 2009).

Large, submillimeter surveys of various star-forming clouds and cores have been performed with single-dish polarimeters (e.g., Matthews et al. 2009; Dotson et al. 2010). The SHARC-II Polarimeter (SHARP, Li et al. 2008) at the Caltech Submillimeter Observatory, is one of the newer submillimeter polarimeters and allows for dual-beam (simultaneous observations of horizontal and vertical polarization components) polarimetric measurements.

Previous millimeter-wavelength interferometric polarimetric maps have been produced with the Berkeley-Illinois-Maryland Association, the Owens Valley Radio Observatory, and the Submillimeter Array (SMA)

This chapter was previously published as "The Magnetic Field Morphology of the Class 0 Protostar L1157-mm" in the Astrophysical Journal Letters as Stephens, I. W., Looney, L. W., Kwon, W., et al. 2013, ApJ, 769, L15.

(e.g., Girart et al. 2006; Kwon et al. 2006; Rao et al. 2009; Tang et al. 2010), but these observations only used single-polarization receivers modulated with a quarter-wave plate. The Combined Array for Research in Millimeter-wave Astronomy (CARMA) has recently installed 1 mm dual-polarization receivers; the first science observations in full-Stokes were made in 2011.

In this Letter we present polarimetric observations from SHARP and CARMA of the protostar L1157-mm in the dark cloud L1157. L1157-mm is a low-mass Class 0 source (i.e., the youngest of protostars) with a large bipolar outflow spanning about 5′ (Bachiller et al. 2001) and a perpendicular 2′ flattened envelope (Looney et al. 2007). Though the distance to the source is a bit uncertain, with estimates ranging from 200 to 450 pc (e.g., Kun 1998), we adopt a distance of 250 pc (Looney et al. 2007).

These observations trace the magnetic field structure within the core and throughout the infall envelope (which, given the adopted distance, could extend to 30″–40″) of L1157-mm. In this Letter we will examine how the continuum and the magnetic field morphologies correlate with other structures in L1157, such as its outflow and flattened core, and will estimate the field strength.

3.2 Observations and Data Reduction

With SHARP and CARMA we create polarimetric maps that show the fractional linear polarization, $P = \sqrt{Q^2 + U^2}/I$ (where I, Q, and U are Stokes parameters) and the angle with respect to the plane of the sky, θ (measured counterclockwise from north). When making uncertainty cuts based on polarization, we used polarized intensity, $P_I = IP$ rather than P. Due to the only positive nature of P and P_I, de-biasing these values is necessary (e.g., Vaillancourt 2006) and was done for all observations.

3.2.1 SHARP

Polarimetric observations of L1157-mm were made with SHARP in 2008 September. These observations were at 350 μm (resolution of $\sim$10″) and were mosaicked in a chop/nod observing mode. The SHARP data reduction is discussed in Chapman et al. (2013). The total integration time on L1157 is about 15.8 hr; due to constant chopping, the integration time on the source is closer to 7 hr.

3.2.2 CARMA

CARMA observations of L1157 in full-Stokes mode at 1.3 mm were first made in the E-array ($\sim$4.″6 resolution) in 2011 July as a CARMA summer school project. Additional observations in the D- ($\sim$2″) and C- ($\sim$0.″8) arrays were obtained over the next year as part of the TADPOL (Telescope Array Doing POLarization) key

project (e.g., Hull et al. 2013). An additional D-array summer school observation was also added in 2012 June.

The CARMA dual-polarization system is capable of measuring all 4 cross-correlations simultaneously through the circularly polarized feeds and full-Stokes correlator. The reduction process for the data in this Letter is explained in Hull et al. (2013). For L1157-mm, the flux calibrator was typically MWC349, but when this source was unavailable, we used Mars or Neptune. Flux calibration is accurate within ∼15%; however, for the rest of the paper, only statistical uncertainties are discussed. The phase calibrator used for all tracks was 1927+739.

3.3 Results

Figure 3.1 shows the results (dust continuum and the inferred magnetic field orientation) for SHARP and the combined CARMA observations. In the 350 μm SHARP map, an extension of the continuum is seen toward the southeast with a positional angle (PA, measured counterclockwise from north) of about 124°, differing from the PA of the outflow of 161° (Bachiller et al. 2001); however, this extension roughly coincides with N_2H^+ extension seen in Chiang et al. (2010). In the combined CARMA data, the continuum is extended toward the northwest with PA ≈ –20°, which agrees well with ∼ –27° from *Spitzer* 8μm and with –19° from Bachiller et al. (2001). This extension may be due to photons preferentially escaping through the poles, thus heating the outflow cavity. The continuum also extends toward the east, showing the flattened envelope of L1157-mm; this extension matches very well with *Spitzer* and N_2H^+ observations of the flattened structure (Chiang et al. 2010). Additionally, the continuum observations show an indication of this flattened structure toward the west. The east and west continuum extensions are also seen at 1.3 mm with the SMA at ∼5.″5 resolution (Tobin et al. 2013).

For SHARP, all vectors are aligned within ∼30° with the outflow angle measured by Bachiller et al. (2001); however, the southeast vector is offset from the mean of the other three vectors by 50°. CARMA vectors have a definitive hourglass shape, with the hourglass axis nearly coinciding with that of the outflow (Figure 3.2). We note that the difference between the hourglass axis and the outflow axis (a proxy for rotation axis) is about 15°[1]. We do not discuss the reason for this discrepancy, though we note that W. Kwon et al. (in preparation) discusses the possibility of two jets ejected from L1157-mm, and our hourglass is tilted toward the more CO-bright (and probably more massive) jet. We note that the northwest SHARP vectors also coincides better with the CO-bright jet (within ∼15°) than the entire outflow (within ∼30°).

[1]Hull et al. (2013) derived a PA difference of 0° for L1157 because they defined the outflow direction as the line connecting the two brightest CO(2–1) peaks, whereas we follow Bachiller et al. (2001), which uses the midline of the outflow cones.

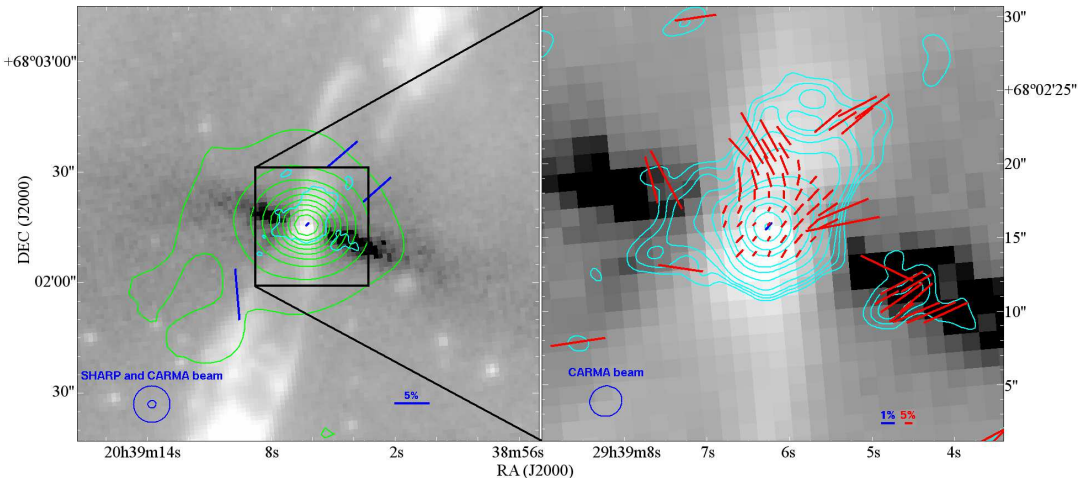

Figure 3.1 Polarimetric maps (with polarization vectors rotated by 90° to show the inferred magnetic field orientation) of L1157-mm with the grayscale background showing a log-scale map of *Spitzer* 8 μm emission (Looney et al. 2007). Magnetic field vectors are shown for $P_I > 2\sigma_{P_I}$ and $I > 2\sigma_I$. Left: SHARP continuum contours and vectors are shown in green and blue respectively. Cyan shows the 2σ intensity detections from CARMA. The length of the vectors is proportional to P. SHARP contour levels range from 10% to 90% in 10% increments of the peak flux. Right: cyan (red) contours (vectors) are the combined CARMA data at $2\farcs1$ resolution and the central blue vector is from SHARP. CARMA contour levels are [2,3,4,6,10,15,20,40,60,100,140]$\times\sigma$, σ=1.02 mJy beam^{-1}. Negative contours are not shown.

As seen in Figure 3.1, we also find that for both CARMA and SHARP observations, P is significantly less toward the center of the object, which is typical in polarimetric observations (e.g., Girart et al. 2006). Several factors may contribute to lower central fractional polarization, such as: (1) averaging along the line of sight is more likely to smear out the polarization through the thickest part of the source, (2) de-polarization at higher density, and (3) different grain populations at the center.

3.3.1 Comparison between Different Wavelengths

To compare SHARP and CARMA values, we smooth the CARMA data to a beam size of $10''$ to provide accurate comparison between wavelengths. We find that the central vectors have P=0.7% $\pm$ 0.2%, $\theta = -37\fdg9 \pm 9\fdg0$ for SHARP and P = 3.80% $\pm$ 0.11%, θ=$-32\fdg2 \pm 0\fdg8$ for the CARMA data. These vectors are our only point of comparison, and the angles are consistent with each other. This central angle is also consistent at all CARMA resolutions (see Figure 3.3).

Studies have attempted to explain polarization spectra observed in various molecular clouds. Vaillancourt & Matthews (2012) present $P[\lambda]/P[350]$ values at wavelengths, λ, of 60, 100, 850, and 1300 μm. The median $P[\lambda]/P[350]$ value of a cloud can vary dramatically, but the typical value for these wavelengths was $\sim$2. Our value of $P[1300]/P[350] \approx 5.4$ does not fit well within this polarization spectrum. However, comparisons

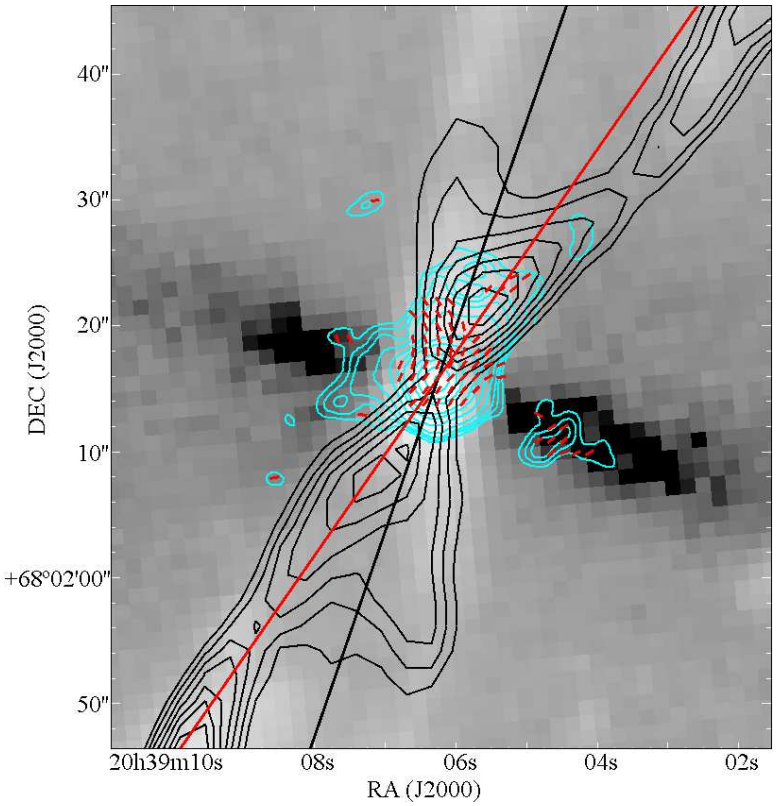

Figure 3.2 Hourglass morphology of L1157 with the red line showing the axis of the hourglass and the black line showing the center of the outflow from Bachiller et al. (2001). Cyan and red vectors are the same as Figure 3.1. Black contours show the CO(2–1) moment-0 map (integrated intensity) of the outflow with contour levels of [2,3,4,5,6,7,8,9]×σ, σ=8 Jy beam^{-1} km s^{-1} (W. Kwon et al., in preparation). Negative contours are not shown.

of single dish and interferometric fractional polarization should be made with caution; e.g., with varying polarization across the source, the interferometer tends to resolve out Stokes I more than Stokes Q or U, causing P to be overestimated. Additionally, we only have one point of comparison.

3.3.2 Comparison between Different Size Scales

When a cloud with initially parallel magnetic field lines collapses and flux-freezing holds at least partially, the field becomes pinched into an hourglass morphology. According to ambipolar diffusion low-mass star formation models (e.g., Fiedler & Mouschovias 1993; Galli & Shu 1993; Allen et al. 2003), the hourglass size may range from the size of the protostar cloud core (a few hundred to a few thousand AU) to the size of the protostar infall envelope (up to about 10,000 AU). Our observations probe resolutions from ∼300–2250 AU and will provide a diagnostic of the size scale of the pinch.

From our combined CARMA observations, we apply three different Gaussian tapers to the visibility data

which, along with the non-tapered data, probe four different resolutions (1.″2, 2.″1, 3.″0, 4.″5) as seen in Figure 3.3. We note that L1157-mm is only marginally resolved at 4.″5 resolution. Red vectors are shown when $P_I > 2\sigma_{P_I}$ and are shown spatially at approximately Nyquist frequency (∼2 vectors per beam). In attempt to see the most morphology possible given our sensitivity, we also show yellow vectors for $1.5\sigma_{P_I} < P_I < 2\sigma_{P_I}$.[2]

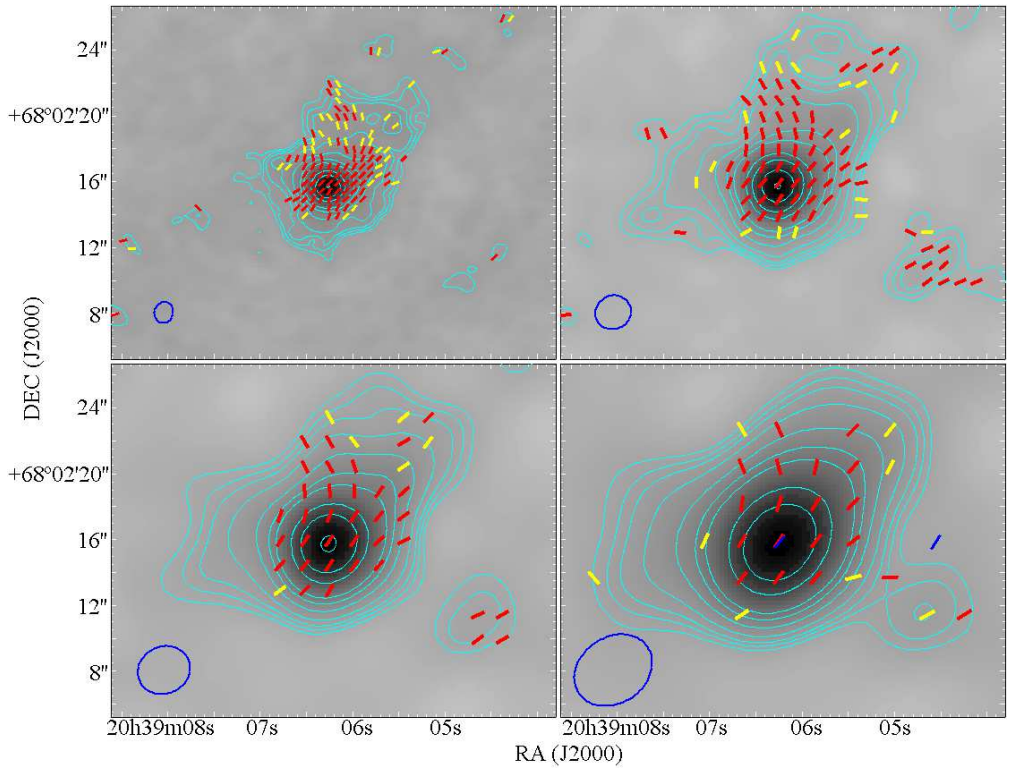

Figure 3.3 The dust continuum emission and magnetic field morphology as measured by CARMA to determine the size-scale at which we see the hourglass. Grayscale is the Stokes I intensity on a square root scale and the blue ellipses show the beam size for each resolution. All vectors have $I > 2\sigma_I$, the red vectors have $P_I > 2\sigma_{P_I}$, and the yellow vectors have $1.5\sigma_{P_I} < P_I < 2\sigma_{P_I}$. Top left: 1.″2 resolution, top right: 2.″1 resolution, bottom left: 3.″0 resolution, and bottom right: 4.″5 resolution, with SHARP vectors for $P_I > 1.5\sigma_{P_I}$ in blue (9″ resolution). The hourglass pinch becomes the most obvious at higher resolution. CARMA contour levels are the same as in Figure 1. The rms error, σ, for each of the four panels is 0.94, 1.02, 1.79, and 2.58 mJy beam^{-1} respectively.

Parts of the hourglass morphology can be detected in the lower resolution maps, but the full hourglass becomes evident in the two higher resolution plots. SHARP data, however, fail to see a definitive pinch even when considering lower σ detections (the entire low-σ SHARP polarization field is not shown in this Letter).

The resolution at which the *full* hourglass morphology becomes apparent at 1.3 mm is approximately 2.″1 or 550 AU. We note that this size-scale is highly uncertain (particularly due to distance and signal to

[2]When plotting vectors even down to P_I/σ_{P_I}=1, we notice that the scatter from the morphology is typically small ($\lesssim$10°, indicating we have overestimated errors and/or vectors are not independent). Therefore, $1.5\sigma_{P_I}$ vectors help in displaying the magnetic field morphology.

noise), though it is roughly consistent with the 290 AU resolution probing the hourglass in Girart et al. (2006), assuming a distance to NGC 1333 of 235 pc (Loinard 2013).

3.3.3 Magnetic Field Strength

The strength of the magnetic field cannot be measured directly from dust polarization maps; however, different methods allow for estimations. The standard technique for calculating magnetic fields from polarimetric maps is the Chandrasekhar–Fermi (CF) technique (Chandrasekhar & Fermi 1953) and modifications of the method.

We use a modified CF technique (Ostriker et al. 2001) in the large central region where polarimetric observations exist ($P_I > 2\sigma_{P_I}$ and $I > 2\sigma_I$ for the combined data at 2.1″ resolution). Our application of the technique follows the methodology outlined in Girart et al. (2006), which fits parabolas to the vectors and uses the residuals from the fits to calculate the angle dispersion in NGC 1333 IRAS 4A.

The central region of L1157-mm has a total flux of 0.35 Jy in an area of 70 arcsec^2. Using a dust temperature of 25 K (H.-F. Chiang 2013, private communication) and a dust opacity of κ_ν=0.9 cm^2 g^{-1} (Ossenkopf & Henning 1994), we find that the central region has a mean volume density of $n(\mathrm{H_2})$=7.4×10^6 cm^{-3}. From N_2H^+ observations, we use a non-thermal rms velocity dispersion about the line of sight of $\delta v_{\rm los} = 0.18$ km s^{-1} (Chiang et al. 2010). The dispersion from the residuals of parabola fits was 7.°5 (see Figure 3.4) and the uncertainty of the polarization angle is ∼4°, resulting in an angular dispersion of $\delta\phi = 6°$. Given these parameters, we find a plane-of-sky magnetic field measurement of 1.4 mG. Using these values, the mass-to-magnetic flux ratio (using the method discussed in Crutcher 1999) is found to be 1.1 times the critical value for collapse.

Since the CF method only calculates the average magnetic field strength and has numerous uncertainties (see discussion in Crutcher 2012), we also use another method by Koch et al. (2012) that calculates the magnetic field strength at all locations where there are dust polarization and emission measurements. This technique assumes ideal magnetohydrodynamics (MHD) and that the dust emission gradient indicates the direction of the MHD force equation, leading to the equation for the magnetic field strength below:

$$B = \sqrt{\frac{\sin\psi}{\sin\alpha}(\nabla P + \rho\nabla\phi)\ 4\pi R} \tag{3.1}$$

In this equation, ψ is the angle difference between gravity and the intensity gradient, α is the difference between polarization and the intensity gradient, P is the hydrostatic pressure, ϕ is the gravitational potential as a function of radius, and R is the local curvature radius of the polarization vectors. When applying this technique, we assume a density profile of the envelope to follow the fits of L1157-mm observations in Chiang

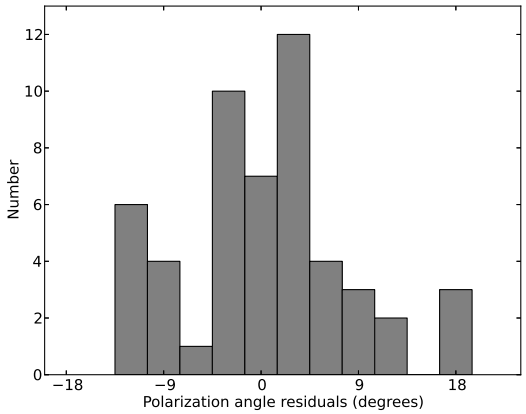

Figure 3.4 Histogram of angle residuals (difference between measured angle and parabolic fit) at each vector location. One vector in the west of L1157-mm was excluded from the fitting since it caused a large reduced χ^2 value.

et al. (2012, power-law of $\rho \propto r^{-p}$ with $p = 2$). We also use a central core mass of $M_0 = 0.19\ M_\odot$ (assumed to be similar to L1527, Tobin et al. 2012). Additionally, we assume the pressure gradient, ∇P, to be negligible compared to gravity. The local curvature is calculated in the manner suggested in Koch et al. (2012).

The magnetic field throughout the large central region where polarimetric observations exist ($P_I > 2\sigma_{P_I}$ and $I > 2\sigma_I$ for the combined data at $2\farcs1$ resolution) can be seen in Figure 3.5; outside this area, magnetic field measurements are unreliable. This figure uses median-filtered smoothing at approximately Nyquist sampling (i.e., with pixel sizes of $0\farcs25$, we replace each pixel value by the median of the surrounding 5×5 box). The color bar indicates the field strength in mG, with an average and median magnetic field throughout the region of 3.6 and 3.4 mG respectively. The red contours show the locations where magnetic field tension dominates gravity (subcritical). Note that the central areas are supercritical (gravity dominates the magnetic field tension). The Koch et al. (2012) method determines the criticality based on sin ψ/sin α, while the critical values for the CF method is an average about the entire region and depends on calculated values (e.g., magnetic field strength, mass).

When using the method from Koch et al. (2012) to estimate the magnetic field, we have three free parameters: p, M_0, and distance, d. In the parameter space of our uncertainty in variables, $1.5 < p < 2.5$, $0.1\ M_\odot < M_0 < 0.75\ M_\odot$, and 200 pc $< d <$ 500 pc, the median magnetic field follows the approximate relationship:

$$B = 3.4\ \mathrm{mG} \left(\frac{p}{2}\right)^{1.9} \left(\frac{M_0}{0.19\ M_\odot}\right)^{0.5} \left(\frac{d}{250\ \mathrm{pc}}\right)^{0.5} \tag{3.2}$$

When altering these parameters, our median magnetic field value of 3.4 mG does not drastically change

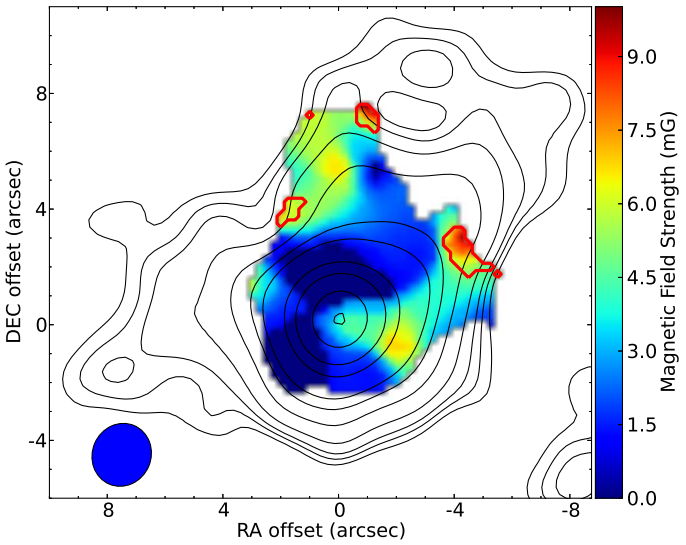

Figure 3.5 Magnetic field throughout L1157-mm with the color scale in mG. Black contours are the same as Figure 1. Red contours indicate subcritical locations, while the rest of the colored area is supercritical.

and will generally be within a factor of ∼2. Note that changing these parameters does not change the supercritical and subcritical locations in the cloud since these locations only depend on the value of sin ψ/sin α.

3.4 Discussion

In this Letter we present the first detection of magnetic fields in L1157-mm at two different wavelengths. Our main results are:

- We find the second instance of a full hourglass morphology in the inferred magnetic field around a low-mass protostar. This is also only the second instance around a Class 0 source. The axis of the hourglass is nearly aligned with the axis of the outflow, with the full detection of the hourglass occurring at a resolution of ∼550 AU.
- The angle of the central magnetic field vector agrees at 350 μm and 1.3 mm and at all size-scales.
- We used two methods to calculate the plane-of-sky magnetic field throughout the central region and find values of 1.4 and 3.4 mG.

While this particular hourglass is nearly aligned with the outflow, the TADPOL survey results have shown that in general, magnetic field lines are consistent with being preferentially misaligned (perpendicular) or randomly aligned with respect to outflows (Hull et al. 2013).

The first well-defined hourglass morphology around a low-mass protostar was observed in 1997 in the Class 0 binary system NGC 1333 IRAS 4A (Girart et al. 1999); such a discovery has not been published since. Our observation of L1157-mm is arguably the best example of an hourglass shape in any star formation region to date. Characterizing such systems is an important step to better understand the role of magnetic fields in star formation.

IRAS 4A's hourglass axis of symmetry is misaligned with large scale outflow as measured by CO(3–2) (Blake et al. 1995) by 16° and is over 40° misaligned with the small scale outflow as measured by SiO(1–0) (Choi 2005). However, SHARP observations found that the large scale field in IRAS 4A coincides within 1° of the large scale outflow (Attard et al. 2009). Our observations of L1157-mm find that the hourglass axis of symmetry and northwest SHARP vectors are similarly misaligned by ∼15–30°, but the hourglass axis is more aligned with the outflow than these SHARP vectors. These results suggest the need to compare more polarimetric observations at different resolutions, which will be a future TADPOL project.

Recent high resolution Expanded Very Large Array observations detect only a single continuum source at size scales of ∼12 AU (J. J. Tobin 2013, private communication), suggesting that L1157-mm is most likely a single source. Perhaps cores with a single system are more likely to yield an hourglass detection and/or an hourglass axis aligned with the outflow.

We thank Katherine Rosenfeld, Che-Yu Chen, and Aaron Juarez for their help in providing CARMA summer school tracks.

Support for CARMA construction was derived from the states of California, Illinois, and Maryland, the James S. McDonnell Foundation, the Gordon and Betty Moore Foundation, the Kenneth T. and Eileen L. Norris Foundation, the University of Chicago, the Associates of the California Institute of Technology, and the National Science Foundation. Ongoing CARMA development and operations are supported by the National Science Foundation under a cooperative agreement (NSF AST 08-38226) and by the CARMA partner universities.

The Caltech Submillimeter Observatory is operated by the California Institute of Technology under cooperative agreement with the National Science Foundation (AST-0838261), and SHARP is supported by NSF grant AST-090930 to Northwestern University.

Chapter 4

Surveying HII Regions of Young Stellar Objects in the Large Magellanic Cloud

4.1 Introduction

The formation of massive stars (defined here as $M_*/M_\odot > 8$) is considered significantly different than low-mass stars (e.g., Zinnecker & Yorke 2007). During star formation, massive protostars quickly accumulate enough mass to initiate hydrogen fusion before they finish accreting. Since these stars are still in the formation process, they are often called "young stellar objects" (YSOs). If these high-mass YSOs have sufficiently high photospheric temperatures (i.e,. they're not dramatically expanded by ongoing accretion), then they will have intense UV radiation. If hydrogen ionizes faster than it accretes on the YSO, an H II region will form.

H II regions around YSOs can span a wide range of sizes and densities and are classified in Habing & Israel (1979) and Franco et al. (2000). The densest YSO H II regions are called hypercompact (HC, $\lesssim$0.03 pc, $\gtrsim 10^6$ cm^{-3}), ultracompact (UC, $\lesssim$0.1 pc, $\gtrsim 10^4$ cm^{-3}), compact ($\lesssim$0.5 pc, $\gtrsim 3\times10^3$ cm^{-3}), and dense ($\lesssim$2 pc, $\gtrsim$300 cm^{-3}). Such regions can also have extended emission of several pc which may be caused by leakage of ionizing photons out of the immediate vicinity of the massive YSO through holes in a clumpy envelope (e.g., Kurtz et al. 1999; Kim & Koo 2001, hereafter KK01). The massive YSO's H II region eventually grows (sometimes combining with other nearby H II regions) into the so-called classical H II region ($\sim$10 pc, $\sim$100 cm^{-3}).

During the densest stages (in particular, the HC and UC H II stages), these regions have strong optical extinction, which can cause Hα emission to be undetected. However, radio observations of free-free emission suffer much less from extinction and therefore can provide a better survey of compact YSO H II regions. The first large, high-resolution (0.″4) survey of UC H II regions in our Galaxy was completed by Wood

This chapter includes material in preparation for publication which includes the authors Ian W. Stephens, Leslie W. Looney, Remy Indebetouw, You-Hua Chu, Robert A. Gruendl, C.-H. Rosie Chen, Jonathan P. Seale, Maxim A. Voronkov, Jessica Marie Evans.

& Churchwell (1989a, hereafter WC89) and extended by Kurtz et al. (1994). These two Galactic studies surveyed over 100 UC H II regions and found five distinct morphologies.

WC89 introduced the notion of the "age" or "lifetime" problem: more UC H II are detected than expected from dynamical expansion. Numerous works had suggested possible explanations of the problem, such as thermal pressure or accretion. KK01 suggested a hierarchical structure of H II regions where an UC H II region can be embedded in an extended H II region. It is suggested that the hierarchical structure is ionized by the same ionizing source, i.e., ionizing flux can escape the UC H II region to create extended regions. These extended regions can expand more dynamically and indicate ages of $\gtrsim 10^5$ yr, allowing for the WC89 UC detection count.

Simulations by Peters et al. (2010a) that include feedback by both ionizing and non-ionizing radiation showed that the five UC H II morphologies defined in WC89 are all apparent in a massive star-forming cluster. These morphologies, however, typically do not represent different evolution states. Instead, UC H II regions can grow and contract, and only when accretion slows down, the H II region can dynamically grow.

While the Milky Way can be used for studying YSO H II regions at high resolution, there are many challenges when studying these Galactic sources, including large distance uncertainties, extinction about the Galactic plane, and confusion of the broadband tracers (e.g., infrared emission) along the line of sight. Observations in the Large Magellanic Cloud (LMC) mitigate these problems. The LMC has a known distance of $\sim$50 kpc (Feast 1999), which is close enough to resolve stars, a nearly face-on orientation (inclination of $\sim 35^\circ$, van der Marel & Cioni 2001), and low extinction. Thus, the LMC allows for perhaps the most homogenous sample for a survey of YSO H II regions.

Since the launch of the *Spitzer Space Telescope*, large samples of LMC YSOs have been created (e.g., Gruendl & Chu 2009). Seale et al. (2009, hereafter SL09) used *Spitzer*'s Infrared Spectrograph (IRS) to spectroscopically identify 277 of the most massive LMC YSOs. From each YSO's spectrum, SL09 used principal component analysis (PCA) of the silicate absorption to quantify the embeddedness (which is likely indicative of age) of each YSO, while C.-H. R. Chen et al. (in preparation) modeled each YSO's spectral energy distribution (SED) for stellar mass estimates.

The peak of the free-free emission spectrum for a massive YSO is a function of the surrounding electron density. For UC H II regions, this peak is just above 5 GHz (Kurtz 2005). Higher densities require higher frequencies (millimeter wavelengths) whose emission will be contaminated with dust emission. In this paper we present a free-free emission survey of $\sim$60 massive LMC YSOs with the Australia Telescope Compact Array (ATCA) at 5.5 and 9 GHz. The resolution at these frequencies is about $2\farcs5$ and $1\farcs5$ respectively or 0.625 and 0.375 pc at the distance of the LMC; thus, our observations of these regions will not have the five

morphologies as expressed in WC89. Resolved observations will either be regions that are no longer compact or contain one or more compact sources (that are often <0.1 pc in size) embedded in brighter extended emission.

With the combination of sources from Indebetouw et al. (2004, hereafter IJC04), we have free-free observations around 102 LMC YSOs with *Spitzer* IRS observations. We find detections around 54 of these sources and investigate correlations between the H II region parameters and *Spitzer* spectra/models. In particular, we compare our observations to the modeled masses, which proves to be a pertinent variable in the discussion of H II regions. In this paper we discuss our ATCA and *Spitzer* observations in Section 4.2, present results of ATCA observations and compare them with *Spitzer* spectra and photometry in Section 4.3, and summarize in Section 4.4.

4.2 Observations and Data Reduction

4.2.1 ATCA Free-Free Observations

High resolution observations with ATCA using the Compact Array Broadband Backend (CABB) correlator were made from 2009 January 28 to February 1 with baselines up to 6 km. Simultaneous observations at 5.5 and 9 GHz (5.5 and 3.3 cm respectively) were carried out on 16 fields. Typical synthesized beam sizes were about $3\farcs0 \times 2\farcs1$ and $1\farcs8 \times 1\farcs3$ for 5.5 and 9 GHz respectively. These observations are insensitive to structures above about $50''$ and $29''$ for 5.5 and 9 GHz respectively. The MIRIAD package (Sault et al. 1995) was used for data reduction, and we followed the typical procedures for reduction. The bandpass calibrator used for the observations was either 1253-055 or 1934-638. The phase calibrator used was 0530-727. Flux calibration used observations of the source 1934-638 and is accurate to within $\sim$10%, although for the rest of the paper, only statistical uncertainties are considered. For fields with large noises due to bright sources, we iteratively used self-calibration, using each successive clean image as a model. Each field was also corrected for primary beam sensitivity. These ATCA observations can be seen in Figures 4.11-4.40 at the end of this paper.

For a more complete sample, 10 fields were also taken from IJC04 for a total of 26 fields. While more fields were available in IJC04, we only include the fields that contain LMC YSOs with *Spitzer* IRS observations from SL09 and were not duplicates with the observations from this study. These fields were observed at slightly different frequencies of 4.8 and 8.64 GHz (6.2 and 3.5 cm respectively) and are not as deep as our observations (see Table 4.1). IJC04 observations have resolutions of $2\farcs0/1\farcs5$ and are insensitive to structures greater than $30''/20''$ for 4.8/8.64 GHz respectively. For the rest of the paper, the 5.5 and 4.8 GHz

observations will collectively be referred to as "6 cm" and the 9 and 8.64 GHz observations as "3 cm".

Figure 4.1 shows the entire LMC in Hα with circles indicating the full width half maximum (FWHM) of each observation's 6 cm primary beam response with yellow triangles showing the location of SL09 sources. A summary of all observations is seen in Table 4.1. The listed rms values show the approximate noise of the map, and the listed beams denote the synthesized beams with positions angles (PA) measured counterclockwise from north. Regions with multiple RA/DEC values had multiple pointings, and the listed sensitivities and beams are for the combined mosaics.

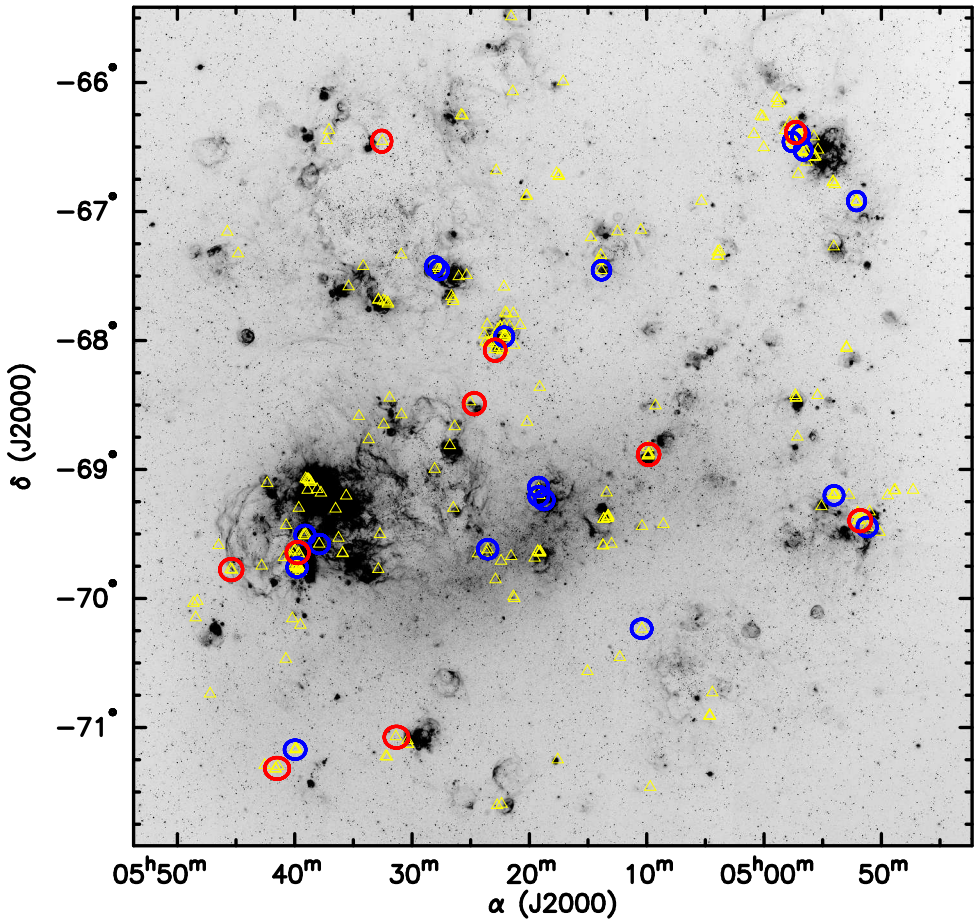

Figure 4.1 Hα image from the Magellanic Cloud Emission-Line Survey (MCELS, Smith & MCELS Team 1999). Circles show the 6 cm primary beam sizes for observations from this study (blue) and archival observations (red, Indebetouw et al. 2004). Yellow triangles show locations of SL09 YSOs with *Spitzer* IRS observations.

Table 4.1. Summary of Observations

Region[a] Name	RA (J2000)	DEC (J2000)	3 cm rms (μJy)	6 cm rms (μJy)	3 cm Beam Size, PA ($'' \times ''$, $^\circ$)	6 cm Beam Size, PA ($'' \times ''$, $^\circ$)
N79	04:51:12.60	–69:26:45.40	49	43	1.8×1.3, 15	3.0×2.1, 15
N4	04:52:06.78	–66:55:09.61	58	41	1.9×1.3, –88	2.7×2.3, 59
N83	04:54:02.21	–69:12:02.56	49	43	1.8×1.3, 16	3.0×2.1, 15
N11F	04:56:39.87	–66:31:35.61	46	31	2.2×1.2, –56	3.2×2.0, –52
N11A/B	04:56:54.00	–66:24:30.00	63	45	3.2×1.0, –48	4.8×1.7, –48
N11C/D	04:57:36.99	–66:27:36.86	47	32	2.2×1.2, –54	3.2×2.1, –49
None	05:10:25.97	–70:14:01.28	46	43	1.9×1.3, 13	3.0×2.1, 13
N30	05:13:51.20	–67:27:21.46	46	32	2.2×1.2, –56	3.2×2.1, –51
N119	05:18:44.42	–69:14:12.25	46	33	1.8×1.3, 10	3.0×2.1, 10
	05:19:11.78	–69:12:23.84				
	05:19:13.00	–69:08:07.94				
N44	05:22:08.68	–67:58:12.87	57	41	1.8×1.3, 77	2.8×2.3, 47
N132	05:23:33.02	–69:37:03.73	47	44	1.9×1.3, 9	3.1×2.1, 9
N51	05:27:41.04	–67:27:15.60	55	30	1.9×1.3, 84	2.7×2.3, 51
	05:28:03.39	–67:25:30.87				
N156	05:37:54.05	–69:34:39.20	67	44	3.6×1.0, –54	4.6×1.7, –54
N158	05:39:07.52	–69:30:25.44	67	46	3.0×1.0, –59	4.5×1.7, –57
N159	05:39:48.00	–69:45:32.00	64	46	3.3×1.0, –59	4.7×1.7, –56
N214	05:39:57.98	–71:10:18.05	67	46	3.2×1.0, –55	4.7×1.7, –55
			Fields from IJC04			
N79	04:51:48.00	–69:23:48.00	1500	530	1.8×1.2, 15	2.1×1.7, 13
N11A	04:57:18.00	–66:23:16.00	160	230	1.6×1.4, –30	1.8×1.7, –31
N105	05:09:50.00	–68:52:59.99	620	300	1.8×1.2, 15	2.2×1.7, 17
N44	05:22:55.00	–68:04:29.99	150	89	1.7×1.3, 2	1.9×1.7, 3
N138	05:24:41.80	–68:29:23.23	75	81	1.6×1.3, 4	2.0×1.7, 8
N206	05:31:20.00	–71:04:29.99	120	84	1.7×1.5, 19	1.9×1.8, 20
N55	05:32:35.00	–66:27:19.99	61	76	1.7×1.3, 1	2.2×1.7, 2
N160	05:39:45.00	–69:38:39.99	600	500	1.6×1.4, –31	2.1×1.7, –10
N214	05:41:30.00	–71:18:59.99	120	93	1.8×1.5, –5	2.1×1.7, –8
N168	05:45:24.57	–69:46:33.73	92	81	1.6×1.3, 1	2.0×1.7, 3

[a]Designation from Henize (1956).

4.2.2 YSO *Spitzer* IRS observations

SL09 used *Spitzer* IRS to analyze the mid-infrared spectra from ∼5 to 37 μm of 294 objects. These objects were selected based on classification of Gruendl & Chu (2009), primarily consisting of "definite" and "probable" YSOs with high 8 μm flux ([8.0] < 8.0). 277 of these sources had spectra indicative of embedded YSOs, and PCA analysis was used to quantify the silicate absorption. Silicate PCA strength values vary from about –0.7 to 0.7; positive values indicate silicate absorption (with values $\gtrsim$0.2 having strong silicate absorption) and those with negative values were either contaminated by other lines or had no silicate absorption. While objects with disks often have their silicate spectra highly dependent on the source's inclination angle, it is expected that these sources are not degenerate; at these ages, the silicate absorption of the YSOs' spectra relates to the source's embeddedness (J. M. Oliveira 2013, private communication). Thus, for positive silicate PCA strengths, we posit that a larger value (more silicate absorption) implies a more embedded, *younger* source. Negative PCA values, however, have little or no indication of the YSO's evolutionary stage.

SL09 also classified sources in different groups based on the features of each spectra. In our samples of YSOs, we have sources from all 6 embedded groups: S, P, SE, PE, E, and F. The S and P groups denote spectra with strong silicate absorption and polycyclic aromatic hydrocarbon (PAH) emission respectively, while the SE/PE groups have strong silicate/PAHs along with fine structure lines. The E group has the spectra dominated by emission lines, and the F group has no dominant spectral features but are still indicative of YSOs.

Additionally, C.-H. R. Chen et al. (in preparation) combined *Spitzer* IRS and photometric observations (from U-band to 70 μm) to model each YSO according to Robitaille et al. (2007). These models included fits for 14 parameters, including stellar mass ($M_{\rm SED}$). However, there is a significant limitation to this SED modeling: it assumes only a single source. Indeed, using higher resolution than *Spitzer* resolves more sources for each YSO; HST observations have found that a massive YSO is typically resolved into a few (e.g., Vaidya et al. 2009) or many (>10, I. W. Stephens et al. in preparation) sources. Certainly at even higher resolutions than HST, more massive stars will be found since YSO multiplicity may exist at scales smaller than 100 AU. Regardless, the YSO spectrum is typically dominated by the most massive source (or a massive binary), which can still provide reasonable estimates for the YSO's mass and luminosity.

4.2.3 YSO H II Regions and Fitting of Sources

For our analysis, we are concerned with H II regions that are ionized by the massive YSO itself, so it is important to confirm that the H II region is created due to the YSO and not some other source. Thus, we

use a combination of Hα and IR imaging and optical photometry. High-resolution ($\sim$1$''$) Hα images from the MOSAIC2 camera on the Blanco 4m telescope at the Cerro Tololo Inter-American Observatory were used to observe the surrounding ionized hydrogen. While the location of the YSO is determined by *Spitzer* in Gruendl & Chu (2009), some sources can have multiple peaks or are elongated in the IR; thus, archival *Spitzer* 8 μm observations were used to match the YSO with the ATCA continuum observations. In addition, using the methodology described in I. W. Stephens et al. (submitted), we can use photometry (primarily from the Magellanic Cloud Photometric Survey (Zaritsky et al. 2004)) and massive star evolutionary tracks (Lejeune & Schaerer 2001) to find the locations of all ionizing stars ($\gtrsim$7 M$_\odot$) throughout the LMC. From here, we classify each source at 6 cm as detected, undetected, or indeterminate (i.e., there is flux nearby, but it is difficult to tell if the YSO is causing the ionization). Since sources that were detected at 3 cm were always detected at 6 cm, the detection classification was based on 6 cm.

All massive YSOs that were observed are listed in Table 4.2. Undetected sources are given an upper limit of four times the sensitivity of the field. It is not uncommon for IR sources outside of the FWHM of the primary beam to be detected, and these sources were all included in our sample. Undetected sources outside of the FWHM, however, were not considered as part of the sample. Our observations were always used in cases where the FWHM of the primary beams of our observations and those from IJC04 overlapped. In a few cases, sources were detected outside of the FWHM of our observations and were incident on IJC04 fields. In these cases we always used IJC04 observations except in rare situations where IJC04 fields had exceptionally poor sensitivity and caused some sources to be undetected.

Table 4.2. Observed YSOs

IRAC Source[a]	$M_{\rm SED}$ ($M_\odot$)	Silicate[b] PCA	YSO[b] Group	D?[c]	RA (J2000)	DEC (J2000)	$F_{3\rm cm}$[d] (mJy)	$F_{6\rm cm}$[d] (mJy)	3 cm Size, PA[d] ($'' \times ''$)	6 cm Size, PA[d] ($'' \times ''$, $^\circ$)	log Q_0[e]	Sp.[e] Type	α	Region Name
045111.39-692646.7	27.4±4.2	0.55	S	Y	04:51:11.771	–69:26:46.96	0.31±0.17	0.54±0.15	Point Source	1.8×1.5, 50	47.1	B0.5V	–1.2±1.3	N79
045205.39-665513.8	17.1±2.3	0.12	PE	Y	04:52:05.663	–66:55:13.41	10.7±1.8	29.9±5.4	11.4×3.0, 65	9.6×6.5, 51	48.8	O7.5V	–2.1±0.5	N4
045206.97-665516.4	30.3±4.5	0.42	SE	Y	···	···	···	···	···	···	48.8	···	···	N4
045208.94-665537.4	14.0±2.3	–0.05	PE	I	···	···	···	···	···	···	48.8	···	···	N4
045209.22-665521.9	28.9±4.6	0.17	PE	Y	04:52:09.268	–66:55:22.66	22.0±2.3	66.6±8.6	9.8×4.1, –42	13.9×6.4, –33	49.2	O7V	–2.3±0.3	N4
045358.57-691106.7	25.2±3.6	0.54	P	Y	04:53:58.612	–69:11:05.99	6.0±0.6	2.8±0.2	0.9×0.5, –10	Point Source	47.8	B0V	1.5±0.3	N83
045400.10-691155.5	21.4±4.3	0.68	PE	N	···	···	<0.19	<0.17	···	···	47.8	···	···	N83
045401.14-691152.9	25.2±3.7	0.27	PE	I	···	···	···	···	···	···	47.8	···	···	N83
045403.04-691139.7	18.6±2.8	0.21	PE	N	···	···	<0.19	<0.17	···	···	47.8	···	···	N83
045426.06-691102.3	35.0±4.7	–0.06	PE	Y	04:54:26.124	–69:11:01.72	67.3±2.2	43.7±1.0	1.8×1.5, –44	1.9×1.8, –29	49.0	O7.5V	0.9±0.1	N83
045550.62-663434.6	22.4±4.0	0.36	S	Y[f]	04:55:50.635	–66:34:34.76	···	2.3±0.3	···	1.4×0.7, –31	47.7	B0V	···	N11F
045625.99-663155.5	12.3±1.9	–0.13	PE	Y	04:56:25.607	–66:31:54.90	0.81±0.24	0.88±0.16	4.0×2.1, –66	6.4×4.2, –47	47.3	B0.5V	–0.2±0.7	N11F
045629.02-663159.3	13.4±1.9	0.05	PE	Y	04:56:29.114	–66:31:58.44	0.16±0.08	0.46±0.13	Point Source	5.3×2.6, –47	47.0	B0.5V	–2.1±1.1	N11F
045638.76-662446.2	10.9±1.9	0.03	PE	N	···	···	<0.25	<0.18	···	···	47.0	···	···	N11A/B
045640.79-663230.5	20.1±4.9	–0.14	F	Y	04:56:40.763	–66:32:30.52	0.35±0.16	0.41±0.12	3.1×0.4, –33	3.2×1.5, –67	47.0	B0.5V	–0.3±1.1	N11F
045647.23-662431.8	···	0.10	PE	Y	04:56:47.897	–66:24:34.49	13.7±2.2	15.6±1.2	10.8×7.6, –21	9.7×6.3, –87	48.5	O8V	–0.3±0.4	N11A/B
045651.82-663133.0	9.9±1.0	–0.20	PE	N	···	···	<0.18	<0.12	···	···	48.5	···	···	N11F
045657.25-662513.0	23.5±4.7	0.10	PE	Y	04:56:57.392	–66:25:12.84	3.5±0.6	3.9±0.3	4.7×1.0, –44	3.5×1.1, –45	47.9	O9V	–0.2±0.4	N11A/B
045659.85-662425.9	12.1±1.3	–0.50	PE	Y	04:56:59.996	–66:24:24.75	3.1±0.5	0.96±0.13	6.3×2.5, –34	4.6×1.4, –41	47.3	B0.5V	2.4±0.4	N11A/B
045716.25-662319.9	18.3±1.7	–0.03	PE	Y	04:57:16.575	–66:23:19.78	34.8±3.4	39.6±1.3	11.5×5.5, –54	6.8×5.2, –55	48.9	O7.5V	–0.3±0.2	N11A/B
045720.72-662814.4	9.7±1.0	–0.26	PE	N	···	···	<0.18	<0.13	···	···	48.9	···	···	N11C/D
045742.00-662634.4	15.6±2.4	–0.07	PE	Y	04:57:41.976	–66:26:33.69	0.40±0.16	0.29±0.04	2.0×1.2, –43	Point Source	46.8	B0.5V	0.6±0.9	N11C/D
045747.68-662816.9	19.4±4.4	0.26	PE	Y	04:57:47.573	–66:28:16.38	<0.18	0.96±0.17	···	5.3×4.2, 68	47.3	B0.5V	···	N11C/D
045749.22-662900.3	13.8±1.1	–0.03	P	Y	04:57:49.278	–66:29:00.57	0.14±0.06	1.3±0.3	Point Source	5.1×4.3, –80	47.5	B0V	–4.5±1.0	N11C/D
051024.09-701406.5	23.4±6.1	0.37	S	N	···	···	<0.18	<0.17	···	···	47.5	···	···	None
051351.51-672721.9	31.8±4.2	0.25	P	Y	05:13:51.576	–67:27:22.21	7.6±0.2	4.6±0.3	Point Source	1.2×0.8, 24	48.0	O9V	1.0±0.1	N30
051909.02-691156.1	16.1±3.4	–0.05	F	N	···	···	<0.18	<0.13	···	···	48.0	···	···	N119

Table 4.2 (cont'd)

IRAC Source[a]	$M_{\rm SED}$ ($M_\odot$)	Silicate[b] PCA	YSO[b] Group	D?[c]	RA (J2000)	DEC (J2000)	$F_{3\rm cm}$[d] (mJy)	$F_{6\rm cm}$[d] (mJy)	3 cm Size, PA[d] ($'' \times ''$)	6 cm Size, PA[d] ($'' \times ''$, $^\circ$)	log Q_0[e]	Sp.[e] Type	α	Region Name
051912.27-690907.3	37.7±5.4	0.56	S	Y	05:19:12.451	–69:09:06.73	0.75±0.21	0.83±0.10	1.8×0.6, 32	1.6×0.7, 11	47.3	B0.5V	–0.2±0.6	N119
052147.09-675656.8	15.8±2.4	–0.05	PE	I	···	···	···	···	···	···	47.3	···	···	N44
052156.97-675700.1	11.5±1.0	0.07	PE	N	···	···	<0.22	<0.16	···	···	47.3	···	···	N44
052202.11-675753.6	17.7±2.1	0.29	PE	Y	05:22:02.108	–67:57:53.60	1.0±0.4	0.88±0.23	3.4×1.3, –63	3.3×2.6, –89	47.3	B0.5V	0.3±0.9	N44
052203.30-675747.0	20.8±2.5	0.15	PE	N	···	···	<0.22	<0.16	···	···	47.3	···	···	N44
052204.85-675800.3	16.9±2.1	–0.06	PE	N	···	···	<0.22	<0.16	···	···	47.3	···	···	N44
052207.27-675819.7	14.1±2.2	–0.13	PE	Y	05:22:07.255	–67:58:20.54	<0.22	0.85±0.19	···	4.4×2.2, –33	47.3	B0.5V	···	N44
052212.57-675832.4	42.9±4.4	0.44	SE	Y	05:22:12.640	–67:58:32.09	49.2±0.5	45.4±1.3	1.2×0.4, 64	1.6×0.9, 55	49.0	O7V	0.2±0.1	N44
052333.40-693712.2	19.1±1.8	0.48	P	N	···	···	<0.18	<0.17	···	···	49.0	···	···	N132
052337.88-693854.4	22.7±2.7	–0.28	P	N	···	···	<0.18	<0.17	···	···	49.0	···	···	N132
052736.93-672728.6	13.4±1.2	–0.49	F	N	···	···	<0.24	<0.12	···	···	49.0	···	···	N51
052743.47-672624.2	17.0±3.3	0.14	P	N	···	···	<0.24	<0.12	···	···	49.0	···	···	N51
052757.09-672522.3	13.7±1.6	–0.15	PE	Y	05:27:57.029	–67:25:22.77	1.9±0.4	2.8±0.3	4.5×3.2, 43	4.7×4.5, 25	47.8	B0V	–0.8±0.5	N51
052803.20-672525.6	14.4±0.8	–0.12	PE	N	···	···	<0.24	<0.12	···	···	47.8	···	···	N51
053754.82-693435.8	15.3±3.0	0.43	S	N	···	···	<0.26	<0.18	···	···	47.8	···	···	N156
053904.88-692949.9	15.4±1.9	–0.04	PE	Y	05:39:04.769	–69:29:49.45	0.36±0.24	0.40±0.09	Point Source	5.0×1.3, –53	46.9	B0.5V	–0.2±1.4	N158
053906.31-693043.8	13.6±1.4	–0.15	PE	N	···	···	<0.26	<0.18	···	···	46.9	···	···	N158
053915.77-693039.9	···	0.10	PE	Y	05:39:15.414	–69:30:38.43	6.8±0.8	24.7±1.6	8.3×4.8, –49	8.9×6.6, 5	48.7	O8V	–2.6±0.3	N158
053929.21-694719.0	···	0.36	P	I	···	···	···	···	···	···	48.7	···	···	N159
053935.99-694604.1	22.6±6.7	–0.08	PE	N	···	···	<0.25	<0.18	···	···	48.7	···	···	N159
053937.04-694536.7	28.2±4.0	0.68	PE	Y	05:39:36.913	–69:45:36.21	1.3±0.3	0.54±0.15	Point Source	Point Source	47.1	B0.5V	1.8±0.7	N159
053937.53-694609.8	32.0±4.7	0.04	PE	Y	05:39:37.543	–69:46:09.59	17.0±2.2	63.7±5.6	3.6×2.8, –8	6.1×3.3, 9	49.2	O7V	–2.7±0.3	N159
053937.60-694525.0	34.4±5.2	0.37	PE	Y	05:39:37.454	–69:45:25.78	114.2±3.2	147.3±3.8	3.4×2.8, 47	3.8×3.6, –0	49.5	O3V	–0.5±0.1	N159
053941.89-694612.0	33.2±5.2	0.38	PE	N	···	···	<0.25	<0.18	···	···	49.5	···	···	N159
053945.18-694450.4	19.7±1.1	0.05	PE	Y	05:39:44.981	–69:44:50.11	1.5±0.2	3.1±0.5	6.6×1.4, –71	8.0×2.4, –58	47.8	B0V	–1.5±0.5	N159
053951.60-694510.5	···	0.16	PE	Y	05:39:51.848	–69:45:10.16	1.6±0.3	6.1±0.5	6.9×1.6, –69	6.0×4.1, –72	48.1	O9V	–2.8±0.5	N159
053952.11-710930.7	14.2±3.2	–0.34	P	N	···	···	<0.26	<0.18	···	···	48.1	···	···	N214

Table 4.2 (cont'd)

IRAC Source[a]	$M_{\rm SED}$ ($M_\odot$)	Silicate[b] PCA	YSO[b] Group	D?[c]	RA (J2000)	DEC (J2000)	$F_{3\rm cm}$[d] (mJy)	$F_{6\rm cm}$[d] (mJy)	3 cm Size, PA[d] ($'' \times ''$)	6 cm Size, PA[d] ($'' \times ''$, $^\circ$)	log Q_0[e]	Sp.[e] Type	α	Region Name
053952.29-694516.5	···	0.14	PE	I	···	···	···	···	···	···	48.1	···	···	N159
053953.43-710953.1	22.2±2.7	0.26	P	I	···	···	···	···	···	···	48.1	···	···	N214
053955.66-711000.9	19.6±2.5	0.13	PE	Y	05:39:55.698	–71:10:00.91	0.32±0.11	1.7±0.2	Point Source	3.7×1.7, –48	47.6	B0V	–3.3±0.7	N214
053958.39-711005.5	19.4±4.0	0.30	S	N	···	···	<0.26	<0.18	···	···	47.6	···	···	N214
053958.52-711014.6	21.2±3.8	0.47	S	N	···	···	<0.26	<0.18	···	···	47.6	···	···	N214
053959.34-694526.3	18.9±2.2	–0.37	PE	N	···	···	<0.25	<0.18	···	···	47.6	···	···	N159
054000.69-694713.4	17.8±1.9	–0.38	PE	Y	05:40:00.606	–69:47:13.21	2.9±0.6	5.3±0.3	7.3×2.0, –66	3.8×2.3, –54	48.1	O9V	–1.2±0.4	N159
054004.40-694437.6	36.1±5.0	0.04	PE	Y	05:40:04.408	–69:44:37.34	55.2±2.5	64.7±2.5	3.0×2.8, 72	3.1×2.9, –74	49.2	O7V	–0.3±0.1	N159
054009.49-694453.5	23.3±2.3	0.29	PE	Y	05:40:09.503	–69:44:54.67	3.9±0.6	2.2±0.2	9.4×1.7, –65	8.7×2.1, –42	47.7	B0V	1.2±0.4	N159
054009.50-694023.0	17.0±2.0	0.09	PE	Y[f]	05:40:09.441	–69:40:25.01	···	39.9±4.2	···	15.4×12.6, –44	49.0	O7.5V	···	N159
054025.15-694012.1	···	0.02	PE	Y[f]	05:40:25.060	–69:40:12.53	···	61.6±6.1	···	10.1×7.9, 36	49.1	O7V	···	N159
YSOs from IJC04														
045153.29-692328.6	45.3±2.9	0.36	SE	Y	04:51:53.323	–69:23:28.84	152.5±9.9	135.1±6.3	2.1×0.6, 82	2.9×1.4, 78	49.5	O4V	0.2±0.1	N79
045200.43-692342.6	19.0±1.8	0.04	PE	Y	04:52:00.448	–69:23:42.40	64.9±16.7	6.4±2.9	10.7×2.1, –6	5.7×0.9, 86	48.2	O9V	3.9±0.9	N79
045201.15-692007.7	12.6±1.4	–0.50	F	N	···	···	<6.13	<2.13	···	···	48.2	···	···	N79
045204.56-692046.4	15.2±1.9	–0.01	PE	N	···	···	<6.13	<2.13	···	···	48.2	···	···	N79
045713.47-661900.1	9.8±1.2	–0.21	PE	N	···	···	<0.65	<0.92	···	···	48.2	···	···	N11A
050949.11-685230.6	17.8±4.3	–0.51	E	N	···	···	<2.48	<1.2	···	···	48.2	···	···	N105
050950.53-685305.5	41.7±4.4	0.18	P	Y	05:09:50.559	–68:53:05.29	40.0±1.9	26.9±1.3	Point Source	Point Source	48.8	O8V	0.7±0.1	N105
050952.26-685327.3	30.2±4.7	0.57	PE	Y	05:09:52.209	–68:53:26.00	2.9±0.6	18.6±4.0	7.3×2.0, –66	8.6×5.0, –82	48.6	O8V	–3.1±0.5	N105
050952.73-685300.7	27.9±3.9	0.06	PE	Y	05:09:52.867	–68:52:59.96	38.3±6.3	35.8±4.1	4.6×3.9, 24	4.7×2.9, –14	48.9	O7.5V	0.1±0.3	N105
050953.89-685336.7	19.7±2.6	0.40	P	N	···	···	<2.48	<1.2	···	···	48.9	···	···	N105
050954.63-684947.2	12.2±1.6	–0.15	P	N	···	···	<2.48	<1.2	···	···	48.9	···	···	N105
052216.87-680403.9	13.6±2.8	0.39	P	N	···	···	<0.61	<0.36	···	···	48.9	···	···	N44
052219.69-680437.4	19.0±2.0	0.09	PE	Y	05:22:19.640	–68:04:36.68	22.0±4.9	11.5±0.8	8.4×5.4, –56	4.2×3.5, 28	48.4	O8V	1.1±0.4	N44

Table 4.2 (cont'd)

IRAC Source[a]	$M_{\rm SED}$ ($M_\odot$)	Silicate[b] PCA	YSO[b] Group	D?[c]	RA (J2000)	DEC (J2000)	$F_{3\rm cm}$[d] (mJy)	$F_{6\rm cm}$[d] (mJy)	3 cm Size, PA[d] ($'' \times ''$)	6 cm Size, PA[d] ($'' \times ''$, $^\circ$)	log Q_0[e]	Sp.[e] Type	α	Region Name
052222.46-713532.2	17.0±3.3	0.18	F	N	···	···	<0.61	<0.36	···	···	48.4	···	···	N44
052232.65-680301.7	10.8±1.6	–0.45	P	N	···	···	<0.61	<0.36	···	···	48.4	···	···	N44
052249.13-680129.1	12.0±2.0	–0.14	PE	N	···	···	<0.61	<0.36	···	···	48.4	···	···	N44
052255.12-680409.4	17.6±2.1	–0.03	PE	Y	05:22:55.127	–68:04:09.22	2.9±0.3	3.1±0.3	1.6×1.2, 31	1.5×1.1, 68	47.8	B0V	–0.1±0.2	N44
052256.79-680406.8	13.2±1.7	–0.16	PE	N	···	···	<0.61	<0.36	···	···	47.8	···	···	N44
052308.60-680006.5	13.0±2.0	0.08	PE	N	···	···	<0.61	<0.36	···	···	47.8	···	···	N44
052315.18-680017.1	16.1±0.1	0.13	PE	Y	05:23:15.208	–68:00:16.79	<0.61	0.56±0.28	···	Point Source	47.1	B0.5V	···	N44
052331.37-680108.0	12.7±0.7	–0.10	PE	N	···	···	<0.61	<0.36	···	···	47.1	···	···	N44
052343.48-680033.9	24.8±5.2	0.35	P	Y[f]	05:23:43.481	–68:00:34.02	···	9.6±0.8	···	1.1×0.8, 4	48.3	O9V	···	N44
052504.10-682824.5	20.0±2.7	–0.16	E	I	···	···	···	···	···	···	48.3	···	···	N138
053020.32-710748.9	14.1±1.5	0.10	PE	Y[f]	05:30:20.392	–71:07:48.53	···	3.4±0.9	···	4.9×1.3, 65	47.9	B0V	···	N206
053020.79-710738.6	15.7±2.2	0.08	PE	Y[f]	05:30:20.563	–71:07:38.19	···	9.7±2.0	···	7.4×6.3, 66	48.3	O9V	···	N206
053023.18-710556.3	13.2±1.5	–0.08	PE	N	···	···	<0.47	<0.34	···	···	48.3	···	···	N206
053122.85-710409.9	18.8±1.9	–0.05	PE	Y	05:31:22.910	–71:04:08.90	4.1±0.9	3.2±0.8	5.6×3.8, 53	4.5×3.6, 48	47.9	B0V	0.4±0.6	N206
053232.06-662715.2	22.4±5.4	–0.18	PE	Y	05:32:31.942	–66:27:15.23	0.97±0.19	0.78±0.15	1.2×0.8, –40	Point Source	47.2	B0.5V	0.4±0.5	N55
053938.73-693904.3	24.5±3.6	0.36	PE	Y	05:39:38.771	–69:39:04.14	13.3±2.6	7.8±1.8	2.2×1.3, –23	1.3×0.9, 22	48.2	O9V	0.9±0.5	N160
053939.02-693911.4	33.1±3.1	0.64	PE	Y	05:39:39.012	–69:39:11.00	14.5±2.0	16.3±2.0	1.7×0.8, –18	2.4×1.2, –41	48.6	O8V	–0.2±0.3	N160
053959.51-693730.4	17.8±2.7	–0.55	P	N	···	···	<2.40	<2.0	···	···	48.6	···	···	N160
054004.19-693812.4	13.9±1.5	–0.16	PE	N	···	···	<2.40	<2.0	···	···	48.6	···	···	N160
054125.95-711753.9	13.8±1.1	–0.13	P	N	···	···	<0.47	<0.37	···	···	48.6	···	···	N214
054137.57-711902.0	18.6±2.6	–0.01	PE	Y	05:41:37.439	–71:19:01.45	18.9±1.4	18.9±1.2	6.5×5.3, 42	6.2×5.1, 47	48.6	O8V	–0.0±0.2	N214
054138.76-711913.9	16.3±1.2	–0.06	PE	N	···	···	<0.47	<0.37	···	···	48.6	···	···	N214
054520.03-694644.8	27.8±3.4	0.21	P	Y	05:45:20.034	–69:46:45.02	2.6±0.3	2.6±0.2	1.5×0.5, –23	Point Source	47.8	B0V	–0.0±0.3	N168
054527.92-694622.6	18.3±2.4	–0.24	PE	Y	05:45:27.805	–69:46:22.72	13.1±1.0	14.0±0.9	4.2×3.7, 21	4.1×3.6, 12	48.5	O8V	–0.1±0.2	N168

[a] *Spitzer* Infrared Array Camera (IRAC) designation from Gruendl & Chu (2009).

[b] These values/groups are from SL09.

[c] Is the source detected at 6 cm? Y: Yes, N: No, I: Indeterminate.

[d] Fitted parameter from `imfit`.

[e] Values were calculated for 6 cm only.

[f] Source was detected outside the FWHM of the 6 cm primary beam.

The location, size, and flux of each YSO's encompassing H II region was determined by fitting an elliptical Gaussian using the MIRIAD task `imfit`. This task was slightly modified to propagate the error for the integrated flux via covariance matrices. The methodology of fitting elliptical Gaussians to the continuum flux was typically found to be consistent with IJC04 within a few percent. One YSO, 045206.97-665516.4, could not be fit due to confusion with other nearby YSO H II regions. In Table 4.2, we also specify the sizes (observed major and minor axes deconvolved with the synthesized beam) at each wavelength as specified by `imfit`. According to the sizes of our sources (and, as will be discussed later, densities and emission measures), Habing & Israel (1979) would classify most of our sources as "dense" H II regions, though some sources are more consistent with "classical" H II regions and many of the unresolved sources may be classified as compact or UC.

In addition, we use the MIRIAD task `maxfit` to fit the location and quantity of the peak flux value for each YSO's H II region. The locations of the peak source is listed in Table 4.2 for 6 cm. The 6 cm locations were preferred over 3 cm since the observations have better sensitivity, had better phases during data reduction, and have a comparable resolution to *Spitzer*. These locations are fairly consistent with *Spitzer* locations, though at times they can be off by $\sim 2''$ which indicates that *Spitzer* and ATCA observations sometimes could be sampling different sources. However, these sources typically have 8 μm emission elongated in the direction of the free-free emission. Moreover, simulations by Peters et al. (2010b) showed that the H II emission peak does not always coincide with the YSO location, albeit their discrepancy was found at a much smaller size scale than probed by our resolution. The peak flux values for both 3 cm and 6 cm are shown in Table 4.3.

It is also worth mentioning that in many of our fields, there are other continuum sources that are detected which are not listed in these tables. These sources do not have *Spitzer* IRS observations from SL09, and therefore are not included in our study. Many of these sources are likely massive YSOs based on their physical properties (e.g., spectral indices, IJC04, Martín-Hernández et al. 2005), but for a more uniform survey, these sources have been excluded.

4.3 Results

4.3.1 Detections

In order to determine whether a YSO is massive enough to create a detectable H II region, the detection threshold of the observations needs to be assessed. Using Equation 4.1 (Condon 1992), we are able to estimate the hydrogen ionizing flux (Q_0) for a given sensitivity. Note that this equation assumes that the

region is optically thin which may underestimate the detection limit, though most sources are expected to be optically thin unless they are HC. We are concerned with a significant H II detection (3σ), so we estimate the ionizing luminosity of three times the sensitivity of an observation (i.e., $L_{\rm thermal} = 4\pi d^2(3\sigma)$, where d is the distance to the LMC). From these ionizing flux values, we approximate the spectral type from Smith et al. (2002) using a metallicity representative of the LMC of 0.4 $Z_\odot$. The masses for each spectral type were estimated using Habets & Heintze (1981) and then compared to $M_{\rm SED}$ in order to predict whether an H II region should be detected around the YSO. The detection limit for our observations is close to a B1V star ($\sim$12 $M_\odot$) and those from IJC04 were either a B0.5V or a B0V ($\sim$14 and 15.6 $M_\odot$ respectively). Figure 4.2 shows silicate PCA strength versus $M_{\rm SED}$ which is color-coded to show detections. The approximate detection thresholds are shown by dashed lines.

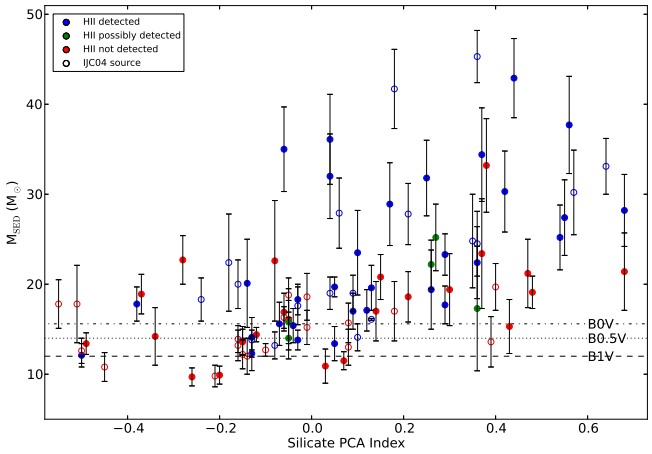

Figure 4.2 $M_{\rm SED}$ versus silicate PCA strength (>0.2 implies strong absorption, <0.0 implies weak to no absorption) for YSOs. For more positive silicate PCA strengths, sources are more embedded and likely younger. Blue circles show 6 cm H II continuum detections while red and green circles show 6 cm non-detections and indeterminate detections respectively for YSOs within the FWHM of the primary beam. Solid circles show observations from this study while open circles are from IJC04. Dashed lines show approximate detection limits for our observations (B0V) and IJC04 observations (B0.5V and B1V).

$$Q_0 \geq 6.3 \times 10^{52} s^{-1} \left(\frac{T_e}{10^4 \mathrm{K}}\right)^{-0.45} \left(\frac{\nu}{\mathrm{GHz}}\right)^{0.1} \frac{L_{\rm thermal}}{10^{27} \mathrm{erg\,s^{-1}Hz^{-1}}} \tag{4.1}$$

If every YSO is expected to have an H II region, this simplistic analysis implies that we have a few less detections than expected; however, most of these massive YSOs that have the possibility to be detected indeed have an H II region around them. There are many reasons why we might not see detection around all of these sources. We may have inaccurate $M_{\rm SED}$ calculations or mass estimates and Q_0 values from Habets & Heintze (1981) and Smith et al. (2002) may be somewhat imprecise. Some sources may be optically thick (perhaps HC H II regions, which often require millimeter observations) or have high accretion rates.

Perhaps some sources have not yet ionized enough material to create a detectable H II region or have an overestimation in mass due to multiplicity. Regardless, there is still agreement between $M_{\rm SED}$ and whether or not there are detections.

Since large-scale structure can be resolved out by the interferometer at 3 cm more than 6 cm, 6 cm was our primary means for calculating Q_0 for each YSO. Q_0 was calculated using Equation 4.1 with $L_{\rm thermal} = 4\pi d^2 F_{\rm 6cm}$. This ionizing flux is typically underestimated for at least four reasons: (1) the formula assumes the source is optically thin, (2) large-scale emission can be resolved out, (3) the implemented fitting task, `imfit`, fits a Gaussian to the densest region and does not add the additional extended emission, and (4) it is often found that Q_0 has $\gtrsim 30\%$ of the ionizing photons absorbed by dust (e.g., WC89, KK01). We select the spectral type for each source using Smith et al. (2002) for metallicity $0.4Z_\odot$, picking the later spectral types for Q_0 values in between spectral types. Q_0 values and the associated spectral types for each YSO is listed in Table 4.2.

To further test the accuracy of the $M_{\rm SED}$ mass estimates, we match the $M_{\rm SED}$ to spectral types from Martins et al. (2005) for luminosity class V. Martins et al. (2005) only modeled sources of solar metallicity, but this study may have the most accurate O-star estimates of masses to date. We also match our estimated Q_0 to the spectral types of this same study and find that on average the spectral types are off by about 1 subclass (e.g., O6.5 – O5.5 = 1 subclass). In a few situations, the spectral types could be off by a few, especially the source 051912.27-690907.3 whose mass spectral type is estimated to be ∼O5V, but the ionizing flux indicates that it is a B star. This discrepancy does not necessarily indicate inaccuracy of the Robitaille et al. (2007) model; e.g., this source could have large extinction and/or strong accretion which may cause the free-free emission to be reduced. Moreover, it is seen amongst the whole sample that typically the spectral type from $M_{\rm SED}$ is a bit earlier than the spectral type from Q_0. This indicates that perhaps $M_{\rm SED}$ is overestimated and/or Q_0 is underestimated. The latter is certainly plausible given our discussion in the previous paragraph. Overall, however, $M_{\rm SED}$ appears to be fairly accurate.

4.3.2 Fluxes

Integrated fluxes at 3 and 6 cm are compared to $M_{\rm SED}$ in Figure 4.3. SED groups from SL09 (as explained in Section 4.2.2) are plotted next to each point. For both wavelengths, there is a positive correlation between the logs of F_ν and $M_{\rm SED}$. In both graphs, however, there exists an S Group point at 37.7 $M_\odot$ (the source 051912.27-690907.3 mentioned in Section 4.3.1) that is well below the expected flux. Other S and F Group points also show below average fluxes in the graph. These groups lack fine structure lines and PAH emission, which may indicate less excitation in the area. Thus, it is expected that the flux of these regions would

be slightly lower. Moreover, if we only consider sources below ∼25 $M_{\odot}$, there would be little correlation in the relationship due to the six PE sources in the top left of the graph. The fluxes for these PE sources are surprisingly high for their masses, though having high PAH and fine structure line emission in their spectra may be indicative of their large fluxes. Nevertheless, for these six sources, we cannot find anything particularly unique about their *Spitzer* spectra.

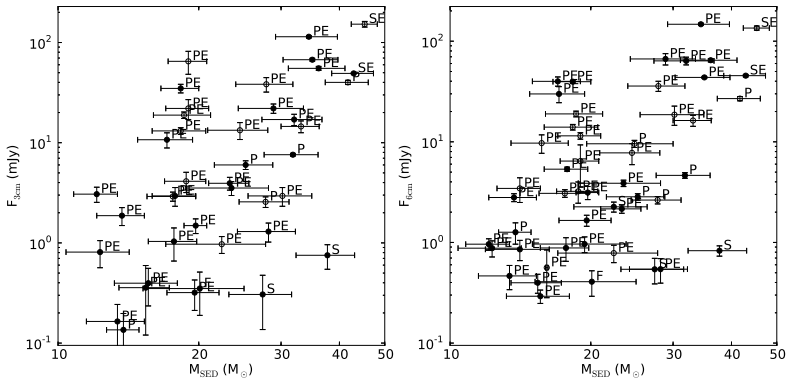

Figure 4.3 Integrated fluxes for 3 and 6 cm versus $M_{\rm SED}$. Labels indicate SL09 YSO classification. Solid circles are observations from this study while empty circles are sources from IJC04.

Though we present the graphs on a log-log plot, which is indicative of a power-law, this data is just as significantly fit by an exponential. Basic fits (i.e., error bars of each point is not taken into account) to power-laws are $F_{\rm 3cm} = 3.4 \times 10^{-4} M_{\rm SED}^{3.0\pm0.71}$ and $F_{\rm 6cm} = 1.1 \times 10^{-3} M_{\rm SED}^{2.7\pm0.61}$ and to exponentials are $F_{\rm 3cm} = 0.24{\rm e}^{(0.12\pm0.029){\rm M_{SED}}}$ and $F_{\rm 6cm} = 0.36{\rm e}^{(0.11\pm0.025){\rm M_{SED}}}$. The theoretical expectation for this relationship is not completely straightforward. If we assume the regions are optically thin, flux is directly related to Q_0. The relationship of mass and Q_0 for massive stars depends on the model and a single power-law or exponential does not well fit the theoretical expectations. Generally a single-power law fits better than an exponential. If we use the models from Martins et al. (2005) to compare Q_0 with the spectroscopic mass, $M_{\rm spec}$, using theoretical and observational scales of effective temperatures ($T_{\rm eff}$), we find relationships of $Q_0 \propto M_{\rm spec}^{3.8\pm0.23}$ and $Q_0 \propto M_{\rm spec}^{3.0\pm0.14}$ respectively. Our data appear to be more consistent with $T_{\rm eff}$ derived from observations rather than theory.

For free-free emission, the spectral index, α (where $F_\nu \propto \nu^\alpha$), is expected to be between –0.1 (optically thin) and 2 (optically thick). We have calculated α for our YSO H II regions as seen in Table 4.2. Since 6 cm observations are more sensitive to large scale structure than 3 cm, these spectral indices are sometimes underestimated. We note that spectral indices that are very negative (<–1) tend to occur in regions that are exceptionally large or for which the 3 cm observations will resolve the 6 cm observations into more sources, causing the `imfit` task to fit different morphologies. Figure 4.4 shows spectral indices as a function of the

diameter of the model sphere, D (as explained in Section 4.3.4). Spectral indices have a slight tendency to be more negative for larger source sizes which is attributed to resolving out emission or resolving the emission into multiple sources at 3 cm.

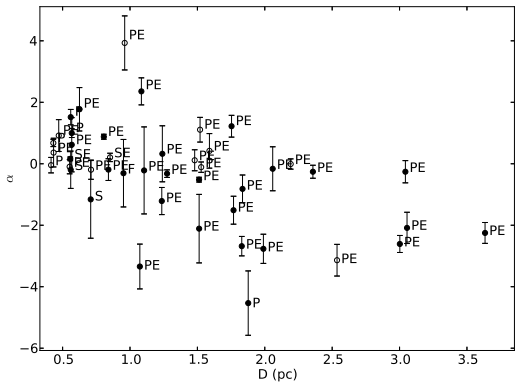

Figure 4.4 Spectral indices versus fitted sizes of sources. Labels indicate SL09 YSO classification. Solid circles are observations from this study while empty circles are sources from IJC04.

4.3.3 Sizes

As discussed previously, we fit sizes to all of our sources with MIRIAD's `imfit` task at both 3 and 6 cm. Figure 4.5 shows the deconvolved major and minor axes versus the silicate PCA strength. Sizes of the circles are proportional to $M_{\rm SED}$. Though resolution can vary from region to region and our synthesized beam can have various eccentricities, we used dashed lines to represent a resolution of $2''$ and $3''$ for 3 and 6 cm respectively. Sizes below these lines are roughly unresolved in at least one dimension.

It is evident from these plots that sources with high silicate PCA strength ($\gtrsim$0.3) are much less likely to have one axis resolved. At 6 cm, we find that sources with strong silicate absorption (silicate PCA strength of ≥ 0.2) have major axis sizes above $3''$ (0.75 pc) only 41$\pm$12% of the time, while the rest of the sources have major axes above $3''$ 81$\pm$7% of the time[1]. This result may indicate that YSOs with silicate absorption, which are likely younger sources, have had less time to evolve its H II region. However, we note that these unresolved YSOs are also typically more massive, so the causal effect could depend on mass rather than age.

We find that that the eccentricities of the fully resolved sources (sources with major and minor axes above $3''$ at 6 cm) are indicative of non-spherical sources. Out of 16 fully resolved sources at 6 cm, 13 sources have eccentricities over 0.5. This result, however, is not different than WC89 and Kurtz et al. (1994), where 36 out of 51 of their resolved spherical sources have eccentricities above 0.5. Though typically modeled as spheres, these UC H II and our H II regions are likely better modeled as ellipsoids. The presence of circular

[1]Errors are calculated via the standard error of percentages.

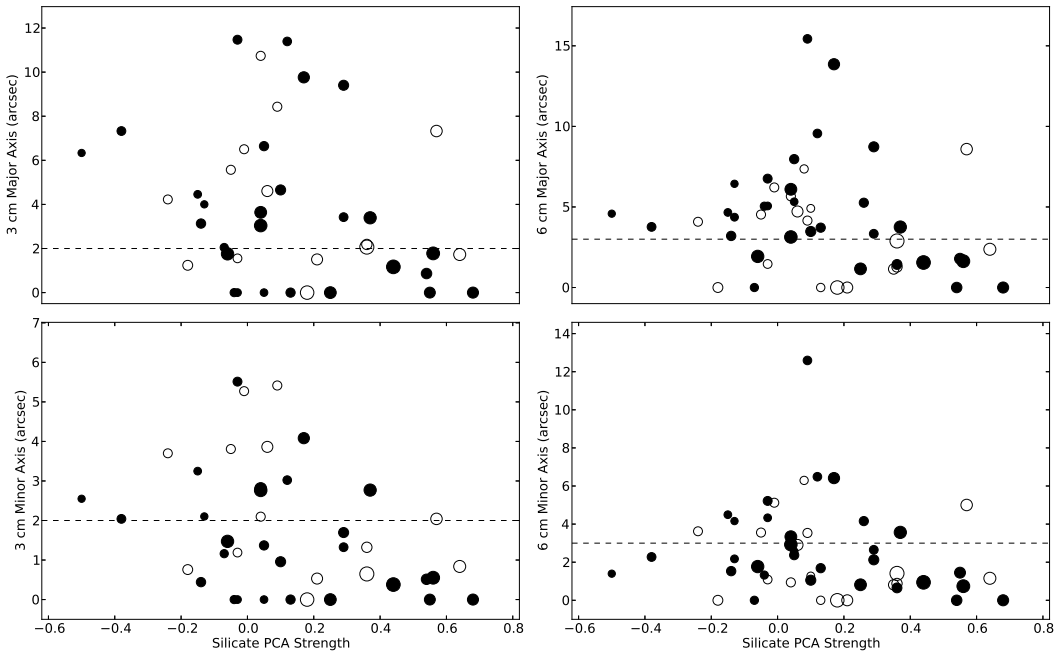

Figure 4.5 Fitted axes of sources versus Silicate PCA Strength. The dashed lines shows the approximate resolution of the observations ($\sim 3''$ and $2''$ at 3 and 6 cm respectively). Labels indicate SL09 YSO classification. Solid circles are observations from this study while empty circles are sources from IJC04. Sizes of the circles are proportional to $M_{\rm SED}$.

morphologies in these samples may not be indicative of a spherical morphology; rather, the observer may be looking at two similar dimensions of the ellipsoid (i.e., approximately a spheroid), with the long axis parallel to the line of sight.

Since accretion is higher about a disk than the poles, ionization is preferential about the poles. This mechanism causes two smaller (and similar) dimensions about the disk plane and a larger dimension about the poles, allowing the ellipsoid to take shape of a prolate spheroid. However, multiple massive YSOs within a region can have their H II regions combine into a single H II region. Since YSOs tend to form with their rotation axes approximately parallel to each other (e.g., Peters et al. 2010a), the combination of H II regions tend to extend about their disks. This extension is perpendicular to the extension of a single YSO's prolate spheroid, which can work to make the region appear more spherical or even create a prolate spheroid extended along the disk plane rather than the poles. Indeed, the simulations of Peters et al. (2010a) showed that for a single YSO, the continuum is preferentially extended about one or both poles, but for a combination of YSOs, the H II region extends about the disk plane. Given the size-scale of our region, these simulations suggest that our regions are prolate spheroids with the longest axis about the disk plane.

Moreover, with different regions containing different multiplicities and containing YSOs and H II regions with a variety of masses and multiplicities, the H II regions can form irregular shapes. Such regions are

apparent in our sample (e.g., Figure 4.18), though the central regions are generally well fit by a Gaussian.

4.3.4 Densities

As discussed in the previous section, these H II regions may be spheroids, and the depth along the line of sight for these spheroids is unknown. However, assuming a sphere simplifies the process of calculating the densities of each H II region. Like WC89, we calculate the rms electron density using two methods: one that has an emission measure, EM, that depends on a spherical morphology and another whose EM is independent of the morphology. We use an electron temperature of $T_e = 10^4$ K for all calculations and show computed values in Table 4.3. In all situations we use 6 cm values due to higher sensitivity, more trustworthy fluxes due to the less attenuation in the larger primary beam and better calibration, and more comparable resolution with *Spitzer*. Though not shown, calculations were also computed for 3 cm fluxes and were found to be consistent with our 6 cm values. However, for the point source-like sources, 3 cm densities could be up to a factor 5 higher.

Table 4.3. Derived YSO Parameters from Fitted 6 cm Continuum Observations

		from 6 cm integrated flux density						from peak 6 cm flux density per synthesized beam			
IRAC Source[a]	Sphere Diameter (pc)	EM/10^4 (pc cm^{-6})	n_e (cm^{-3})	U (pc cm^{-2})	Peak 3 cm Flux Density (mJy bm^{-1})	Peak 6 cm Flux Density (mJy bm^{-1})	Δs (pc)	T_b (K)	τ_ν	EM/10^4 (pc cm^{-6})	N_e (cm^{-3})
045111.39-692646.7	0.71	4.3	294	15.6	0.38	0.45	0.39	2.9	0.000	3.1	284
045205.39-665513.8	3.06	12.9	244	59.6	0.95	3.21	1.91	20.8	0.002	22.8	345
045209.22-665521.9	3.63	20.3	280	77.8	1.91	5.14	2.29	33.4	0.003	36.6	400
045358.57-691106.7	<0.56	>36.4	>957	27.2	5.13	2.97	<0.30	19.1	>0.002	>20.9	>830
045426.06-691102.3	0.81	270.2	2174	67.6	31.73	28.68	0.45	184.3	0.019	203.5	2131
045550.62-663434.6	<0.57	>28.0	>833	25.2	···	1.98	<0.31	12.3	>0.001	>13.5	>662
045625.99-663155.5	2.06	0.8	75	18.4	0.24	0.17	1.25	1.1	0.000	1.2	96
045629.02-663159.3	1.51	0.8	87	14.9	0.19	0.15	0.90	1.0	0.000	1.1	108
045640.79-663230.5	0.95	1.8	164	14.2	0.21	0.27	0.54	1.7	0.000	1.8	184
045647.23-662431.8	3.04	6.7	177	47.9	0.77	1.96	1.89	9.9	0.001	10.9	240
045657.25-662513.0	0.84	22.1	609	30.2	1.80	2.77	0.46	14.0	0.001	15.3	574
045659.85-662425.9	1.08	3.3	207	19.0	0.56	0.56	0.61	2.8	0.000	3.1	225
045716.25-662319.9	2.36	28.6	414	65.4	2.41	7.81	1.44	39.5	0.004	43.3	549
045742.00-662634.4	<0.57	>3.6	>301	12.7	0.24	0.32	<0.31	2.0	>0.000	>2.2	>268
045747.68-662816.9	1.88	1.1	91	19.0	···	0.25	1.13	1.5	0.000	1.7	122
045749.22-662900.3	1.88	1.4	104	20.8	0.20	0.39	1.13	2.5	0.000	2.7	154
051351.51-672721.9	<0.57	>57.9	>1199	32.0	7.24	4.15	<0.31	25.9	>0.003	>28.4	>960
051912.27-690907.3	<0.56	>10.6	>516	18.0	0.56	0.72	<0.30	4.6	>0.000	>5.1	>408
052202.11-675753.6	1.24	2.3	162	18.4	0.43	0.44	0.72	2.9	0.000	3.1	209
052207.27-675819.7	1.28	2.1	152	18.2	···	0.38	0.75	2.5	0.000	2.7	191
052212.57-675832.4	<0.56	>588.8	>3860	68.5	40.17	37.47	<0.30	243.6	>0.025	>269.8	>2988
052757.09-672522.3	1.83	3.3	160	27.1	0.28	0.70	1.11	4.6	0.000	5.0	212
053904.88-692949.9	1.10	1.3	129	14.1	0.21	0.20	0.63	1.1	0.000	1.2	136
053915.77-693039.9	3.00	11.0	227	55.9	0.65	2.82	1.86	14.8	0.001	16.2	294
053937.04-694536.7	<0.63	>5.6	>355	15.7	1.08	0.59	<0.34	3.0	>0.000	>3.3	>313
053937.53-694609.8	1.83	76.5	768	76.7	5.08	15.46	1.09	79.8	0.008	87.7	895
053937.60-694525.0	1.51	258.8	1553	101.4	26.22	49.9	0.89	257.5	0.026	285.5	1794
053945.18-694450.4	1.77	4.0	179	28.1	0.37	1.07	1.05	5.5	0.001	6.0	239
053951.60-694510.5	1.99	6.2	209	35.0	0.39	1.49	1.20	7.7	0.001	8.4	265
053955.66-711000.9	1.07	5.8	275	22.7	0.36	0.95	0.61	4.9	0.000	5.3	296
054000.69-694713.4	1.24	14.1	401	33.6	0.74	2.58	0.71	13.3	0.001	14.6	453
054004.40-694437.6	1.27	159.9	1330	77.1	12.97	26.13	0.73	134.9	0.014	148.6	1423
054009.49-694453.5	1.75	2.8	151	24.8	0.70	0.68	1.04	3.5	0.000	3.8	191
054009.50-694023.0	5.34	5.6	122	65.6	···	2.74	3.38	14.1	0.001	15.5	214
054025.15-694012.1	3.47	20.6	290	75.8	···	7.51	2.17	38.7	0.004	42.5	443
YSOs from IJC04											
045153.29-692328.6	0.85	747.8	3517	98.5	90.89	66.2	0.49	738.6	0.077	630.8	3590
045200.43-692342.6	0.96	28.0	641	35.7	6.12	1.83	0.56	20.4	0.002	16.8	548
050950.53-685305.5	<0.43	>581.5	>4361	57.5	37.84	26.91	<0.23	292.0	>0.030	>243.6	>3228
050952.26-685327.3	2.54	11.6	254	50.9	2.01	2.00	1.59	21.7	0.002	17.9	335
050952.73-685300.7	1.48	65.8	791	63.3	6.63	10.17	0.90	110.3	0.011	91.2	1008
052219.69-680437.4	1.52	19.9	430	43.3	1.45	2.30	0.93	28.7	0.003	23.6	504
052255.12-680409.4	0.55	40.5	1017	27.9	1.68	2.12	0.31	26.3	0.003	21.7	842
052315.18-680017.1	<0.40	>13.9	>699	15.8	···	0.61	<0.22	7.6	>0.001	>6.2	>534
052343.48-680033.9	0.43	207.8	2609	40.8	···	7.75	0.23	96.5	0.010	79.7	1845
053020.32-710748.9	1.03	13.0	422	29.0	···	1.21	0.61	14.3	0.001	11.8	441
053020.79-710738.6	2.63	5.7	174	41.0	···	1.08	1.65	12.7	0.001	10.5	252

Table 4.3 (cont'd)

		from 6 cm integrated flux density						from peak 6 cm flux density per synthesized beam			
IRAC Source[a]	Sphere Diameter (pc)	EM/10^4 (pc cm^{-6})	n_e (cm^{-3})	U (pc cm^{-2})	Peak 3 cm Flux Density (mJy bm^{-1})	Peak 6 cm Flux Density (mJy bm^{-1})	Δs (pc)	T_b (K)	τ_ν	EM/10^4 (pc cm^{-6})	N_e (cm^{-3})
053122.85-710409.9	1.59	5.1	213	28.4	0.69	0.78	0.97	9.2	0.001	7.6	280
053232.06-662715.2	<0.43	>16.8	>739	17.7	0.71	0.81	<0.23	8.7	>0.001	>7.2	>552
053938.73-693904.3	0.47	140.5	2050	38.0	6.58	6.23	0.26	71.6	0.007	59.1	1515
053939.02-693911.4	0.71	129.6	1603	48.7	8.72	9.14	0.40	105.1	0.011	86.9	1471
054137.57-711902.0	2.19	15.8	319	51.2	1.84	2.05	1.37	24.1	0.002	19.8	381
054520.03-694644.8	<0.41	>61.7	>1449	26.5	1.84	2.28	<0.22	26.8	>0.003	>22.1	>991
054527.92-694622.6	1.53	24.1	471	46.3	2.32	3.35	0.93	39.3	0.004	32.4	589

[a]Designation from Gruendl & Chu (2009).

The first method uses the modified Mezger & Henderson (1967) equations from Panagia & Walmsley (1978), which approximates the H II regions as spheres that are optically thin, homogeneous, dust-free, and ionization-bounded. The diameter of this modeled sphere can be calculated from the Gaussian fit of the source, but a scaling factor must be applied that takes into the account the size of the synthesized beam. For H II regions, the most commonly applied correction factor is discussed in Panagia & Walmsley (1978); however, we use the spherical correction factor from van Hoof (2000) since the calculation is more straightforward and likely more accurate. It is noted, however, that this correction factor does assume a circular beam, while our beams can sometimes have high eccentricities; we use the geometric mean of the FWHM of the synthesized beam major and minor axes, θ_B, as an approximation of the beam size. We apply this correction factor to the geometric mean of the deconvolved Gaussian axes, θ_D, to approximate the modeled sphere diameter, D, and show the tabulation in Table 4.3. When θ_B is more than twice the size of θ_D, we use $\theta_B/2$ as an upper bound to θ_D. Along with these modeled sphere diameters, we use the 6 cm integrated fluxes to calculate the EM and rms electron density (n_e). From n_e we can also calculate the excitation parameter, $U = rn_e^{2/3}$, which is independent of source geometry.

The second method, as described in WC89, calculates the "peak physical properties" and allows a calculation of the EM that is independent of geometry. The brightness temperature, T_b, is calculated from the peak flux intensity using the Rayleigh Jeans approximation and is used to calculate the optical depth, τ_ν, given $T_b = T_e(1-e^{-\tau_\nu})$. The peak EM is calculated from τ_ν using the formula from Mezger & Henderson (1967) and is used to calculate the peak rms electron density, $N_e = (\mathrm{EM}/\Delta\mathrm{s})^{1/2}$. For our sources, we approximate the line of sight depth along the peak position, Δs, to be equal to θ_D. Again, $\theta_B/2$ is used as an upper bound for Δs when $\theta_B > 2\theta_D$. N_e and n_e provide very similar values, which indicates consistency between the two methods, though for most comparisons we show in this paper, we will primarily use n_e.

Our densities are indicative of "dense" H II regions, but they could contain UC H II regions that do not add enough flux to the extended H II region to dominate our fits. Indeed, ionizing fluxes calculated by KK01

of compact/extended regions are much higher than the UC H II counterpart. As a test, we used MIRIAD task `uvmodel` to place an UC H II point source in our H II region and find that our sources can still be fitted with similar sizes and densities. However, extended sources less than ∼1 mJy are not likely to have an UC H II region since the dense core would dominate the fit. Nevertheless, it is possible and maybe even likely that most of these H II regions are harboring UC H II regions consistent with hierarchical structure discussed in KK01 (as discussed in Section 4.1).

Density and Excitation Parameter versus Mass

Figure 4.6 shows the relationship between the log of $M_{\rm SED}$ and the log of both n_e and N_e. Both power-law and exponentials give comparable fits. The power-law fits are $n_e = 0.38 M_{\rm SED}^{2.3\pm0.29}$ and $N_e = 0.96 M_{\rm SED}^{2.0\pm0.24}$ and the exponential fits are $n_e = 50{\rm e}^{(0.09\pm0.012){\rm M_{SED}}}$ and $N_e = 69{\rm e}^{(0.08\pm0.010){\rm M_{SED}}}$.

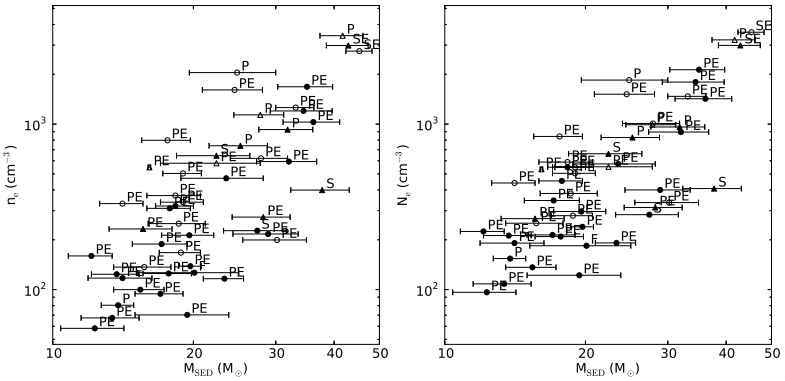

Figure 4.6 Plot of n_e and N_e versus $M_{\rm SED}$. Triangles represent unresolved sources and show the lower limits for n_e and N_e. Labels indicate SL09 YSO classification. Solid shapes are observations from this study while empty shapes are sources from IJC04.

Spectral types are often associated with theoretical stellar parameters and can be directly compared to our values of $M_{\rm SED}$ and U. From the Martins et al. (2005) values of the ionizing fluxes of class V stars, we calculate values of U for each O-star using the formula from Panagia (1973) for $T_e = 10^4$ K. In Figure 4.7 we show the plot U versus $M_{\rm SED}$ for our observations and U versus $M_{\rm spec}$ for Martins et al. (2005) models for both theoretical and observational $T_{\rm eff}$. SL09 YSO classifications are not shown to make the plot clear, but once again, the bottom right outlier is the S Group source 051912.27-690907.3. Though the Martins et al. (2005) data is best fit with a logarithmic function, the spread in our data causes difficulty in picking an accurate fit. Still there is an slight positive correlation exists in our data between U and $M_{\rm SED}$ (adjusted coefficient of determination $\bar{R}^2$=0.35, or $\bar{R}^2$=0.42 with outlier removed), and the modeled parameters are in the same general vicinity as our YSOs.

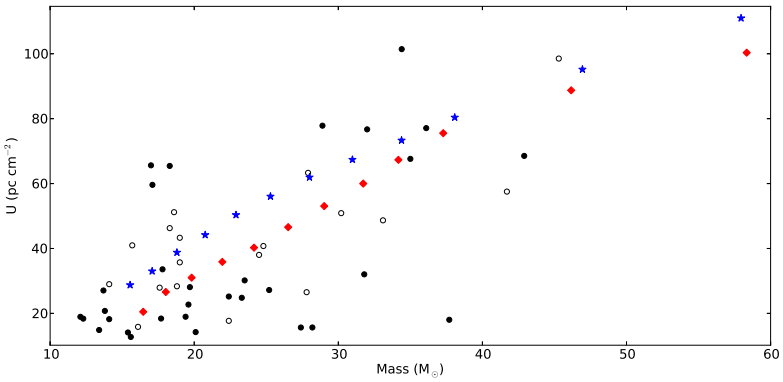

Figure 4.7 Plot of U versus mass. The circles use $M_{\rm SED}$ for mass, with the solid circles coming from this study and the empty circles coming from IJC04. Red diamonds and blue stars are from Martins et al. (2005) and use theoretical and observational $T_{\rm eff}$ respectively and use $M_{\rm spec}$ for mass.

Density versus Size

In the classic Strömgren sphere model, given a constant Q_0, the expected density versus size relationship is $n_e \propto D^{-1.5}$. However, observations frequently show that such a relationship is not the case, with both Galactic and extragalactic H II regions showing a power-law closer to $n_e \propto D^{-1}$ (e.g., Garay & Lizano 1999, KK01, Martín-Hernández et al. 2005, Hunt & Hirashita 2009). We have plotted n_e versus D in Figure 4.8. Compared to most plots of this relationship in other studies, our plot shows more scatter with $\bar{R}^2$=0.42; however, we find the typical D^{-1} power-law of $n_e = 510 D^{-1.0\pm0.17}$. The coefficient of 510 is lower than the one found by KK01 of 790 and is likely due to the inclusion of YSOs with much lower ionization flux, which is particularly evident in Figure 4.8 since larger shapes indicate larger values of Q_0, and there is an obvious increase of Q_0 toward the top-right.

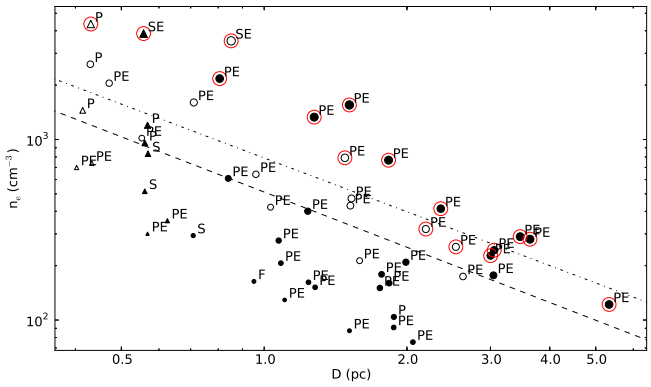

Figure 4.8 Log-log plot of n_e against D. The dashed line shows the power-law fit to our data of $n_e = 510 D^{-1.0}$, while the dot-dashed line shows the relationship $n_e = 790 D^{-0.99}$ from KK01. Triangles represent unresolved sources and show the upper and lower limits of D and n_e respectively. Labels indicate SL09 YSO classification. Solid shapes are observations from this study while empty shapes are sources from IJC04. Larger shapes indicate higher values of Q_0 and are circled in red for log $Q_0 \geq 48.59$.

The reason for the –1 power-law index instead of the –1.5 index is unclear, though suggestions include a champagne flow model combined with hierarchical structure (KK01) and dust absorption and radiation pressure (Arthur et al. 2004; Dopita et al. 2006). However, Draine (2011) showed model fits compared with a variety of H II observations and stressed that observations of different Q_0 should not have a single n_e versus D relationship; the relationship $n_e \propto D^{-1}$ is purely due to sample selection. Our observations sample a variety of ionizing fluxes (values of log Q_0 ranging from 46.8 to 49.5), which is the reason we see appreciable scatter in Figure 4.8.

The KK01 fits includes ancillary data that shows much more spread about their fitted line than the observations made in KK01. We have circled the sources in red for ionizing fluxes similar to the observations in KK01 (i.e., the non-ancillary data); these 16 circled sources follow the fit $n_e = 1650 D^{-1.6\pm0.11}$ with $\bar{R}^2 = 0.93$, which is significantly different than the KK01 fit. We note, however, that KK01's larger (extended) regions have *much* higher ionizing fluxes than their smaller (compact) regions, which systematically causes their power-law index to be lower. Our red circled observations have a much more uniform distribution of Q_0 at all sizes and follows a power-law more comparable to Draine (2011). Thus, though we still see the –1 power-law index for all sources, we believe this is at least partially by chance, and our results are more comparable to the analysis by Draine (2011).

Density versus Silicate PCA Strength

Figure 4.9 shows the relationship between n_e and silicate PCA strength. Higher PCA silicate strengths (particular those with $\gtrsim$0.3, indicating very strong silicate absorption) tend to have higher densities. This trend makes sense since these objects are expected to be more embedded and thus have not yet cleared their envelope. As shown earlier, however, there is a mass-density power-law relationship and larger silicate indices tend to have higher masses which produces a bias in exploring a density and silicate PCA strength trend. Regardless, along with the fact that high silicate indices are less likely to be resolved, the embedded (and likely younger) sources appear to have smaller and more compact H II regions than the less embedded sources, indicating evolving H II regions.

Densities and IR Magnitudes

A common selection criteria for finding UC H II uses absolute IR flux and color. As an example, Kurtz et al. (1994) selected fields from Infrared Astronomical Satellite (commonly known as IRAS) with $\log(F_{60}/F_{12}) \geq 1.30$, $\log(F_{25}/F_{12}) \geq 0.57$, and $F_{100} \geq 1000$ Jy. *Spitzer* observations and our H II regions have comparable resolutions that provide the opportunities to directly compare magnitudes and colors with free-free emission.

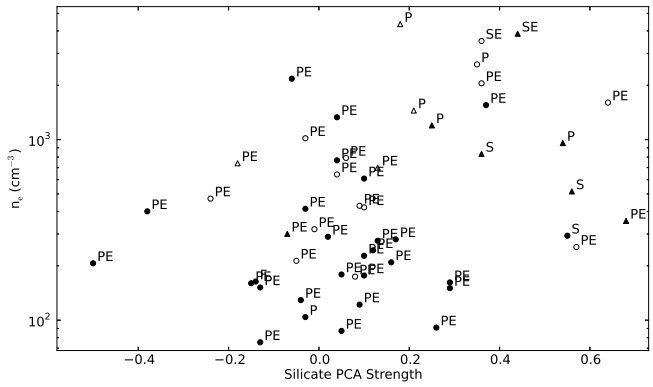

Figure 4.9 Plot of n_e against silicate PCA strength. Triangles represent unresolved sources and show the lower limits of n_e. Labels indicate SL09 YSO classification. Solid shapes are observations from this study while empty shapes are sources from IJC04.

Since we have already compared the parameters of our H II region to M_{SED} and higher M_{SED} have higher IR fluxes, it is unnecessary to draw comparisons that are the same as discussed herein (e.g., higher 8 μm fluxes have higher densities). However, colors, which may be related to physical parameters (e.g., temperature), may provide stronger insight on some parameters.

Our sources have already been selected in Gruendl & Chu (2009) based on the color criteria [4.5]–[8.0] > 2.0. Given this criteria, we have looked at every IR color combination for the central IRAC band wavelengths of 3.6, 4.5, 5.8, 8.0, and 24 μm and have compared them against all parameters discussed in this paper. No correlation is found between colors of the shorter wavelength bands (3.6, 4.5, 5.8, and 8.0 μm) and H II region parameters. Slight color correlations are seen when we subtract the magnitudes of the longer wavelength band (24 μm) from each of the shorter wavelengths for most fitted parameters (though not D or α). An example of one of the correlations is seen in Figure 4.10.

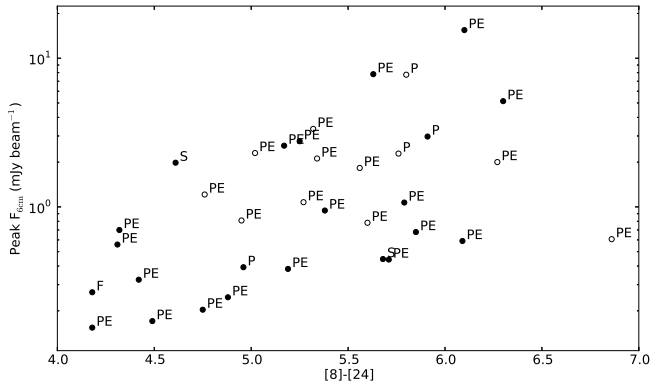

Figure 4.10 Plot of peak 6 cm flux density against the color [8]-[24]. Labels indicate SL09 YSO classification. Solid circles are observations from this study while empty circles are sources from IJC04.

Color relationships between other wavelengths and the 24 μm band are not surprising; as shown in Wood & Churchwell (1989b), UC H II regions tend to have the highest values of F_{25}/F_{12} and F_{60}/F_{12}. However, 70 μm *Spitzer* observations for most of our sources were not available in Gruendl & Chu (2009), and these observations certainly would not resolve our YSOs. The lack of correlation with colors of the shorter *Spitzer* wavelength bands is at least partially due to the fact that YSOs can have various levels of contamination of fine structure lines and PAH in different bands. While 24 μm spectra can vary (SL09), such contamination is not prominent at that wavelength.

4.3.5 Age of YSO H II Regions

As discussed previously, WC89 showed that UC H II regions last much longer than that which is estimated from dynamical expansion; thus, something slows down the growth of the UC H II region. Extended emission associated with these UC H II regions, however, may expand dynamically (e.g., KK01) and the sound-crossing time may be an accurate estimate of the age of the YSO's hierarchical H II region. Our Gaussian fits sometimes fit the more compact emission rather than the extended emission, which expands slower than dynamical expansion. Thus, when we estimate the sound-crossing times for the age of our H II regions, these estimates are generally lower bounds.

To estimate the typical and maximum age of an H II region for a given spectral type, we bin our sources based on their measured Q_0. In each bin, we find the median and maximum radius, $R = D/2$, and calculate the sound crossing time for a sound speed of 10 km s^{-1}. In Table 4.4 we show the tabulated lifetimes for each bin, with $t_{\rm median}$ representing the typical age and $t_{\rm max}$ representing the maximum age of the YSO H II regions; again, these ages are likely underestimated. $t_{\rm max}$ estimates a lower-bound of the maximum age since even the largest region in the bin may still be expanding. We also note that our binning methodology is slightly erroneous since YSOs are still accreting mass (possibly up to $\sim$10^{-3} $M_\odot$ yr^{-1}). Thus, the $t_{\rm max}$ for a given spectral type may come from a different spectral type as probed by the $t_{\rm median}$ in the same bin.

We find that the H II regions typically have ages $> 10^5$ yr, which is consistent with KK01. Since stars with more mass always have shorter lifetimes, it is expected that the more massive stars should have younger H II regions. Though we see this trend for the first two bins, the next three bins certainly do not show larger ages. However these stars have much smaller ionizing radiation and can more quickly reach their Strömgren radii, r_s, where recombination equals photoionization. We have tabulated the range of r_s for each Q_0 bin assuming full ionization, $T_e = 10^4$ K, and hydrogen density $N_H = 20$ cm^{-3}. These assumed values can differ from region to region; thus, we may expect the range of r_s to be larger. It is evident that these lower-mass stars have values of $R_{\rm max}$ more comparable to r_s, which may make us unable to calculate the age of these

Table 4.4. Lifetime of a YSO's HII Region

log Q_0 Range	Sp. Type[a] Range	Num. of Sources	$R_{\rm median}$ (pc)	$R_{\rm max}$ (pc)	$t_{\rm median}/10^5$ (yr)	$t_{\rm max}/10^5$ (yr)	r_s Range (pc)
49–49.5	O3V–O7V	7	1.5	3.6	1.5	3.6	9.2–13.5
48.4–49	O7V–O8V	13	2.2	5.3	2.1	5.2	5.8–9.2
47.9–48.4	O8V–O9V	8	0.9	2.6	0.9	2.6	4.0–5.8
47.3–47.9	O9V–B0V	13	1.1	1.9	1.1	1.8	2.5–4.0
46.5–47.3	B0V–B0.5V	12	0.8	2.1	0.8	2.0	1.4–2.5

[a]Spectral types are from Smith et al. (2002) using $0.4Z_{\odot}$.

regions using the sound-crossing time. However, we have shown that higher mass stars are typically in denser environments, and N_H may be much higher than 20 cm^{-3}, indicating that even the most massive stars could be reaching their Strömgren radii.

4.4 Summary

We have conducted a survey of free-free emission around 102 spectroscopically confirmed massive YSOs and found H II regions around 54 of the sources. We compare *Spitzer* spectral features, including estimates from spectroscopic modeling, to measured quantities from the free-free emission. Our main results are summarized below.

- Almost all YSOs that have enough ionizing flux to produce a detectable H II regions indeed have an H II region. Moreover, masses estimated from Robitaille et al. (2007) models appear to be fairly accurate. Since mass correlates with most observed parameters, it is a crucial consideration when exploring correlations in almost any other relationship.

- The measured parameters (e.g., densities) of these regions are indicative of "dense" H II regions, though they may be harboring UC H II regions.

- More embedded (likely younger) sources are denser and less likely to be resolved, indicating evolving H II regions.

- We have found relationships between *Spitzer* spectra and continuum fluxes. Though a power-law is certainly not a perfect fit, an approximate free-free emission and mass relationship is $F_\nu \propto M^3$. There is a large spread in the data, and sources that lack emission lines in their spectra typically have lower fluxes, while some sources with emission lines have fluxes that are significantly higher than expected.

- H II regions about YSOs are likely better modeled as prolate spheroids. However, spherical geometry still provides reasonable estimates of the parameters of the region.
- The sources with the highest silicate PCA strength (and likely younger sources) tend to be unresolved and denser, indicating that these H II regions take time to evolve. We also see that massive sources are also less likely to be resolved. Since most sources with high PCA strength tend to be massive, mass may be a factor as much as age for the size of the H II region.
- More massive YSOs tend to be in denser environments, with a relationship of about $n_e \propto M^{2.3}$.
- We find the typical relationship between density and size of $n_e \propto D^{-1}$, though due to the spread of our data, we caution the relationship. The spread in the relationship is primarily due to sampling a large range of ionizing fluxes.
- YSO H II regions have ages $\geq 10^5$ yr, consistent with the extended regions of KK01. Since it is plausible that our H II contain more compact sources, our observations may be the extended subset of hierarchical structure in YSO H II regions.

Support for this work was provided by the NSF grant EAPSI 08-603 and AST 08-07323.

Figs. 4.11-4.40 – ATCA 5.5 GHz radio continuum contours on top of MOSAIC Hα images sorted by RA. Masked white pixels in the Hα images denote saturated pixels. All detected SL09 YSOs are shown with triangles along with non-detected YSOs that may be incident in the image. The associated field is also listed in each figure caption. Contour levels are [3,4,5,6,8,10,15,20,30,40,50,75,100,150,200,250,300,400,500, 600,700,800,900,1000] $\times\sigma$ where σ is the rms sensitivity value for each field from Table 4.1. Negative contours are not shown.

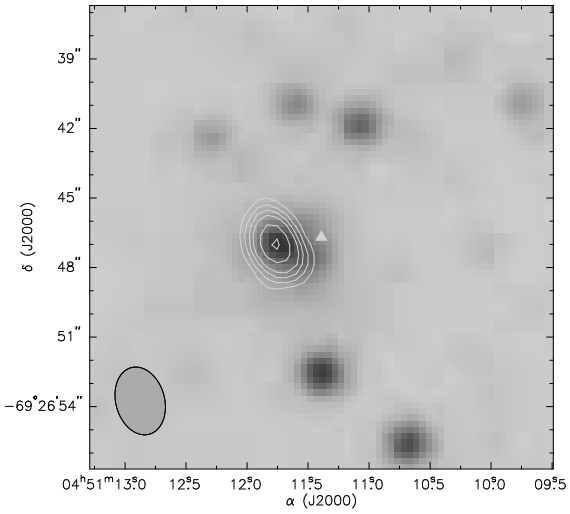

Figure 4.11 N79: 045111.39-692646.7.

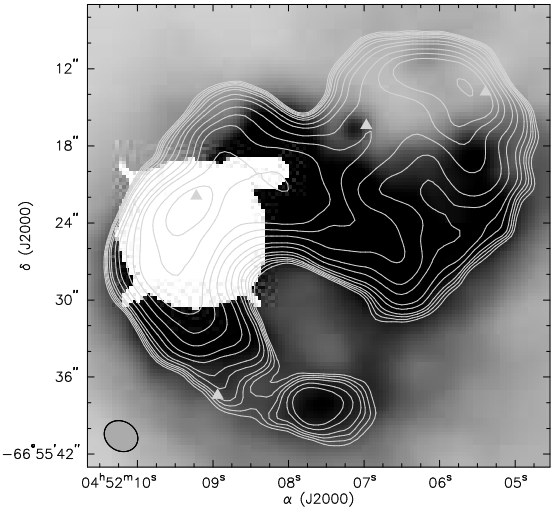

Figure 4.12 N4: from right to left, 045205.39-665513.8, 045206.97-665516.4, 045208.94-665537.4, and 045209.22-665521.9.

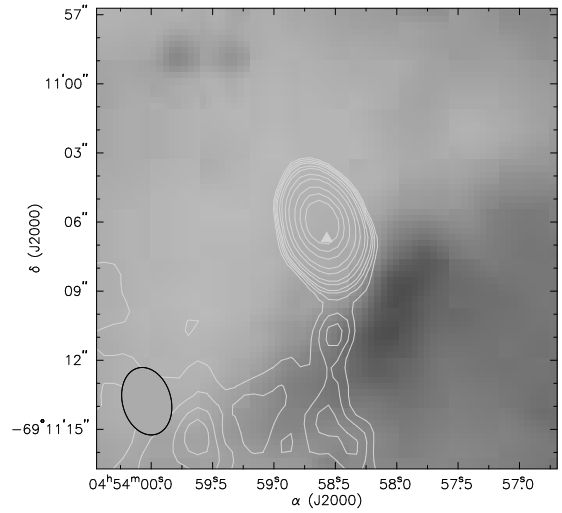

Figure 4.13 N83: 045358.57-691106.7.

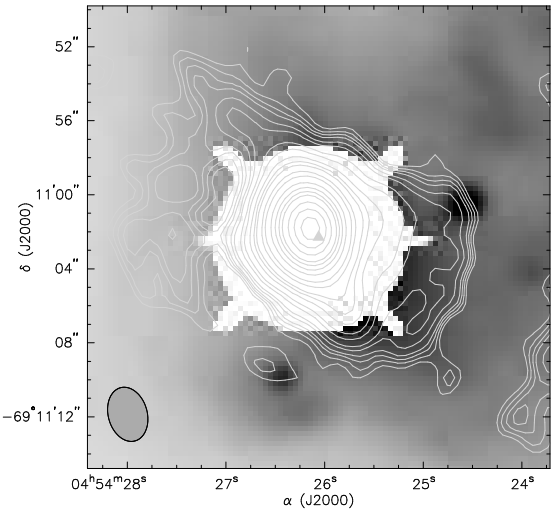

Figure 4.14 N83: 045426.06-691102.3.

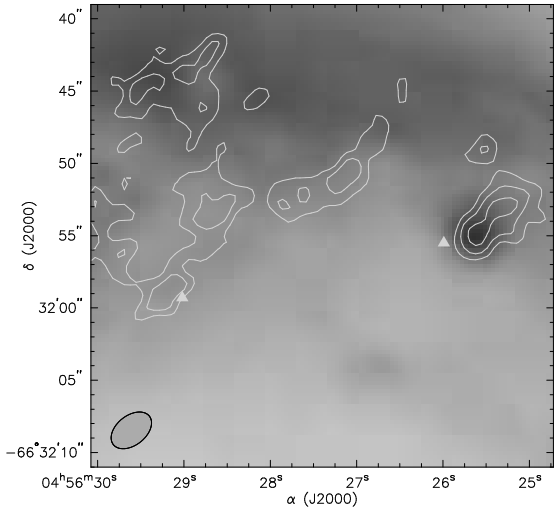

Figure 4.15 N11F: from right to left, 045625.99-663155.5 and 045629.02-663159.3.

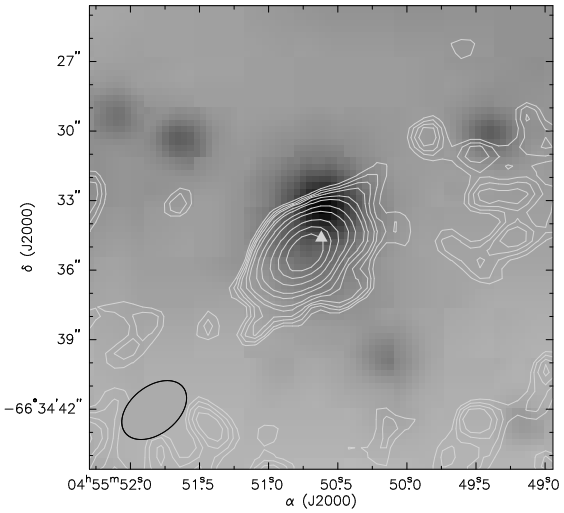

Figure 4.16 N11F: 045550.62-663434.6.

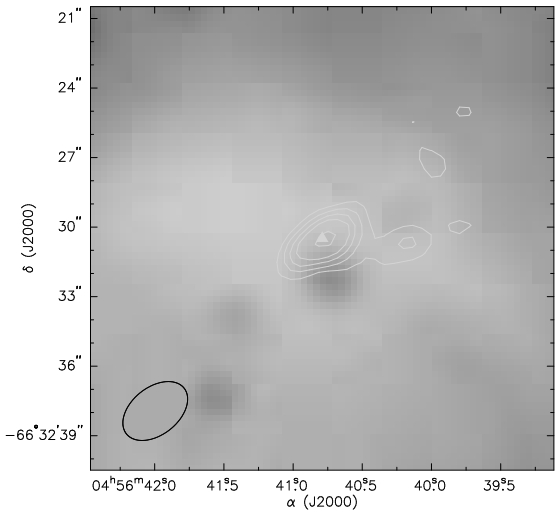

Figure 4.17 N11F: 045640.79-663230.5.

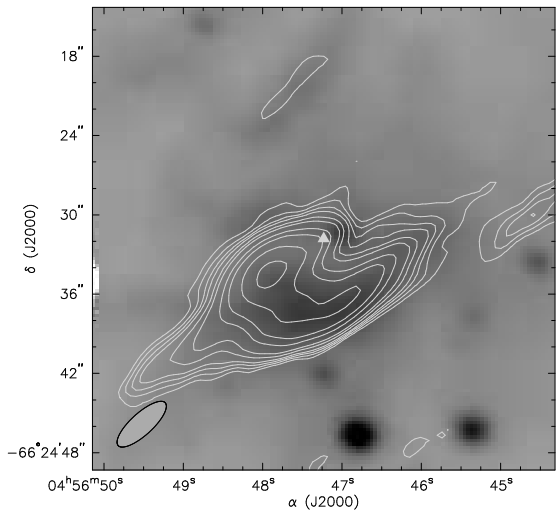

Figure 4.18 N11A/B: 045647.23-662431.8.

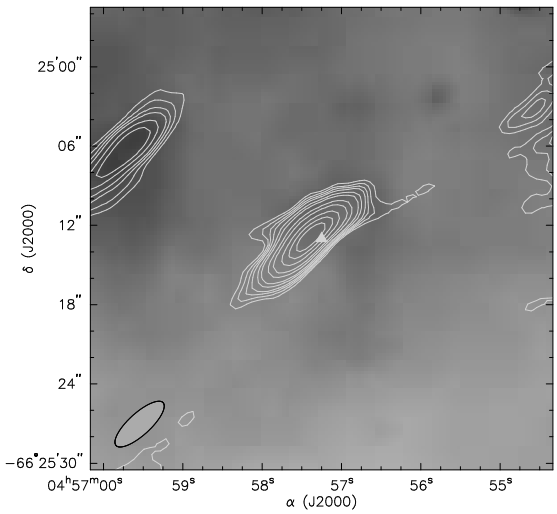

Figure 4.19 N11A/B: 045657.25-662513.0.

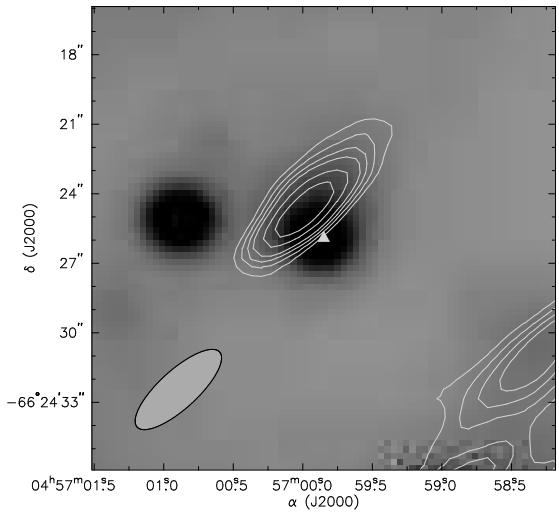

Figure 4.20 N11A/B: 045659.85-662425.9.

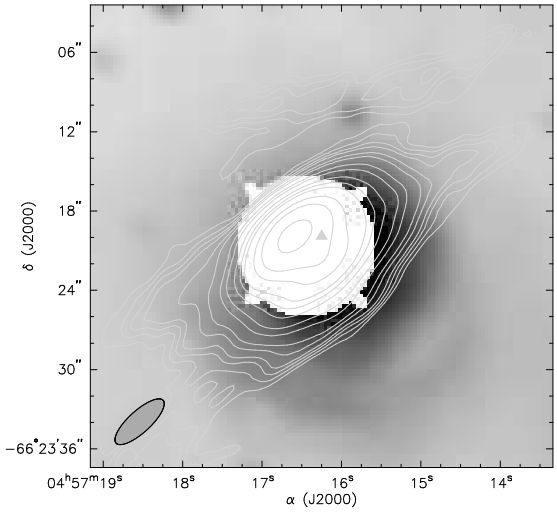

Figure 4.21 N11A/B: 045716.25-662319.9.

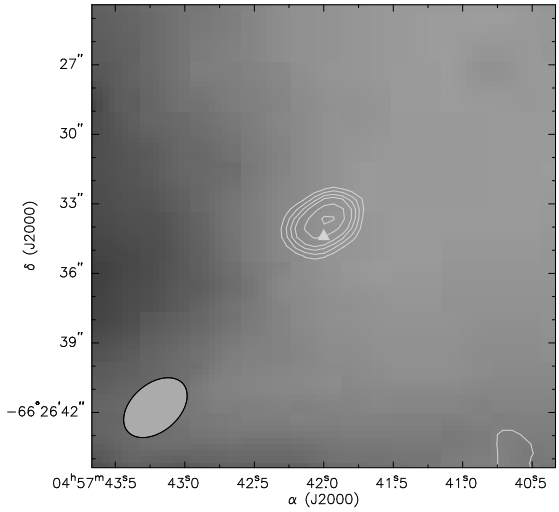

Figure 4.22 N11C/D: 045742.00-662634.4.

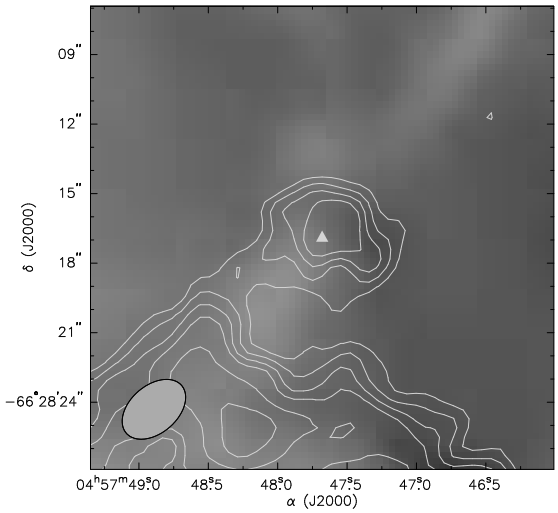

Figure 4.23 N11C/D: 045747.68-662816.9.

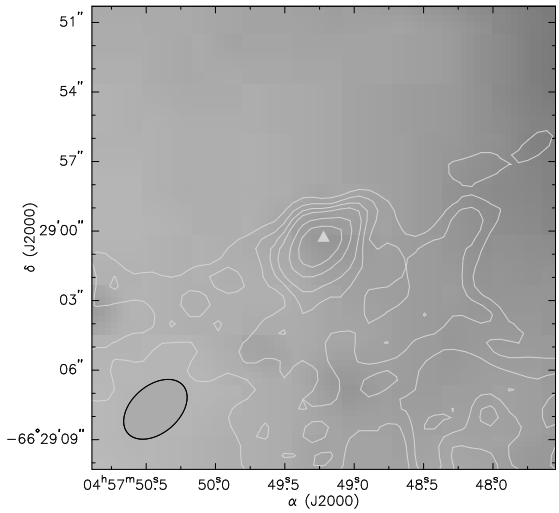

Figure 4.24 N11C/D: 045749.22-662900.3.

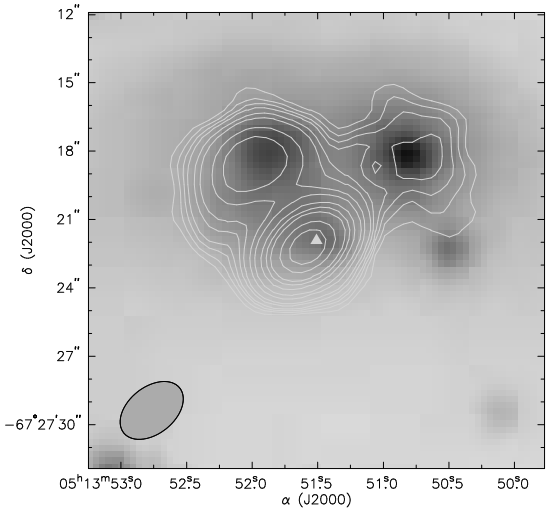

Figure 4.25 N30: 051351.51-672721.9.

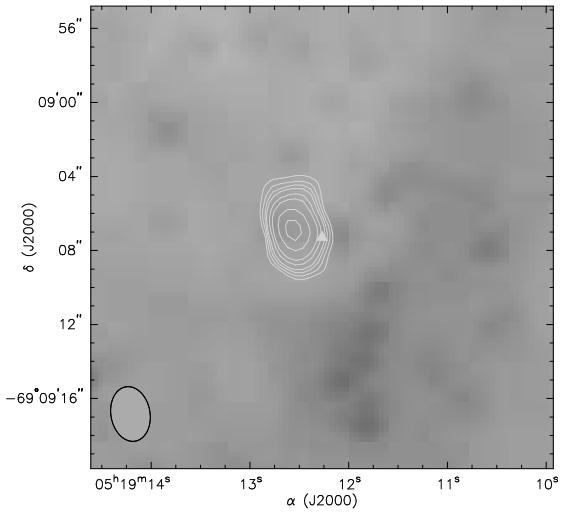

Figure 4.26 N119: 051912.27-690907.3.

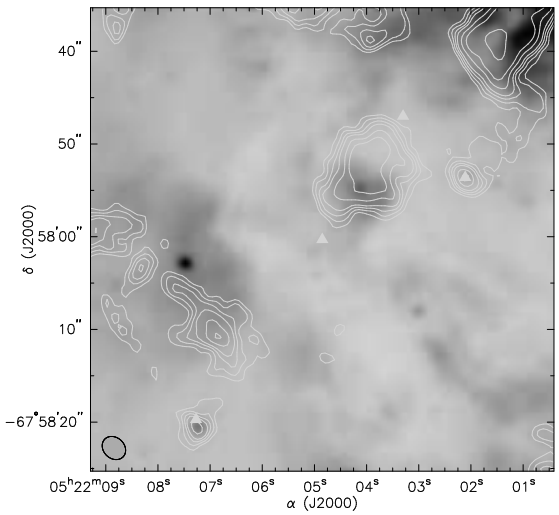

Figure 4.27 N44: from right to left, 052202.11-675753.6, 052203.30-675747.0, 052204.85-675800.3, and 052207.27-675819.7.

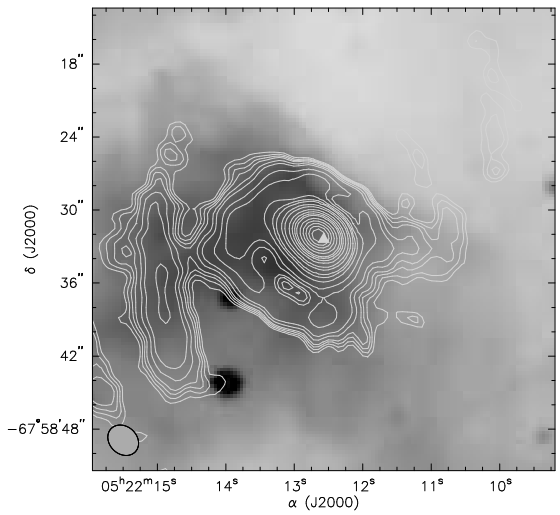

Figure 4.28 N44: 052212.57-675832.4.

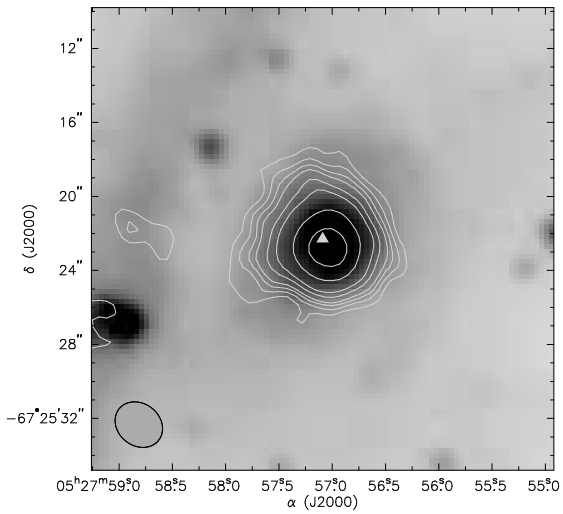

Figure 4.29 N51: 052757.09-672522.3.

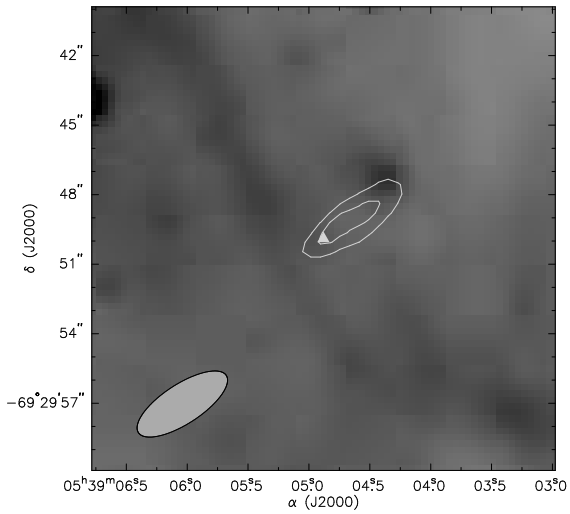

Figure 4.30 N158: 053904.88-692949.9.

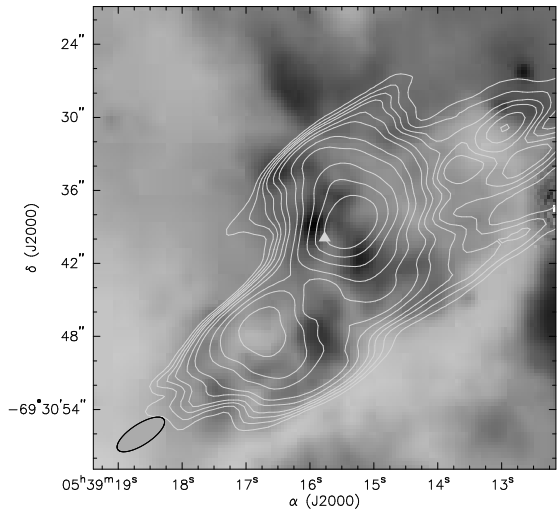

Figure 4.31 N158: 053915.77-693039.9.

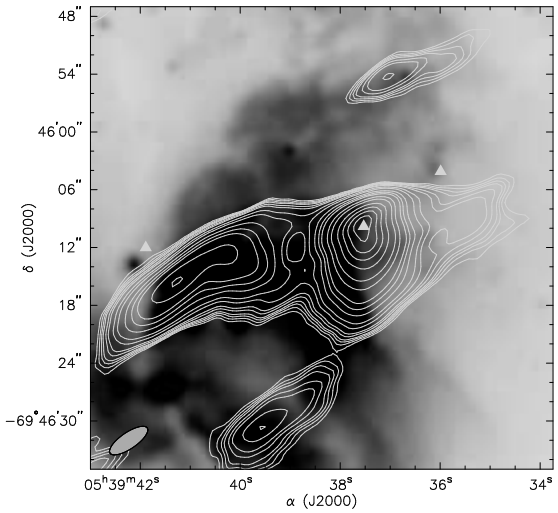

Figure 4.32 N158: 053937.53-694609.8.

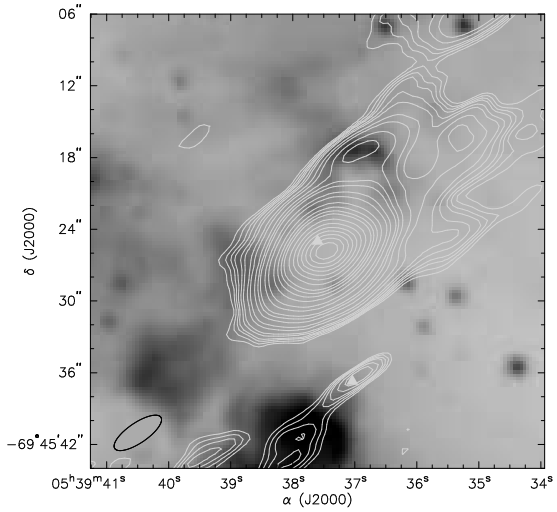

Figure 4.33 N159: from right to left, 053937.04-694536.7 and 053937.60-694525.0.

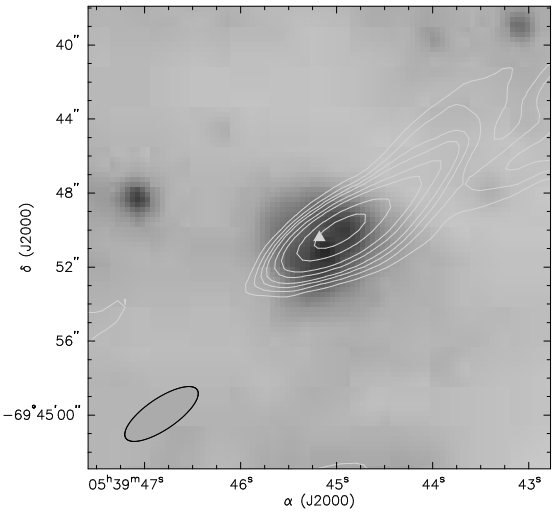

Figure 4.34 N159: 053945.18-694450.4.

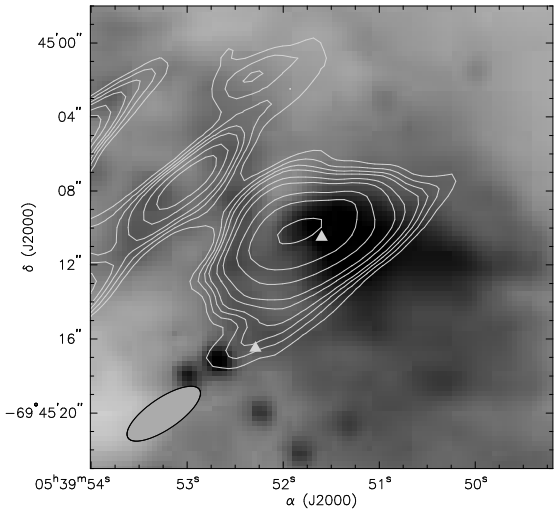

Figure 4.35 N159: from right to left, 053951.60-694510.5 and 053952.11-710930.7.

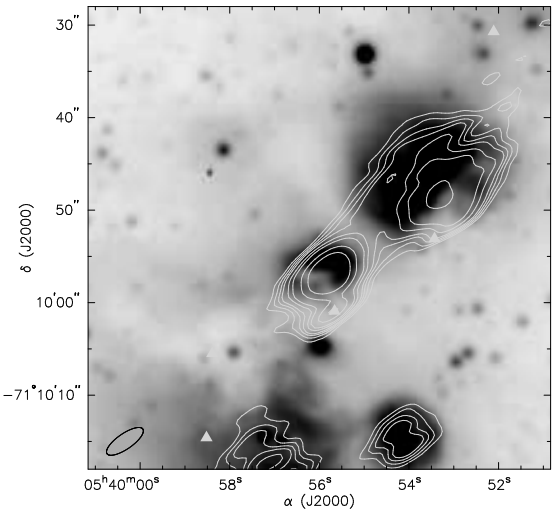

Figure 4.36 N214: from right to left, 053952.11-710930.7, 053953.43-710953.1, 053955.66-711000.9, 053958.39-711005.5, and 053958.52-711014.6.

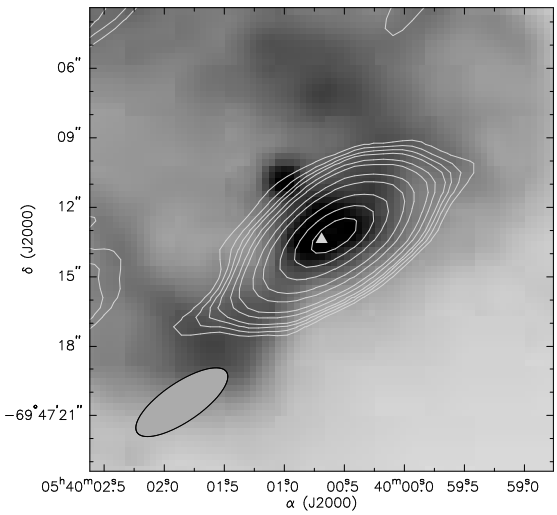

Figure 4.37 N159: 054000.69-694713.4.

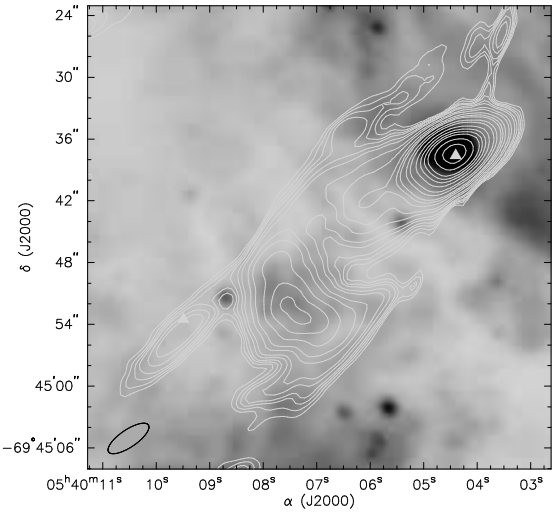

Figure 4.38 N159: from right to left, 054004.40-694437.6 and 054009.49-694453.5.

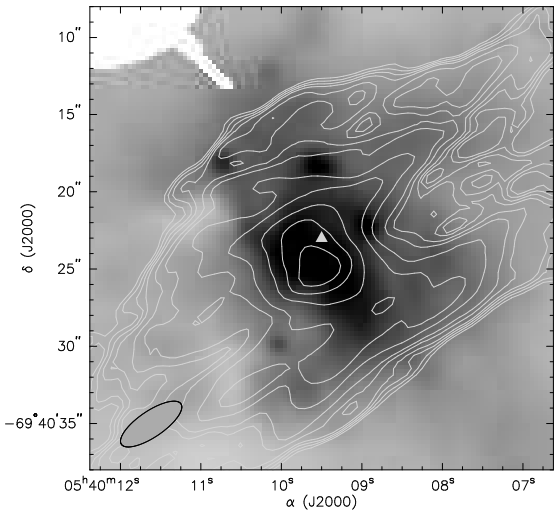

Figure 4.39 N159: 054009.50-694023.0.

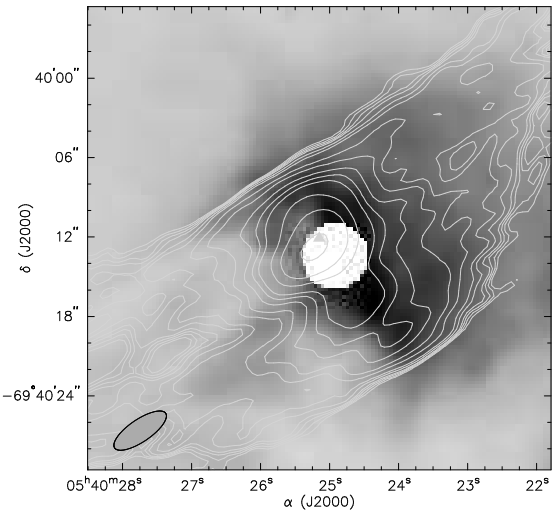

Figure 4.40 N159: 054025.15-694012.1.

Chapter 5

Spitzer Observations of Dust Emission from HII Regions in the Large Magellanic Cloud

5.1 Introduction

Far infrared (FIR) emission of interstellar dust has been commonly used to gauge star formation rates (e.g., Calzetti et al. 2010). In a star-forming region, interstellar dust can be heated, sputtered, and shattered by energy feedback from massive stars via ultraviolet (UV) radiation, fast stellar winds, and supernova remnant (SNR) shocks. It would thus be prudent to investigate how dust properties are modified in the harsh environment around massive stars.

The Large Magellanic Cloud (LMC) provides a nearby, ideal laboratory to study the influence of massive stars on dust properties because of the following advantages over our Galaxy: (1) the LMC has a nearly face-on orientation, mitigating the confusion and extinction along the Galactic plane; (2) the LMC is at a known distance, ∼50 kpc (Feast 1999), so stars can be resolved and studied in conjunction with the interstellar gas and dust; and (3) there exist many complementary multi-wavelength observations of stars, gas, and dust in the LMC. For these reasons, the LMC has been targeted by every space-based IR observatory to study dust properties and calibrate dust emission as star formation indicators.

The first report of *Spitzer Space Telescope* observations of an LMC H II complex was made by Gorjian et al. (2004) for LHA 120-N206 (N206 for short; designation from Henize 1956); its dust emission was qualitatively compared with that of the Orion Nebula. Subsequently, the entire LMC was surveyed by *Spitzer* in the Legacy program Surveying the Agents of a Galaxy's Evolution (SAGE; Meixner et al. 2006). Using the SAGE and additional data of 32 H II complexes in the LMC and SMC, Lawton et al. (2010) found that the 70 μm fluxes appear to be the best star formation indicator, although the correlation between the 70 μm flux and the bolometric IR flux in the 30 Dor giant H II region shows a high degree of scatter. The

This chapter includes material submitted for publication which includes the authors Ian W. Stephens, Jessica Marie Evans, Rui Xue, You-Hua Chu, Robert A. Gruendl, and Dominique M. Segura-Cox

anomaly in 30 Dor could be attributed to the intense energy feedback from the large number of massive stars encompassed by this region.

The SAGE data have also been used to analyze the global FIR emission in the LMC and spectral energy distributions (SEDs) of three large regions selected to represent different levels of star-formation activity (Bernard et al. 2008). A 70 μm excess in the SEDs is found, and this excess increases along the sequence "Milky Way – LMC – SMC", suggesting an influence of decreasing metallicity. The SEDs are fit with an improved version of the dust emission model by Désert et al. (1990), and it is suggested that the 70 μm excess can be explained by a modification of the size distribution of very small grains (VSGs). Since large VSGs are produced through erosion of large grains in the diffuse medium, the presence of VSGs suggests effects of energy feedback.

To investigate the effects of massive stars on dust emission, Slater et al. (2011) studied the dust properties of 4 classical and 12 superbubble H II regions in the LMC and found little correlation between dust emission properties and the spectral type of the hottest star, bolometric luminosity of the underlying massive stars, or the evolutionary status of the H II regions. This result is surprising and is at odds with the anomalous properties of 30 Dor and the abundant presence of large VSGs.

We have examined the H II region sample of Slater et al. (2011) and find that their division between classical and superbubble cases may not be consistent with observations. For example, DEM L34 (= N11; DEM designation from Davies et al. 1976) and DEM L152 (= N44) both contain multiple OB associations with a central superbubble surrounded by compact H II regions, but are classified as "classical" and "superbubble" H II regions, respectively. Furthermore, they have used the integrated dust emission from entire H II regions, while it is expected that the influence of stellar energy feedback ought to depend on radial distances from the stars.

To investigate the influence of massive stars on interstellar dust grains with the least ambiguity, we have chosen to study two clearly defined classical H II regions, N63 (= DEM L243) and N180 (= DEM L323), and two relatively simple superbubbles, N70 (= DEM L301) and N144 (= DEM L199), whose stellar content is well studied. We have analyzed *Spitzer* observations of these four regions, measuring flux densities in radially distributed subregions, constructing SEDs, and using dust emission model fits to determine the dust properties. In this paper, we describe our methodology, target selection, and data sets used in Section 5.2, discuss the stellar content and assess the stellar energy feedback in Section 5.3, describe the creation and modeling of SEDs in Section 5.4, examine the results of each H II region in Section 5.5, discuss the relationship between stellar energy feedback and dust properties in Section 5.6, and summarize the findings in Section 5.7.

5.2 Overview of Methodology, Targets, and Observations

Our strategy for studying the effects of stellar energy feedback on dust grains was to (1) select clean-cut classical and superbubble H II regions around OB associations with well-studied stellar content, (2) use the known stellar content to estimate the radiation field, (3) use archival *Spitzer* observations to extract SEDs for a series of subregions sampling different radial distances to the ionizing OB association, (4) use dust emission models to fit the SEDs and assess the dust properties with respect to the stellar radiation field, and (5) examine the evolutionary status and dust properties of the H II regions and search for variations of dust properties that may be caused by stellar feedback.

Below we describe the four H II regions selected for this study and the data sets used in the analysis. The methods of analysis are described in detail in later sections.

5.2.1 H II Regions Selected for Analysis

We have selected two pairs of H II regions to study their spatially resolved dust properties. The first pair consists of young H II regions, in which massive stars have not cleared a large central cavity via fast stellar winds and supernova explosions. The Hα surface brightness peaks near the central OB association. Such H II regions are often referred to as "classical" H II regions. For this type we have chosen N63 and N180, also known as DEM L243 and DEM L323, respectively.

N63 encompasses the OB association LH 83 (Lucke & Hodge 1970). The stellar content of LH 83 has been studied both spectroscopically and photometrically by Oey (1996). As seen in Figure 5.1, the H II region appears amorphous with a few bright patches. The most massive star in this region has exploded and produced the SNR N63A (Mathewson et al. 1983; Chu 1997; Warren et al. 2003), marked by the X-ray contour over the [S II] image in Figure 5.1. N63 is also classified as a classical H II region by Slater et al. (2011).

N180 is photoionized by the OB association LH 117. The massive star content of LH 117 has been reported by Massey et al. (1989). Figure 5.1 shows a bright compact H II region with some filamentary structure along its periphery. The internal kinematics of this H II region show local expansion around some massive stars, but no large-scale expansion or SNR shocks have been detected (Nazé et al. 2001). Both this paper and Slater et al. (2011) classify N180 as a classical H II region; however, we exclude the faint southeast extension that is photoionized by the OB association LH 118 because the lack of dense gas near the ionizing stars implies a more evolved state.

The second pair consists of superbubbles, in which OB associations have cleared a central cavity and

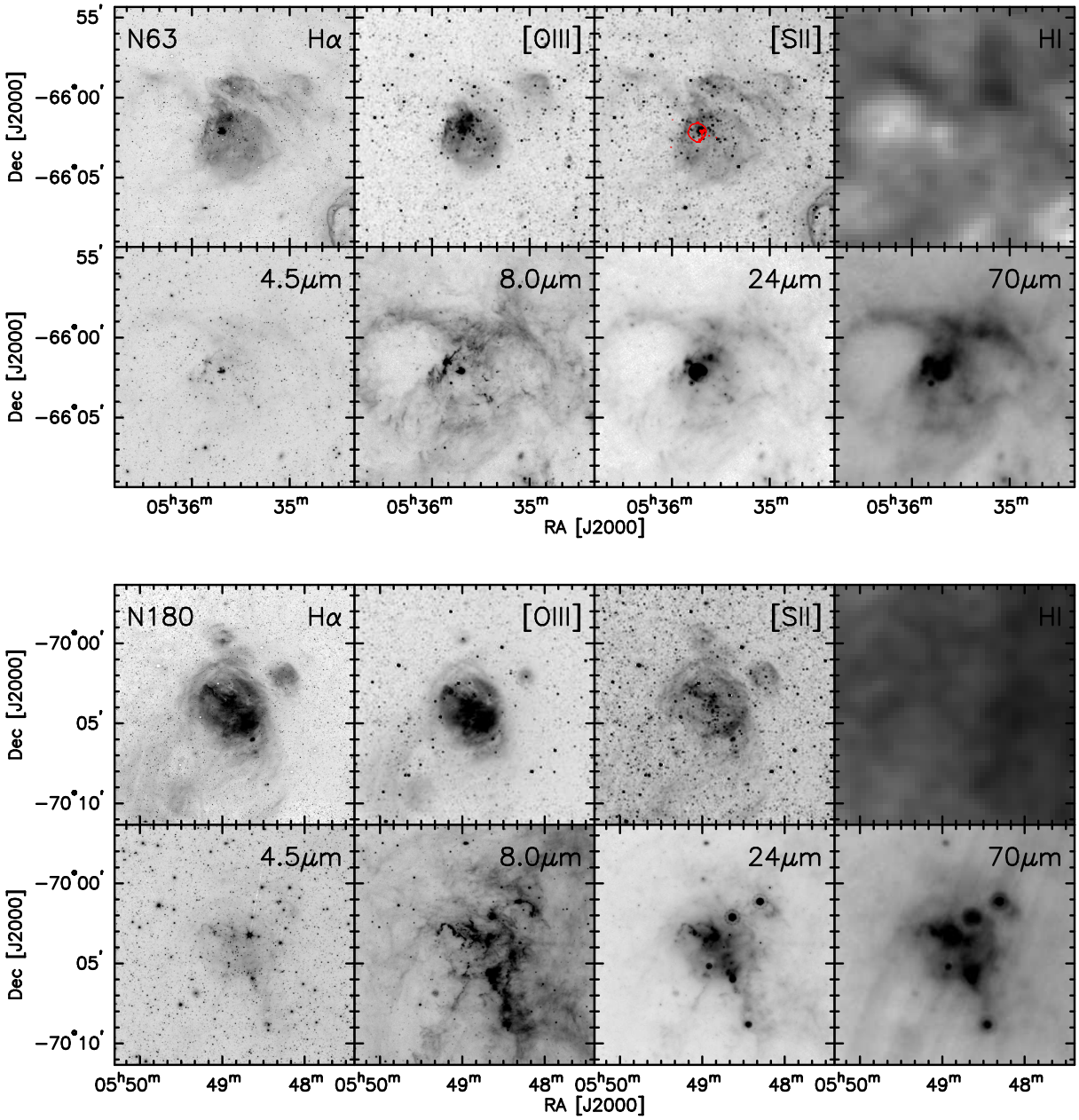

Figure 5.1 Multi-wavelength imaging for classical H II regions N63 and N180. Red contours on [S II] indicate locations of X-ray emission.

swept the interstellar gas into a shell structure. We have selected two superbubbles, N70 and N144, also known as DEM L301 and DEM L199, respectively.

N70 is a superbubble around the OB association LH 114. The massive stars in LH 114 have been studied by Oey (1996). This superbubble has essentially thermal radio emission (Dopita et al. 1981) but shows detectable diffuse X-ray emission, indicating interactions with a recent supernova explosion (Chu & Mac Low 1990). Slater et al. (2011) also classify N70 as a superbubble.

N144 is a superbubble blown by the OB association LH 58. The massive stars of LH 58 have been studied in detail by Garmany et al. (1994). We have classified N144 as a superbubble, in contrast to the classical H II region classification by Slater et al. (2011), because N144 shows a limb-brightened morphology and an expanding shell structure in high-dispersion, long-slit echelle spectra in the Hα line. No SNRs have been reported in N144. Massive young stellar objects have been found in N144 (Gruendl & Chu 2009), indicating on-going star formation.

The emission from stars, gas, and dust in these four H II regions can be seen in the multi-wavelength images presented in Figure 5.1 (two classical H II regions) and Figure 5.2 (two superbubbles).

5.2.2 Observations and Data Sets

Multi-wavelength data sets were used in this work. First, we used optical emission-line images of the H II regions to examine the spatial distribution and spectral variations of the ionized gas and to diagnose the ionization fronts and interstellar shocks. We then used the observed stellar content of these regions to estimate the interstellar radiation field; where available, we adopted spectroscopically determined stellar types reported in the literature, and for the rest we assessed their types and masses using optical photometric data. Finally, we used archival *Spitzer* observations to extract the SEDs of the dust emission for further modeling and analysis. These data sets are described below.

Nebular Emission-Line Images

Hα, [O III] λ5007, and [S II] $\lambda\lambda$6716, 6731 images of these H II regions are available from the Magellanic Cloud Emission-Line Survey (MCELS; Smith & MCELS Team 1999). These images are neither continuum-subtracted nor flux-calibrated; thus, only variations in the surface brightness profiles or line ratios can be determined quantitatively. A rough Hα flux calibration can be made by comparisons with the integrated Hα fluxes reported by Kennicutt & Hodge (1986). The angular resolution of the MCELS images is 2-3$''$.

We have obtained higher-resolution Hα images of our target H II regions using the MOSAIC2 camera

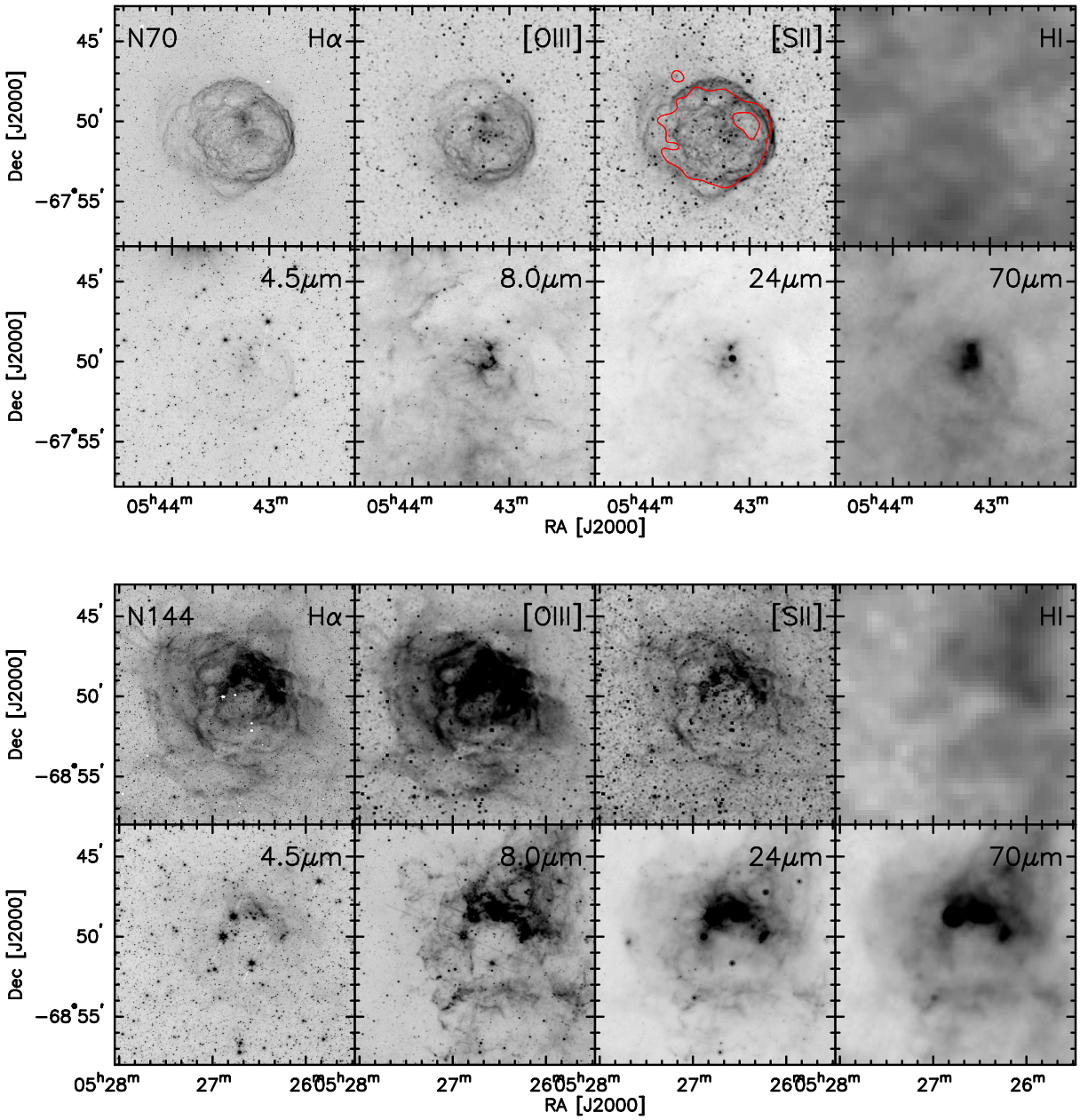

Figure 5.2 Multi-wavelength imaging for supperbubble regions N70 and N144. Red contours on [S II] indicate locations of X-ray emission.

on the Blanco 4m telescope at the Cerro Tololo Inter-American Observatory. The images were bias and flat-field corrected. Astrometric solutions were obtained through comparisons with the Two Micron All Sky Survey Point Source Catalog, typically resulting in better than $\sim 0\farcs2$ accuracy. The Hα images presented in Figures 5.1 and 5.2 have $\sim 1''$ resolution and are combinations of at least 3×300 s exposures. These MOSAIC Hα images are also not continuum-subtracted or flux-calibrated, but they are useful in showing positions of ionizing stars, dust lanes, and small-scale structure of the ionized gas.

Spectroscopic Classifications of Massive Stars

The most massive stars are also the most luminous stars and thus dominate the radiation field of an OB association. Since hot massive stars emit mostly in the far-ultraviolet, the effective temperature and luminosity of a massive star cannot be determined reliably from optical photometry; spectroscopic classifications are needed (Massey 1993). All four H II regions selected for this work have their stellar content well studied both photometrically and spectroscopically. For the most massive stars, we relied on the spectroscopic classifications published in the literature: Oey (1996) classified 17 OB stars in N63 and 20 OB stars and 4 late-type supergiants in N70, Garmany et al. (1994) listed new and published spectral types for the 47 bluest and brightest stars (all OB stars) in N144, and Massey et al. (1989) provided new and published spectral types for the 29 bluest stars (all OB stars) in N180. The spectral types and luminosity classes of OB stars from these studies were used to determine their masses and contributions to the radiation field. The late-type supergiants are as luminous as main-sequence B0 stars and were thus included in the calculation of radiation fields.

Magellanic Cloud Photometric Survey

For main-sequence stars later than late-O, the spectral types can be assessed from optical photometry; therefore, we used the Magellanic Cloud Photometric Survey catalog for stars in the LMC (Zaritsky et al. 2004). This catalog was also used to identify stars in areas around the H II regions which are not covered by previous spectroscopic studies but whose massive stars may make significant contributions to the radiation field. MCPS provides astrometry and $UBVI$ photometry of stars and is reasonably complete for sources with $V \lesssim 20$ mag. Each MCPS entry comes with a set of flags that indicate the quality of the individual detections, including how well the source compares to the point spread function (PSF) and whether the measurements were replaced by photometry in the literature.

We have excluded catalog entries that do not have a complete set of photometric measurements in the $UBVI$ bands, whose magnitude errors in any band exceed 0.2 mag, and whose stars are excluded from PSF

fitting or are not well fit by the PSF. Furthermore, we excluded detections whose $(B-V) \geq 0$ to maintain a sample of blue stars which are expected to be the main source of radiation and for which extinction-free color-magnitude diagrams (CMDs) can be constructed for further analysis (see Section 5.3.1).

After unqualified objects were removed from the MCPS sample, there remained: 429, 501, 2679, and 685 blue stars for the regions within $\sim$ 125, 150, 180, and 170 pc of the central subregions of N63, N70, N144, and N180, respectively. Among these, 13 stars from N63, 14 from N70, 23 from N144, and 16 from N180 had spectroscopic observations from previous studies, and the spectral classifications were used for their mass and luminosity estimates.

The MCPS photometry in the central region of N180 appeared uncharacteristically erroneous upon initial inspection. The MCPS observations were made using a drift-scan camera, which was unable to resolve densely distributed stars against a bright nebular background (Zaritsky et al. 2004). For this reason, in the high surface brightness central region of N180, we opted for the photometric results from Massey et al. (1989), replacing with spectral types from the same study when possible. The way in which the MCPS stars, and those taken from previous studies, were used to determine the radiation field will be described in Section 5.3.1.

Spitzer Space Telescope Observations

The *Spitzer* SAGE observations of the LMC used the Infrared Array Camera (IRAC) and the Multiband Imaging Photometer (MIPS) instruments. The IRAC images have four bands centered at 3.6, 4.5, 5.8, and 8 μm, and the MIPS images have three bands centered at 24, 70, and 160 μm. The detailed survey strategy and data processing of the SAGE observations can be found in Meixner et al. (2006). For all four IRAC bands, we sampled available $1\overset{\circ}{.}1 \times 1\overset{\circ}{.}1$ tiles of our H II regions from the most recent SAGE data release, DR3 (2009). For MIPS, we sampled data from DR3 or DR2 (2008) depending on the availability of specific data. For example, a complete mosaic for MIPS 160 μm was available in DR2, but not DR3. In addition, the available 24 μm mosaic of the LMC from DR3 was prohibitively large due to its higher resolution, but $1\overset{\circ}{.}1 \times 1\overset{\circ}{.}1$ tiles are not released in DR3; thus the small 24 μm files from DR2 were used. Image size was not an issue for the 70 μm mosaic, so the DR3 mosaic was used.

5.3 Stellar Content and Radiation Field

To investigate the effects massive stars have on the dust in these H II regions, we must quantify the stellar

radiation field. We accomplish this by (1) estimating luminosities from their spectral types, when available, or through comparisons of their locations with stellar evolutionary tracks in CMDs, then (2) determining their bolometric incidence flux on designated subregions.

5.3.1 Photometric Estimation of Stellar Masses and Luminosities

To estimate the masses and luminosities of stars without spectroscopic classifications, we used the photometric measurements from MCPS and Massey et al. (1989) and compared them against stellar evolutionary tracks from Lejeune & Schaerer (2001) for initial masses between 5 and 120 $M_{\odot}$. Along these evolutionary tracks, the effective mass, luminosity, temperature, and predicted $UBVRI$ photometry are tabulated for time steps of $\Delta \log t = 0.05$ dex starting at 10^3 yr. We adopted the evolutionary tracks for a metallicity $Z = 0.4\ Z_{\odot}$, which is close to the LMC metallicity.

The extinction to individual stars is unknown, but the stars of interest are blue; therefore, we opted to use the Wesenheit extinction-free magnitude $W \equiv V - DM - (B-V)A_V/E(B-V)$ (Madore 1982) and the Johnson Q reddening-free color $Q \equiv (U-B) - (B-V)E(U-B)/E(B-V)$ (Johnson & Morgan 1953), where $DM = 18.5$ is the distance modulus of the LMC, $E(U-B)/E(B-V) = 0.72$ for blue stars, and $A_V/E(B-V) = 3.1$ from the canonical extinction law.

We assigned masses and luminosities to our candidates by plotting their extinction-free parameters (W and Q) in a color-magnitude diagram (CMD) alongside the evolutionary tracks. As with the MCPS data, the evolutionary tracks were expressed in extinction-free parameters for direct comparison. The evolutionary tracks represent stars of masses 7, 10, 12, 15, 20, 25, 40, 60, 85, and 120 $M_{\odot}$. The closest evolutionary track to a star gives an estimate for its mass, and its position along the track determines its luminosity. Our final analysis includes stars with estimated masses $\gtrsim 7\ M_{\odot}$. The exclusion of lower mass stars is justified because for an unevolved population with the Salpeter (1955) initial mass function, only ~10% of the total radiation is contributed by stars $< 10\ \mathrm{M}_{\odot}$.

A sample CMD can be found in Figure 5.3, which shows evolutionary tracks and stars in N63. With approximated luminosities for the massive star candidates, the radiation field could be quantified. For both N63 and N70, the highest mass stars as ascertained by the evolutionary tracks (and have no spectroscopic classification) were 25 $M_{\odot}$. N144 and N180, on the other hand, included several stars at 40 and 60 $M_{\odot}$ that were not observed in spectroscopic surveys. The masses of these stars are uncertain, but this should not affect the calculation of the radiation field incident on our subregions (described in the next section) by more than a factor of 2.

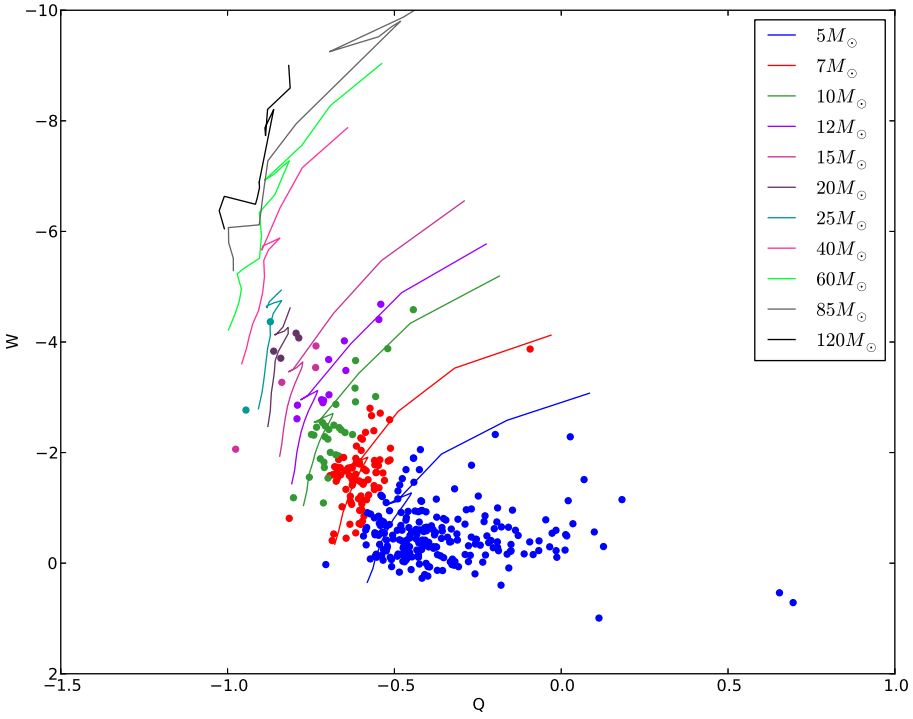

Figure 5.3 Color-magnitude diagram of classical H II region N63 with evolutionary tracks from Lejeune & Schaerer (2001). The color of each star matches the color of the closest evolutionary track, and this mass was used during the construction of the radiation field.

5.3.2 Radiation Field

Based on the fitted evolutionary tracks, 136, 124, 807, and 328[1] massive stars ($M_\odot \gtrsim 7$) exist across the H II regions N63, N70, N144, and N180, respectively. The luminosities of these stars from the evolutionary tracks were used in the estimation of the radiation field. For stars whose spectral types are known from previous studies, their masses and luminosities were estimated directly from their spectral types (Johnson 1966; de Jager & Nieuwenhuijzen 1987; Cox 2000; Smith et al. 2002) and were used in the radiation field calculation.

The line-of-sight locations of the stars are unknown, so it is impossible to compute the 3-dimentional radiation field. As an approximation, we produced a 2-dimensional radiation field image by adding the fluxes of all the stars about each H II region using an inverse square law with effective distance $d_{\rm eff} = \sqrt{2}d_{\rm proj}$, where $d_{\rm proj}$ is the projected distance to a star. These images are shown in the rightmost panels of Figures 5.4a-5.7a. The radiation flux for various parts of each H II can be measured to approximate the total incident power on each subregion (described in Section 5.4) for comparison with exhibited dust properties. The calculated interstellar radiation field (ISRF) presented for each subregion is the median ISRF, which

[1] 61 of these stars in N180 are from Massey et al. (1989)

allows direct comparison to the methodology discussed in Section 5.4.

5.4 Constructing and Modeling of Spectral Energy Distributions of Dust Emission

5.4.1 Construction of SEDs and Color-Color Diagrams

In order to investigate how spectral properties of dust emission vary radially throughout each H II region, we (1) defined radial subregions based on ionized features in Hα images, (2) filtered out contamination due to individual stars in the IRAC bands, (3) calculated background-subtracted fluxes in each subregion, (4) established SEDs for each subregion for further modeling, and (5) constructed color-color diagrams (CCDs) for comparisons among the subregions.

For each H II region (N63, N180, N70, and N144), we used MOSAIC Hα images to examine the distribution of ionized gas in the region. We then placed circular apertures (subregions) with a 40″-diameter (10 pc at the distance of the LMC) in a pattern bisecting the stellar content to sample the dust emission radially for each H II region. In N63, N70, and N144 we used a cross pattern (evenly spaced in each of the four cardinal directions), and for N180 we used a single cut from the northeast to the southwest in order to avoid the diffuse H II region around the OB association LH118 to the southeast. For each H II region, the subregions extend beyond the bright Hα emission. To estimate the local background emission from the LMC, we placed an additional subregion well outside the ionized region at a location with low flux in all the *Spitzer* bands and devoid of massive stars as identified in Section 5.3.1. The locations of the subregions are marked in the top panel of Figures 5.4-5.7.

To reduce the contributions of bright stars to the IR emission, we used a box median filter with size 4.″2×4.″2 (7×7 pixels) to remove point sources from images in the IRAC bands. In the median-filtered images, several of the brightest remaining objects can be identified as extended background galaxies. As a test, SEDs were computed for subregions using both median-filtered and unaltered images for N63. The uncertainty estimates (the method of calculating these are discussed below) indeed show ∼25% improvement when the contamination by individual stars has been median-filtered out. The MIPS images were not median-filtered, as stellar emission is negligible compared to dust emission at these long wavelengths.

The flux density of each subregion was calculated by measuring the median flux value of the pixels within each subregion (using the median-filtered IRAC images and unaltered MIPS images) and multiplying by the

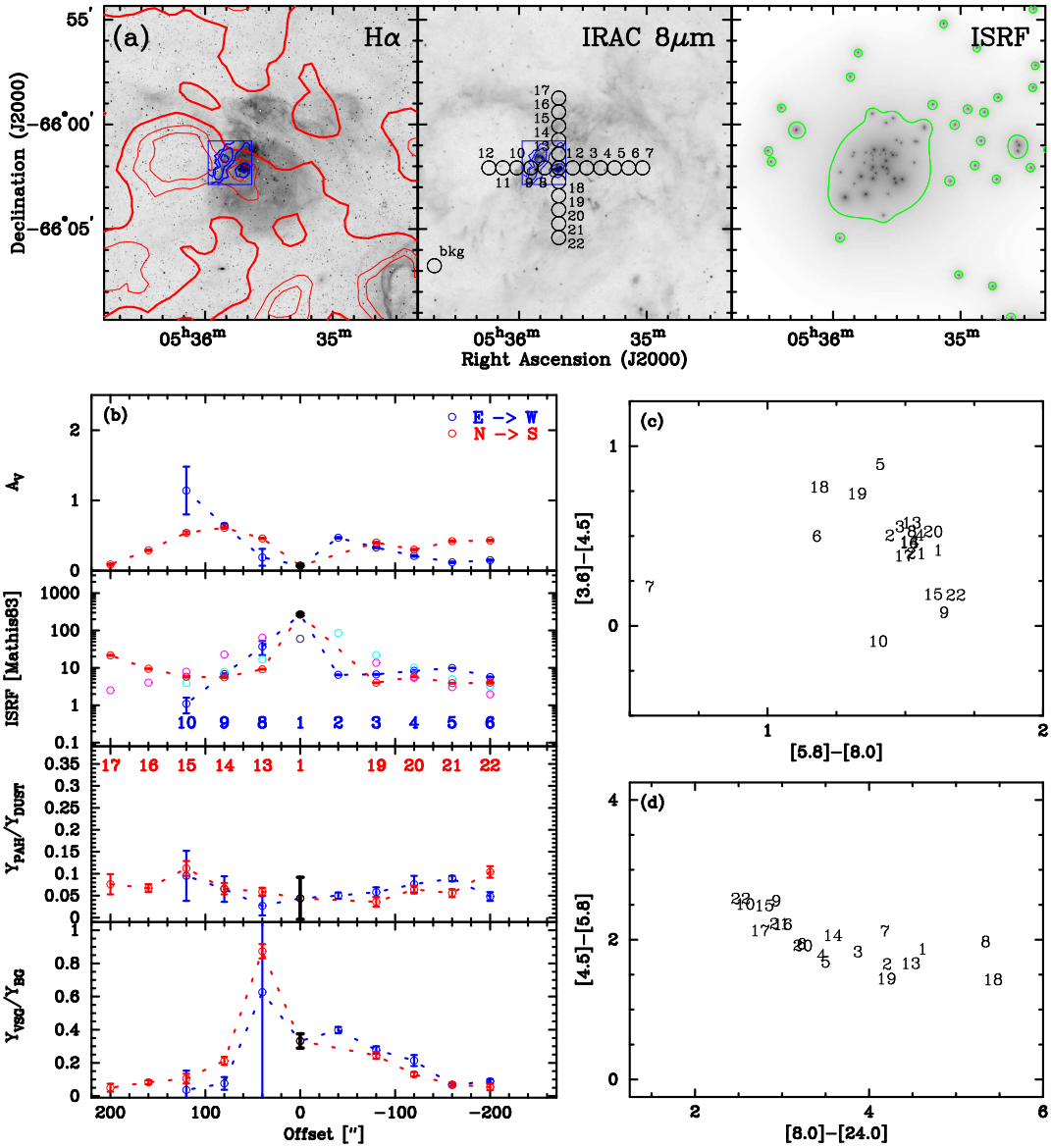

Figure 5.4 Observations and results of classical H II region N63. (a) Hα, IRAC 8 μm, and the radiation field due to massive ($\gtrsim 7M_{\odot}$) stars. North is up. Red contours show ATCA+Parkes HI integrated intensity contours. Blue contours are ESO-SEST CO(2-1) integrated intensity at 22″ resolution. Green contours on the rightmost panel indicate a fiducial value for the radiation field due to massive stars. Numbered circles show 40″ subregions sampled with the background subregion labeled as bkg. (b) `DustEM` model fits. The x-axis shows the offset from the central subregion. The variations of the physical quantities from top panel to bottom panel are: visual extinction, InterStellar Radiation Field, PAH mass fraction to dust mass fraction, and VSG mass fraction to BG mass fraction. The magenta and cyan colors on the ISRF panel show the ISRF as derived from stars. Error bars are 1σ. (c) [5.8]-[8.0] vs [3.6]-[4.5] and (d) [5.8]-[8.0] vs [3.6]-[4.5] color-color diagrams.

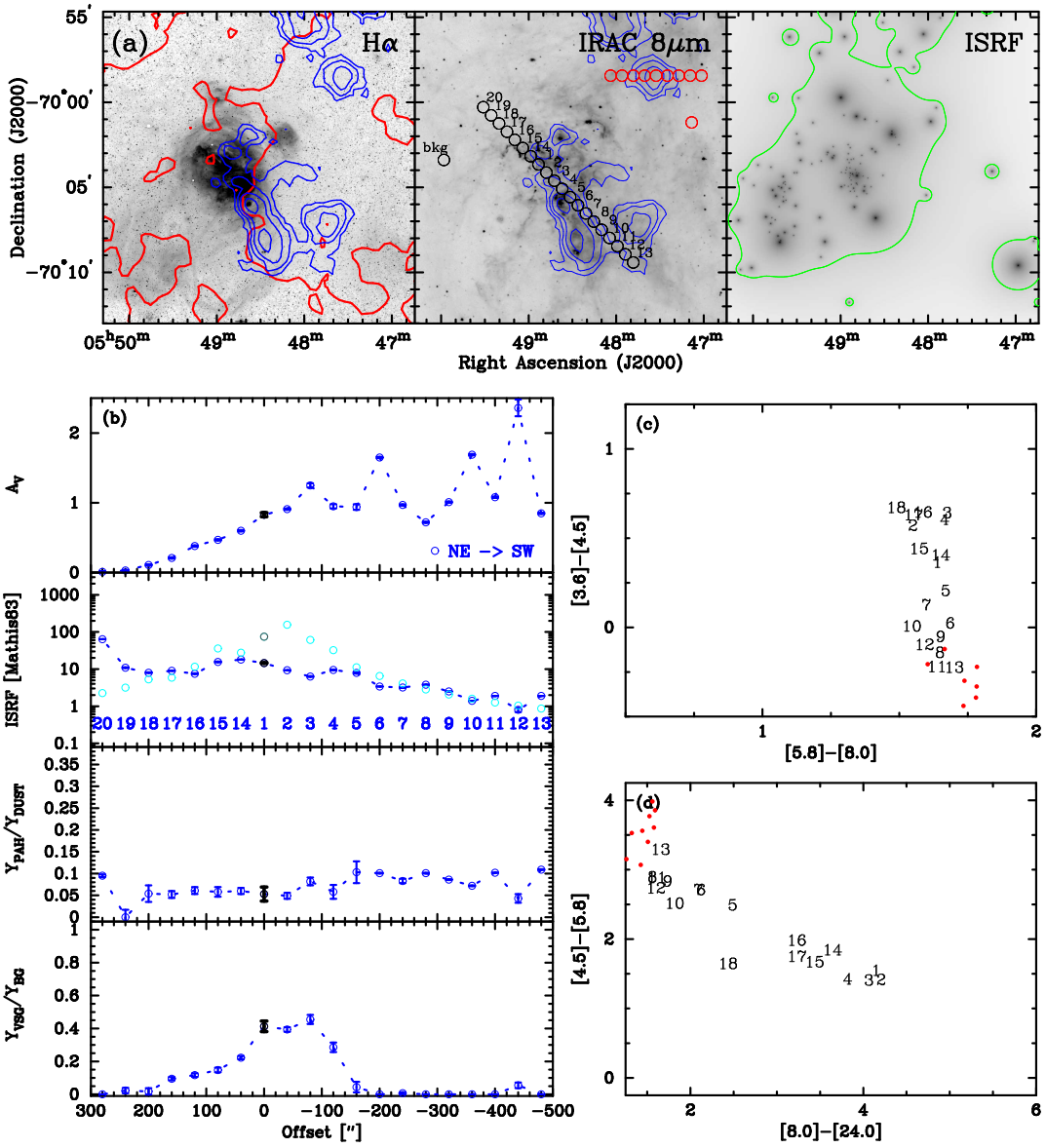

Figure 5.5 Observations and results of classical H II region N180. Description of plots are the same as Figure 5.5 with the exception of the blue contours showing large scale CO(1-0) emission from MAGMA (Wong et al. 2011). The IRAC 8 μm image shows red circles at locations (along with a background subregion) where we test the prevalence of PAHs in molecular clouds in the CCD (also shown in red).

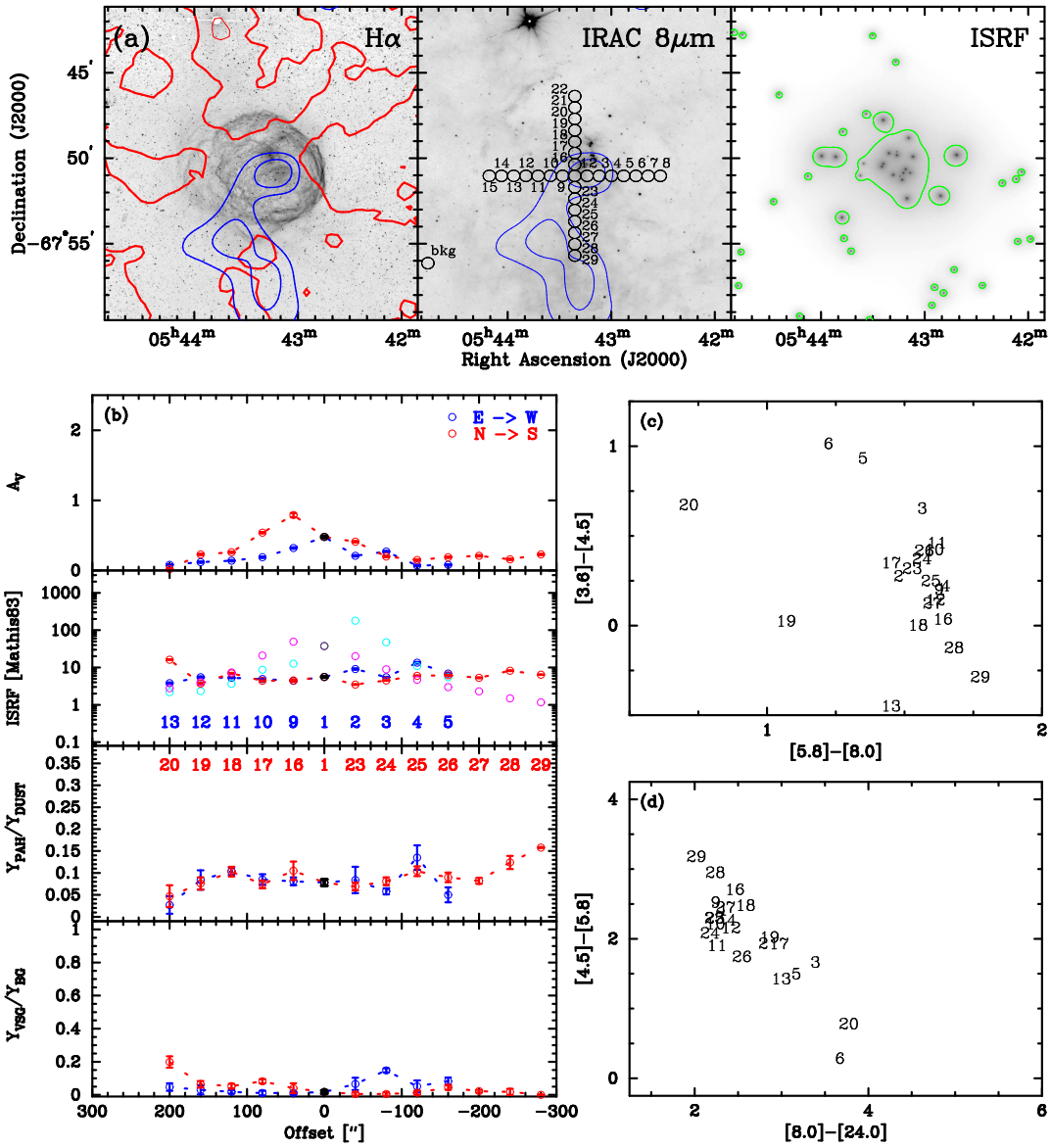

Figure 5.6 Observations and results of the superbubble N70. Description of plots are the same as Figure 5.4 with the exception of the blue contours showing large scale CO(1-0) emission from NANTEN (Fukui et al. 2008).

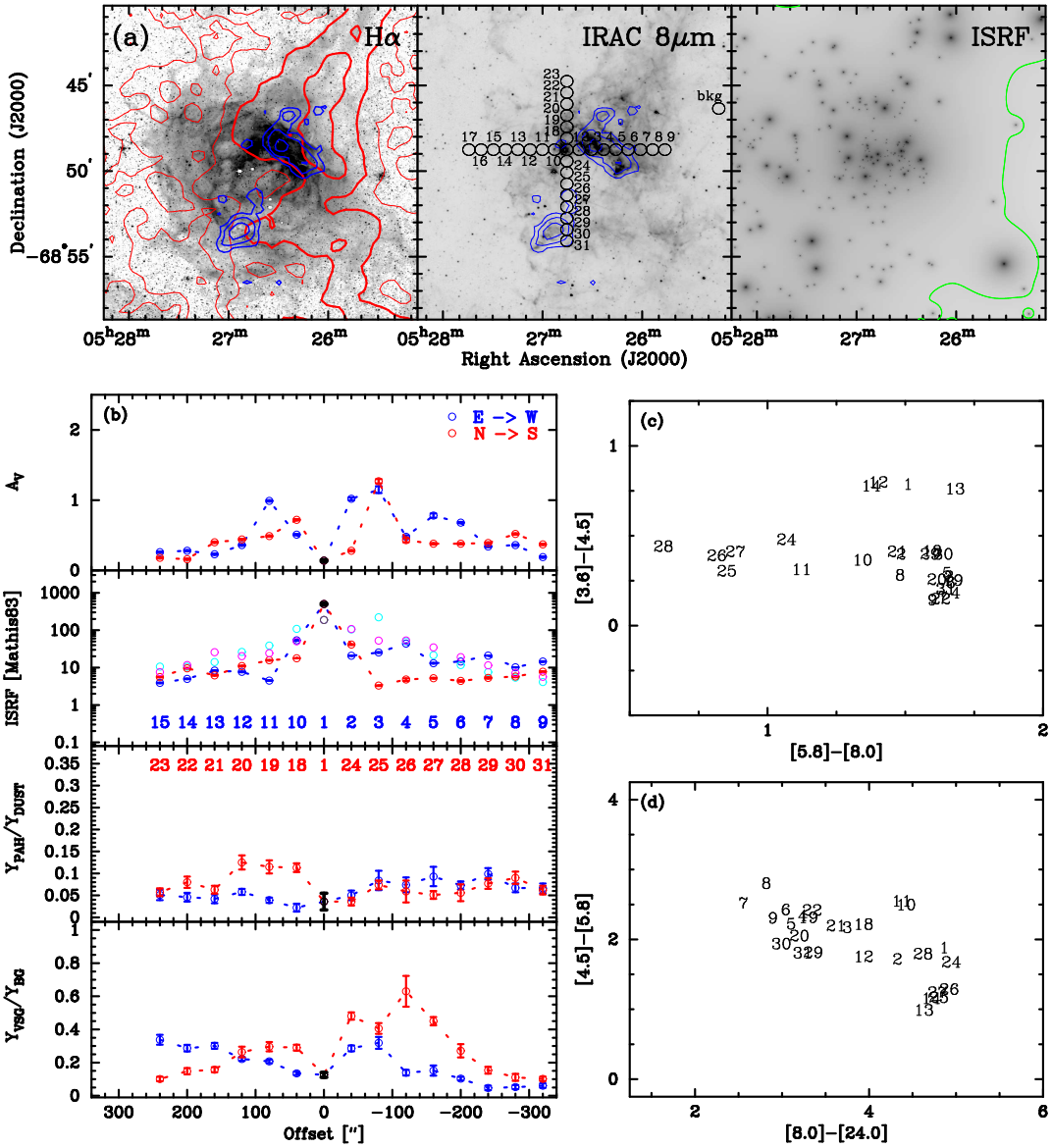

Figure 5.7 Observations and results of the supperbubble N144. Description of plots are the same as Figure 5.4 with the exception of the blue contours showing large scale CO(1-0) emission from MAGMA.

total pixel count. A background subregion's flux density was then subtracted from each subregion's flux density to determine the local emission. The median was chosen rather than the mean because large ranges of fluxes with non-Gaussian distributions were often present. To assess the approximate uncertainty of each measurement, we used the first and third quartile of the flux distribution within the subregion as estimates for the lower and upper uncertainty estimates, respectively. Since the resolution and data-sampling of *Spitzer* is wavelength-dependent, the number of pixels which formed each flux measurement varies with band. A subregion in each of the four IRAC bands contained 3409 pixels, while the MIPS 24, 70, and 160 μm bands had 197, 49, and 5 pixels, respectively. Therefore, the quartile error-bars show the spread of subregional fluxes for all bands except MIPS 160 μm (however the 160 μm error bars do not grossly affect SED fitting). The flux densities from the seven *Spitzer* mid-IR bands were then combined to form an SED for each subregion. The photometric flux density measurements of each subregion for all four H II regions are shown in Table 5.1.

Table 5.1. Photometric Flux Density Measurements[a]

HII Region	Subregion	3.6μm (mJy)	4.5μm (mJy)	5.8μm (mJy)	8.0μm (mJy)	24μm (mJy)	70μm (mJy)	160μm (mJy)
N63	1	$13.4^{+31.1}_{-7.9}$	$12.9^{+29.4}_{-7.2}$	$48.1^{+145.6}_{-27.0}$	$119.1^{+316.3}_{-75.6}$	$933^{+46.7}_{-23.6}$	$8513^{+104.9}_{-55.7}$	$3186^{+0.6}_{-0.9}$
	2	$3.4^{+1.2}_{-0.6}$	$3.5^{+0.9}_{-0.5}$	$10.7^{+2.4}_{-1.7}$	$22.5^{+4.7}_{-3.7}$	$121^{+1.4}_{-1.5}$	$1372^{+5.5}_{-4.8}$	$1956^{+0.1}_{-0.1}$
	3	$2.2^{+0.6}_{-0.5}$	$2.3^{+0.3}_{-0.3}$	$8.4^{+2.9}_{-1.5}$	$18.3^{+7.5}_{-4.1}$	$72^{+0.5}_{-0.3}$	$920^{+1.1}_{-0.8}$	$1397^{+0.1}_{-0.1}$
	4	$2.3^{+0.8}_{-0.6}$	$2.4^{+0.5}_{-0.4}$	$8.2^{+3.8}_{-1.8}$	$19.1^{+9.8}_{-5.9}$	$51^{+0.6}_{-0.4}$	$702^{+0.6}_{-1.1}$	$1014^{+0.0}_{-0.0}$
	5	$0.8^{+0.3}_{-0.2}$	$1.2^{+0.2}_{-0.2}$	$3.7^{+1.1}_{-1.1}$	$7.5^{+1.4}_{-1.3}$	$21^{+0.2}_{-0.1}$	$426^{+0.6}_{-0.2}$	$635^{+0.0}_{-0.0}$
	6	$0.9^{+0.7}_{-0.5}$	$0.9^{+0.4}_{-0.4}$	$3.7^{+1.5}_{-1.0}$	$6.1^{+1.6}_{-1.4}$	$13^{+0.1}_{-0.1}$	$283^{+0.3}_{-0.3}$	$564^{+0.1}_{-0.0}$
	7	$0.4^{+0.3}_{-0.3}$	$0.3^{+0.3}_{-0.2}$	$1.7^{+0.9}_{-0.7}$	$1.6^{+2.5}_{-1.4}$	$8^{+0.2}_{-0.1}$	$322^{+1.1}_{-1.0}$	$740^{+0.1}_{-0.2}$
	8	$3.2^{+0.7}_{-0.6}$	$3.4^{+0.6}_{-0.5}$	$13.9^{+3.5}_{-2.4}$	$31.5^{+7.2}_{-5.5}$	$481^{+2.7}_{-2.5}$	$2704^{+9.2}_{-6.4}$	$3040^{+0.6}_{-0.6}$
	9	$3.4^{+5.2}_{-1.5}$	$2.4^{+4.2}_{-1.0}$	$16.7^{+21.0}_{-5.9}$	$42.2^{+53.3}_{-15.3}$	$70^{+3.9}_{-1.8}$	$1481^{+10.8}_{-9.7}$	$2718^{+0.2}_{-0.4}$
	10	$2.0^{+3.4}_{-1.6}$	$1.2^{+1.6}_{-1.0}$	$8.1^{+16.8}_{-5.1}$	$16.5^{+47.5}_{-13.5}$	$19^{+1.2}_{-0.7}$	$182^{+2.0}_{-1.4}$	$1171^{+0.5}_{-0.6}$
	11	$0.3^{+0.5}_{-0.2}$	$0.4^{+0.4}_{-0.3}$	$1.0^{+1.0}_{-0.9}$	$-0.6^{+1.3}_{-1.0}$	$2^{+0.1}_{-0.1}$	$-15^{+0.4}_{-0.2}$	$197^{+0.1}_{-0.1}$
	12	$-0.0^{+0.3}_{-0.2}$	$0.0^{+0.3}_{-0.3}$	$-0.1^{+1.0}_{-0.9}$	$-2.6^{+0.7}_{-0.6}$	$0^{+0.1}_{-0.0}$	$-60^{+0.3}_{-0.3}$	$3^{+0.0}_{-0.0}$
	13	$4.7^{+1.1}_{-0.8}$	$5.3^{+1.2}_{-0.7}$	$16.2^{+3.5}_{-2.5}$	$36.7^{+8.5}_{-6.8}$	$253^{+3.0}_{-2.1}$	$2301^{+1.2}_{-6.6}$	$2505^{+0.1}_{-0.1}$
	14	$3.2^{+1.2}_{-1.0}$	$3.2^{+0.9}_{-0.7}$	$14.3^{+4.9}_{-3.2}$	$32.2^{+12.1}_{-7.9}$	$97^{+1.2}_{-0.8}$	$1286^{+2.1}_{-1.1}$	$2245^{+0.1}_{-0.1}$
	15	$4.3^{+1.6}_{-1.2}$	$3.3^{+0.9}_{-0.8}$	$21.7^{+6.3}_{-4.9}$	$53.0^{+18.2}_{-11.1}$	$77^{+0.6}_{-0.6}$	$1045^{+1.2}_{-1.3}$	$2016^{+0.1}_{-0.4}$
	16	$2.3^{+0.6}_{-0.5}$	$2.3^{+0.6}_{-0.4}$	$11.8^{+2.5}_{-2.2}$	$26.6^{+7.3}_{-3.9}$	$47^{+0.5}_{-0.4}$	$1035^{+1.0}_{-1.1}$	$1550^{+0.0}_{-0.3}$
	17	$2.2^{+1.1}_{-0.9}$	$2.1^{+1.1}_{-0.9}$	$9.8^{+3.9}_{-3.3}$	$21.6^{+10.6}_{-9.1}$	$30^{+1.0}_{-0.6}$	$849^{+2.5}_{-2.9}$	$828^{+0.0}_{-0.0}$
	18	$1.4^{+0.7}_{-0.4}$	$1.9^{+0.7}_{-0.4}$	$4.8^{+1.7}_{-1.7}$	$7.9^{+2.5}_{-2.5}$	$130^{+5.9}_{-2.4}$	$1442^{+13.8}_{-8.3}$	$1401^{+0.4}_{-0.2}$
	19	$1.4^{+0.4}_{-0.3}$	$1.7^{+0.4}_{-0.3}$	$4.4^{+1.8}_{-1.5}$	$8.3^{+4.6}_{-2.5}$	$44^{+0.3}_{-0.4}$	$572^{+0.6}_{-0.2}$	$1141^{+0.0}_{-0.0}$
	20	$1.7^{+0.4}_{-0.4}$	$1.7^{+0.4}_{-0.4}$	$6.8^{+1.3}_{-1.6}$	$16.6^{+3.4}_{-2.7}$	$36^{+0.1}_{-0.2}$	$596^{+0.9}_{-0.7}$	$1116^{+0.1}_{-0.0}$
	21	$1.2^{+0.4}_{-0.3}$	$1.1^{+0.3}_{-0.2}$	$5.8^{+1.6}_{-1.3}$	$13.4^{+3.9}_{-2.1}$	$23^{+0.1}_{-0.1}$	$448^{+0.2}_{-0.2}$	$1171^{+0.0}_{-0.1}$
	22	$1.9^{+0.4}_{-0.4}$	$1.5^{+0.3}_{-0.3}$	$10.7^{+2.0}_{-2.6}$	$28.1^{+5.2}_{-6.3}$	$32^{+0.2}_{-0.3}$	$471^{+0.7}_{-0.6}$	$1229^{+0.1}_{-0.0}$
N180	1	$15.2^{+5.4}_{-3.9}$	$13.9^{+3.2}_{-2.1}$	$38.6^{+20.3}_{-9.9}$	$97.3^{+51.9}_{-31.1}$	$495^{+6.6}_{-3.4}$	$6103^{+25.7}_{-17.8}$	$6340^{+0.1}_{-0.9}$
	2	$9.7^{+2.1}_{-1.3}$	$10.7^{+1.6}_{-1.1}$	$26.3^{+4.8}_{-4.4}$	$61.2^{+11.9}_{-10.2}$	$329^{+2.4}_{-1.5}$	$3952^{+7.8}_{-6.0}$	$4919^{+1.2}_{-0.4}$
	3	$10.2^{+1.5}_{-1.4}$	$12.1^{+1.1}_{-0.9}$	$29.5^{+7.9}_{-5.4}$	$76.8^{+19.9}_{-16.4}$	$362^{+2.0}_{-1.4}$	$3569^{+2.5}_{-5.0}$	$4994^{+0.1}_{-0.7}$
	4	$10.8^{+2.2}_{-1.7}$	$12.3^{+1.6}_{-1.0}$	$30.5^{+20.5}_{-6.0}$	$78.9^{+55.8}_{-17.8}$	$297^{+1.8}_{-2.4}$	$3962^{+7.0}_{-7.8}$	$5154^{+0.7}_{-0.2}$
	5	$8.6^{+4.4}_{-3.0}$	$6.8^{+3.2}_{-1.6}$	$45.0^{+21.3}_{-13.8}$	$116.8^{+55.3}_{-39.3}$	$129^{+3.1}_{-2.0}$	$2504^{+14.1}_{-8.5}$	$4364^{+0.1}_{-0.0}$
	6	$6.1^{+2.3}_{-1.9}$	$4.1^{+1.2}_{-1.1}$	$33.1^{+9.2}_{-10.8}$	$87.3^{+24.4}_{-27.9}$	$69^{+0.7}_{-1.2}$	$1299^{+3.1}_{-4.3}$	$4271^{+0.2}_{-1.1}$
	7	$3.0^{+0.8}_{-0.6}$	$2.2^{+0.5}_{-0.4}$	$17.9^{+1.6}_{-1.3}$	$43.6^{+4.3}_{-3.2}$	$33^{+0.1}_{-0.1}$	$717^{+0.4}_{-0.5}$	$2418^{+0.2}_{-0.0}$
	8	$5.0^{+1.3}_{-1.2}$	$2.9^{+0.8}_{-0.7}$	$27.5^{+5.7}_{-6.2}$	$69.9^{+17.6}_{-17.2}$	$32^{+0.3}_{-0.4}$	$642^{+1.1}_{-1.5}$	$1984^{+0.3}_{-0.1}$
	9	$3.2^{+1.2}_{-0.7}$	$2.0^{+0.7}_{-0.5}$	$18.1^{+3.0}_{-2.5}$	$46.3^{+5.6}_{-5.7}$	$25^{+0.1}_{-0.2}$	$484^{+0.4}_{-0.4}$	$2037^{+0.1}_{-0.2}$
	10	$3.3^{+2.2}_{-1.0}$	$2.2^{+1.5}_{-0.7}$	$14.8^{+2.5}_{-2.4}$	$34.2^{+6.5}_{-5.8}$	$20^{+0.2}_{-0.2}$	$327^{+0.6}_{-0.3}$	$2182^{+0.0}_{-0.3}$
	11	$4.0^{+1.2}_{-0.8}$	$2.1^{+0.8}_{-0.5}$	$20.2^{+4.0}_{-2.9}$	$50.9^{+9.7}_{-7.7}$	$25^{+0.1}_{-0.1}$	$324^{+0.4}_{-0.4}$	$1750^{+0.1}_{-0.0}$
	12	$3.6^{+1.8}_{-1.0}$	$2.1^{+1.1}_{-0.7}$	$17.6^{+2.0}_{-2.3}$	$42.6^{+3.9}_{-4.2}$	$20^{+0.1}_{-0.1}$	$243^{+0.4}_{-0.4}$	$1794^{+0.0}_{-0.9}$
	13	$2.1^{+0.8}_{-0.4}$	$1.1^{+0.5}_{-0.3}$	$15.6^{+1.8}_{-1.5}$	$41.8^{+3.5}_{-2.3}$	$21^{+0.2}_{-0.1}$	$241^{+0.4}_{-0.7}$	$1377^{+0.0}_{-0.0}$
	14	$11.2^{+2.6}_{-2.0}$	$10.6^{+2.0}_{-1.6}$	$38.6^{+8.3}_{-4.5}$	$98.5^{+21.2}_{-10.0}$	$315^{+4.6}_{-2.8}$	$5091^{+11.1}_{-4.5}$	$5127^{+0.4}_{-0.4}$
	15	$8.6^{+4.9}_{-1.9}$	$8.4^{+2.6}_{-1.4}$	$26.1^{+9.5}_{-5.0}$	$61.9^{+22.8}_{-10.9}$	$163^{+1.9}_{-1.5}$	$3201^{+9.0}_{-5.5}$	$3542^{+1.3}_{-0.8}$
	16	$2.2^{+0.8}_{-0.5}$	$2.6^{+0.6}_{-0.5}$	$10.7^{+2.0}_{-2.2}$	$25.6^{+3.8}_{-5.4}$	$56^{+0.8}_{-0.6}$	$1043^{+5.1}_{-3.6}$	$1732^{+0.2}_{-0.5}$
	17	$1.6^{+0.6}_{-0.4}$	$1.8^{+0.4}_{-0.3}$	$6.1^{+1.4}_{-1.1}$	$14.2^{+4.0}_{-2.6}$	$31^{+0.1}_{-0.2}$	$702^{+0.4}_{-0.8}$	$1078^{+0.1}_{-0.1}$

Table 5.1 (cont'd)

HII Region	Subregion	3.6μm (mJy)	4.5μm (mJy)	5.8μm (mJy)	8.0μm (mJy)	24μm (mJy)	70μm (mJy)	160μm (mJy)
	18	$0.9^{+0.8}_{-0.4}$	$1.1^{+0.5}_{-0.4}$	$3.3^{+1.9}_{-1.4}$	$7.2^{+2.9}_{-3.6}$	$7^{+0.1}_{-0.2}$	$294^{+1.6}_{-0.2}$	$528^{+0.3}_{-0.3}$
	19	$0.2^{+0.5}_{-0.3}$	$0.3^{+0.4}_{-0.3}$	$0.8^{+0.8}_{-0.9}$	$0.5^{+1.4}_{-1.4}$	$1^{+0.1}_{-0.1}$	$118^{+0.6}_{-0.5}$	$175^{+0.0}_{-0.0}$
	20	$-0.1^{+0.3}_{-0.3}$	$0.0^{+0.3}_{-0.3}$	$1.9^{+0.8}_{-1.1}$	$3.8^{+1.6}_{-1.9}$	$3^{+0.1}_{-0.1}$	$99^{+0.1}_{-0.2}$	$55^{+0.2}_{-0.0}$
N70	1	$2.6^{+0.9}_{-0.4}$	$2.0^{+0.6}_{-0.3}$	$12.4^{+2.9}_{-1.3}$	$31.1^{+7.4}_{-2.5}$	$29^{+0.7}_{-0.3}$	$766^{+1.9}_{-1.6}$	$1744^{+0.1}_{-0.4}$
	2	$3.2^{+1.6}_{-1.1}$	$2.7^{+0.9}_{-0.6}$	$10.5^{+7.0}_{-3.8}$	$22.9^{+18.8}_{-8.5}$	$33^{+0.2}_{-0.3}$	$696^{+1.7}_{-1.4}$	$1088^{+0.3}_{-0.1}$
	3	$1.5^{+0.6}_{-0.3}$	$1.8^{+0.4}_{-0.5}$	$5.5^{+1.0}_{-0.9}$	$13.0^{+1.8}_{-2.2}$	$33^{+1.2}_{-0.5}$	$519^{+1.4}_{-1.2}$	$983^{+0.1}_{-0.2}$
	4	$1.8^{+1.2}_{-0.5}$	$1.5^{+0.6}_{-0.4}$	$8.0^{+4.1}_{-1.6}$	$20.4^{+9.6}_{-4.1}$	$21^{+0.4}_{-0.1}$	$365^{+0.8}_{-1.1}$	$464^{+0.2}_{-0.0}$
	5	$0.5^{+0.5}_{-0.3}$	$0.8^{+0.4}_{-0.3}$	$2.1^{+1.0}_{-0.7}$	$4.1^{+2.5}_{-1.4}$	$8^{+0.1}_{-0.1}$	$191^{+0.2}_{-0.3}$	$345^{+0.0}_{-0.0}$
	6	$1.1^{+1.0}_{-0.8}$	$1.9^{+1.4}_{-1.0}$	$1.7^{+1.4}_{-1.2}$	$2.9^{+1.8}_{-2.3}$	$9^{+0.1}_{-0.3}$	$196^{+0.3}_{-0.9}$	$27^{+0.0}_{-0.0}$
	7	$0.1^{+0.4}_{-0.2}$	$0.1^{+0.3}_{-0.2}$	$-0.3^{+0.9}_{-0.9}$	$-1.2^{+1.1}_{-0.8}$	$0^{+0.1}_{-0.1}$	$-15^{+0.5}_{-0.3}$	$-103^{+0.0}_{-0.0}$
	8	$0.3^{+0.5}_{-0.3}$	$0.2^{+0.4}_{-0.3}$	$-0.8^{+1.0}_{-0.9}$	$-1.7^{+0.9}_{-0.9}$	$0^{+0.1}_{-0.1}$	$-31^{+0.3}_{-0.2}$	$-109^{+0.0}_{-0.0}$
	9	$1.3^{+0.3}_{-0.3}$	$1.0^{+0.3}_{-0.2}$	$7.0^{+1.3}_{-1.3}$	$17.4^{+2.8}_{-2.7}$	$15^{+0.1}_{-0.1}$	$368^{+0.8}_{-0.2}$	$992^{+0.0}_{-0.0}$
	10	$1.0^{+0.5}_{-0.3}$	$1.0^{+0.4}_{-0.3}$	$5.0^{+1.4}_{-1.0}$	$12.4^{+2.9}_{-2.2}$	$10^{+0.1}_{-0.1}$	$258^{+0.4}_{-0.2}$	$649^{+0.0}_{-0.0}$
	11	$1.3^{+0.4}_{-0.3}$	$1.3^{+0.4}_{-0.3}$	$4.9^{+0.9}_{-0.8}$	$12.2^{+1.4}_{-1.2}$	$10^{+0.1}_{-0.1}$	$212^{+0.2}_{-0.3}$	$493^{+0.0}_{-0.0}$
	12	$1.0^{+0.4}_{-0.4}$	$0.7^{+0.4}_{-0.3}$	$3.5^{+1.6}_{-1.1}$	$8.6^{+4.2}_{-2.8}$	$8^{+0.2}_{-0.1}$	$194^{+0.5}_{-0.4}$	$434^{+0.0}_{-0.1}$
	13	$0.6^{+0.7}_{-0.4}$	$0.3^{+0.4}_{-0.2}$	$0.7^{+0.7}_{-0.7}$	$1.4^{+1.2}_{-1.0}$	$2^{+0.0}_{-0.1}$	$78^{+0.4}_{-0.2}$	$217^{+0.0}_{-0.1}$
	14	$0.3^{+0.4}_{-0.2}$	$0.3^{+0.4}_{-0.3}$	$-0.1^{+0.8}_{-0.8}$	$-0.3^{+0.6}_{-0.6}$	$3^{+0.1}_{-0.1}$	$72^{+0.2}_{-0.3}$	$165^{+0.0}_{-0.0}$
	15	$0.0^{+0.3}_{-0.2}$	$0.0^{+0.3}_{-0.2}$	$0.4^{+0.9}_{-0.8}$	$0.9^{+2.0}_{-1.4}$	$2^{+0.1}_{-0.1}$	$109^{+0.2}_{-0.3}$	$125^{+0.0}_{-0.0}$
	16	$4.1^{+2.3}_{-1.3}$	$2.7^{+1.0}_{-0.7}$	$22.2^{+10.4}_{-5.8}$	$56.0^{+26.7}_{-15.2}$	$60^{+1.4}_{-0.9}$	$975^{+4.0}_{-1.8}$	$2442^{+0.2}_{-0.5}$
	17	$3.3^{+1.1}_{-0.7}$	$3.0^{+0.7}_{-0.7}$	$11.7^{+2.6}_{-1.5}$	$24.8^{+7.1}_{-3.2}$	$42^{+0.8}_{-0.6}$	$719^{+1.8}_{-1.3}$	$1680^{+0.1}_{-0.1}$
	18	$2.8^{+0.7}_{-0.5}$	$1.8^{+0.5}_{-0.5}$	$11.9^{+1.7}_{-2.2}$	$27.6^{+3.6}_{-6.3}$	$33^{+0.2}_{-0.6}$	$598^{+1.3}_{-1.2}$	$1109^{+0.4}_{-0.2}$
	19	$2.1^{+1.1}_{-0.7}$	$1.4^{+0.7}_{-0.4}$	$6.0^{+1.6}_{-1.6}$	$8.9^{+2.3}_{-2.5}$	$13^{+0.1}_{-0.1}$	$233^{+0.8}_{-0.8}$	$624^{+0.0}_{-0.2}$
	20	$1.1^{+0.7}_{-0.3}$	$1.4^{+0.5}_{-0.4}$	$1.9^{+1.0}_{-0.8}$	$2.0^{+1.1}_{-1.2}$	$7^{+0.1}_{-0.1}$	$127^{+0.2}_{-0.2}$	$136^{+0.1}_{-0.0}$
	21	$0.2^{+0.4}_{-0.2}$	$0.2^{+0.4}_{-0.2}$	$0.2^{+0.8}_{-0.8}$	$-1.5^{+1.1}_{-0.9}$	$1^{+0.1}_{-0.1}$	$43^{+0.3}_{-0.2}$	$65^{+0.1}_{-0.2}$
	22	$0.8^{+0.6}_{-0.3}$	$1.2^{+0.7}_{-0.5}$	$1.2^{+0.9}_{-0.8}$	$0.2^{+2.0}_{-1.1}$	$2^{+0.1}_{-0.1}$	$44^{+0.1}_{-0.1}$	$-49^{+0.0}_{-0.0}$
	23	$1.3^{+0.4}_{-0.3}$	$1.1^{+0.3}_{-0.3}$	$6.2^{+1.2}_{-1.1}$	$14.1^{+3.7}_{-2.5}$	$12^{+0.2}_{-0.1}$	$330^{+1.0}_{-0.9}$	$1072^{+0.1}_{-0.2}$
	24	$1.1^{+0.3}_{-0.3}$	$1.0^{+0.4}_{-0.2}$	$4.7^{+0.8}_{-1.0}$	$10.9^{+1.7}_{-1.7}$	$9^{+0.1}_{-0.1}$	$232^{+0.2}_{-0.2}$	$622^{+0.0}_{-0.0}$
	25	$1.3^{+0.4}_{-0.3}$	$1.1^{+0.3}_{-0.3}$	$6.0^{+0.8}_{-1.4}$	$14.6^{+2.4}_{-2.1}$	$12^{+0.1}_{-0.1}$	$267^{+0.5}_{-0.4}$	$582^{+0.0}_{-0.0}$
	26	$2.1^{+0.7}_{-0.5}$	$2.0^{+0.6}_{-0.5}$	$6.6^{+1.9}_{-1.0}$	$15.6^{+3.7}_{-2.0}$	$18^{+0.1}_{-0.1}$	$359^{+0.5}_{-0.6}$	$728^{+0.0}_{-0.0}$
	27	$1.2^{+0.4}_{-0.3}$	$0.9^{+0.4}_{-0.2}$	$5.8^{+0.8}_{-0.9}$	$14.0^{+1.3}_{-1.8}$	$13^{+0.1}_{-0.1}$	$322^{+0.3}_{-0.4}$	$745^{+0.0}_{-0.1}$
	28	$1.6^{+0.3}_{-0.4}$	$1.0^{+0.3}_{-0.2}$	$9.7^{+2.0}_{-1.8}$	$25.4^{+5.1}_{-4.9}$	$22^{+0.2}_{-0.2}$	$419^{+0.3}_{-0.4}$	$738^{+0.0}_{-0.1}$
	29	$2.2^{+0.4}_{-0.3}$	$1.1^{+0.3}_{-0.2}$	$13.7^{+2.4}_{-2.1}$	$39.1^{+4.8}_{-5.1}$	$28^{+0.2}_{-0.2}$	$422^{+0.4}_{-0.5}$	$881^{+0.1}_{-0.0}$
N144	1	$30.8^{+35.4}_{-11.7}$	$41.4^{+40.8}_{-16.4}$	$155.9^{+183.5}_{-49.0}$	$349.0^{+480.9}_{-140.6}$	$3395^{+897.8}_{-97.9}$	$25553^{+538.2}_{-119.2}$	$7139^{+2.4}_{-0.6}$
	2	$17.7^{+10.8}_{-4.7}$	$16.9^{+7.6}_{-4.0}$	$54.8^{+24.8}_{-12.5}$	$119.8^{+68.2}_{-28.8}$	$693^{+22.0}_{-6.2}$	$10333^{+45.2}_{-36.1}$	$9751^{+0.9}_{-0.4}$
	3	$30.8^{+14.8}_{-9.6}$	$26.1^{+10.1}_{-5.2}$	$127.4^{+58.7}_{-41.2}$	$326.7^{+148.3}_{-113.8}$	$1141^{+57.8}_{-10.9}$	$14636^{+75.5}_{-27.4}$	$12672^{+0.2}_{-3.6}$
	4	$20.5^{+8.2}_{-4.6}$	$16.1^{+5.4}_{-2.3}$	$91.2^{+36.6}_{-17.7}$	$238.4^{+106.3}_{-49.3}$	$521^{+15.0}_{-5.5}$	$10182^{+21.5}_{-26.4}$	$7021^{+1.0}_{-0.4}$
	5	$12.7^{+5.4}_{-3.8}$	$11.1^{+3.8}_{-2.4}$	$55.9^{+24.5}_{-15.0}$	$141.7^{+65.3}_{-39.6}$	$272^{+2.0}_{-2.4}$	$4307^{+6.5}_{-4.5}$	$5174^{+0.2}_{-0.1}$
	6	$8.6^{+2.4}_{-1.5}$	$7.2^{+1.2}_{-0.8}$	$42.9^{+10.2}_{-5.3}$	$109.8^{+27.3}_{-13.5}$	$199^{+0.9}_{-1.2}$	$4150^{+7.2}_{-4.1}$	$4870^{+0.0}_{-0.1}$
	7	$8.2^{+2.5}_{-1.4}$	$6.5^{+1.7}_{-0.9}$	$41.6^{+7.6}_{-6.7}$	$103.9^{+19.4}_{-21.3}$	$122^{+1.4}_{-1.1}$	$2939^{+7.1}_{-8.3}$	$2929^{+0.4}_{-0.1}$

Table 5.1 (cont'd)

HII Region	Subregion	3.6μm (mJy)	4.5μm (mJy)	5.8μm (mJy)	8.0μm (mJy)	24μm (mJy)	70μm (mJy)	160μm (mJy)
	8	$2.4^{+1.8}_{-1.0}$	$2.3^{+1.1}_{-0.9}$	$16.1^{+2.9}_{-4.3}$	$35.0^{+7.6}_{-8.1}$	$51^{+0.5}_{-0.5}$	$1359^{+0.9}_{-1.2}$	$2022^{+0.1}_{-0.0}$
	9	$2.7^{+1.4}_{-1.0}$	$2.3^{+0.8}_{-0.6}$	$11.2^{+2.7}_{-2.7}$	$26.6^{+6.7}_{-5.9}$	$40^{+0.6}_{-0.5}$	$1112^{+3.6}_{-2.6}$	$1341^{+0.1}_{-0.1}$
	10	$7.2^{+3.5}_{-2.7}$	$6.8^{+2.6}_{-2.5}$	$42.6^{+18.0}_{-22.8}$	$82.6^{+44.6}_{-47.2}$	$514^{+23.8}_{-10.9}$	$13296^{+70.2}_{-111.3}$	$8417^{+3.9}_{-4.9}$
	11	$2.4^{+0.8}_{-0.7}$	$2.3^{+0.5}_{-0.4}$	$13.0^{+2.2}_{-2.3}$	$22.0^{+6.3}_{-4.6}$	$110^{+1.5}_{-1.2}$	$1566^{+1.1}_{-2.3}$	$3082^{+0.7}_{-0.1}$
	12	$2.5^{+1.1}_{-0.6}$	$3.3^{+0.6}_{-0.7}$	$11.1^{+1.7}_{-1.7}$	$22.8^{+3.8}_{-3.8}$	$79^{+0.4}_{-0.4}$	$1139^{+0.9}_{-0.6}$	$1692^{+0.5}_{-0.0}$
	13	$1.8^{+1.2}_{-0.7}$	$2.4^{+0.8}_{-0.6}$	$5.2^{+2.6}_{-1.1}$	$12.4^{+4.9}_{-2.7}$	$62^{+0.3}_{-0.2}$	$841^{+1.3}_{-0.7}$	$1148^{+0.2}_{-0.0}$
	14	$1.5^{+1.1}_{-0.6}$	$1.9^{+0.7}_{-0.4}$	$4.7^{+1.7}_{-1.8}$	$9.9^{+3.6}_{-1.9}$	$44^{+0.4}_{-0.2}$	$552^{+0.3}_{-0.8}$	$951^{+0.0}_{-0.0}$
	15	$1.2^{+0.7}_{-0.4}$	$1.6^{+0.5}_{-0.3}$	$3.2^{+1.7}_{-1.2}$	$8.7^{+3.1}_{-1.9}$	$37^{+0.1}_{-0.2}$	$402^{+0.6}_{-0.5}$	$734^{+0.1}_{-0.1}$
	16	$0.1^{+0.5}_{-0.3}$	$0.6^{+0.4}_{-0.3}$	$0.4^{+0.9}_{-0.7}$	$2.4^{+0.8}_{-0.7}$	$19^{+0.1}_{-0.1}$	$191^{+0.3}_{-0.3}$	$550^{+0.0}_{-0.0}$
	17	$0.2^{+0.6}_{-0.4}$	$0.5^{+0.5}_{-0.3}$	$0.3^{+0.7}_{-0.8}$	$2.0^{+0.7}_{-0.8}$	$11^{+0.1}_{-0.1}$	$87^{+0.2}_{-0.3}$	$372^{+0.1}_{-0.0}$
	18	$10.6^{+2.6}_{-1.6}$	$10.4^{+1.6}_{-1.1}$	$51.9^{+9.9}_{-11.0}$	$125.3^{+29.8}_{-30.6}$	$509^{+3.4}_{-3.1}$	$6054^{+13.1}_{-6.4}$	$6029^{+1.0}_{-0.3}$
	19	$11.4^{+4.9}_{-2.3}$	$9.6^{+2.8}_{-1.6}$	$52.4^{+12.5}_{-8.6}$	$135.5^{+30.3}_{-22.6}$	$310^{+3.4}_{-2.6}$	$3620^{+12.2}_{-8.3}$	$3770^{+0.3}_{-0.2}$
	20	$10.2^{+2.9}_{-2.4}$	$8.7^{+2.1}_{-1.5}$	$37.4^{+8.0}_{-7.8}$	$91.6^{+17.0}_{-19.3}$	$190^{+0.9}_{-1.2}$	$2125^{+2.6}_{-2.6}$	$2609^{+0.2}_{-1.2}$
	21	$2.2^{+0.8}_{-0.6}$	$2.3^{+0.6}_{-0.5}$	$10.1^{+2.1}_{-1.7}$	$21.8^{+5.2}_{-5.1}$	$58^{+0.8}_{-0.7}$	$898^{+3.6}_{-2.7}$	$1576^{+0.2}_{-0.4}$
	22	$1.7^{+0.8}_{-0.5}$	$1.6^{+0.6}_{-0.3}$	$7.7^{+1.8}_{-1.5}$	$18.4^{+4.7}_{-4.5}$	$38^{+0.3}_{-0.3}$	$616^{+1.2}_{-1.3}$	$871^{+0.3}_{-0.2}$
	23	$0.9^{+0.6}_{-0.4}$	$0.8^{+0.5}_{-0.3}$	$4.4^{+1.3}_{-1.1}$	$8.4^{+2.2}_{-1.3}$	$17^{+0.3}_{-0.2}$	$337^{+0.9}_{-0.7}$	$666^{+0.0}_{-0.1}$
	24	$10.6^{+3.9}_{-2.0}$	$10.9^{+3.0}_{-2.3}$	$34.2^{+9.8}_{-5.9}$	$52.8^{+20.1}_{-17.6}$	$510^{+13.0}_{-3.2}$	$6480^{+98.2}_{-47.4}$	$4636^{+0.4}_{-0.8}$
	25	$9.6^{+6.1}_{-3.5}$	$8.5^{+4.1}_{-3.0}$	$17.6^{+6.4}_{-6.0}$	$23.9^{+9.1}_{-8.7}$	$179^{+1.0}_{-2.2}$	$1660^{+3.4}_{-2.9}$	$3051^{+0.2}_{-1.1}$
	26	$4.6^{+1.8}_{-1.1}$	$4.4^{+1.3}_{-0.7}$	$10.5^{+7.0}_{-3.3}$	$15.0^{+18.5}_{-6.0}$	$105^{+1.3}_{-0.7}$	$968^{+3.1}_{-0.9}$	$1371^{+0.2}_{-0.1}$
	27	$3.9^{+1.5}_{-0.9}$	$3.9^{+1.0}_{-0.6}$	$9.1^{+2.9}_{-1.4}$	$13.8^{+5.3}_{-2.0}$	$83^{+0.7}_{-0.5}$	$864^{+2.1}_{-1.5}$	$1309^{+0.0}_{-0.1}$
	28	$2.4^{+2.6}_{-0.5}$	$2.5^{+1.6}_{-0.4}$	$8.5^{+5.5}_{-1.8}$	$11.4^{+16.0}_{-2.7}$	$53^{+0.7}_{-0.4}$	$630^{+2.0}_{-0.5}$	$1167^{+0.0}_{-0.0}$
	29	$2.9^{+1.3}_{-0.6}$	$2.9^{+1.0}_{-0.7}$	$10.0^{+2.6}_{-2.5}$	$23.5^{+5.4}_{-6.0}$	$51^{+0.4}_{-0.4}$	$714^{+0.4}_{-0.8}$	$1369^{+0.1}_{-0.1}$
	30	$4.2^{+1.6}_{-0.9}$	$4.2^{+0.7}_{-0.6}$	$16.0^{+4.3}_{-2.9}$	$39.6^{+13.4}_{-8.2}$	$66^{+0.5}_{-0.3}$	$1000^{+1.1}_{-1.2}$	$1924^{+0.0}_{-0.2}$
	31	$3.6^{+1.2}_{-1.1}$	$3.1^{+0.8}_{-0.5}$	$10.7^{+4.0}_{-2.0}$	$26.3^{+7.4}_{-4.8}$	$52^{+0.4}_{-0.3}$	$1046^{+1.0}_{-0.9}$	$1715^{+0.1}_{-0.1}$

[a]The flux densities are measured via 40″-diameter circular apertures and are background subtracted. Negative flux values indicate that the aperture fluxes are similar to the background fluxes.

Our SEDs, as derived from median-filtered images, were also compared to SEDs made from SAGE's smoothed and point-source-subtracted residual images (Meixner et al. 2006). Though SEDs were almost identical, there were a few situations where the SEDs from the residual images seemed to produce unphysical results, for example, an inexplicable rise of N180's SEDs at 4.5 μm.

Finally, we used these photometric measurements to construct CCDs for each H II region to search for SED slope changes and color groupings among the subregions. The color magnitudes were calculated based on the Vega zero-magnitude flux densities: 280.9 ± 4.1, 179.7 ± 2.6, 115.0 ± 1.7, and 64.13 ± 0.94 Jy for the 3.6, 4.5, 5.8, and 8.0 μm bands respectively (Reach et al. 2005) and 7.17 ± 0.11 Jy for 24 μm (Rieke et al. 2008). CCDs including 70 and 160 um measurements were not included due to lack of distinct spectral features seen in SEDs, low pixel count sampled, and lack of zero-magnitude flux at these wavelengths in the literature. CCDs for each regions can be seen in panels (c) and (d) of Figures 5.4-5.7.

5.4.2 SED Modeling

In order to study the dust properties in each subregion, we simulated the SEDs using the dust emission modeling tool `DustEM`[2] (Compiègne et al. 2011). The `DustEM` code allows an arbitrary combination of various grain types as input and produces a model SED based on the incident radiation field strength and grain physics in the optically thin limit. We adopted the Désert et al. (1990) dust model implemented in `DustEM`, which includes three dust grain populations: polycyclic aromatic hydrocarbons (PAHs), VSGs composed of amorphous carbon, and big grains (BGs) made of astronomical silicates. The free parameters in the SED fitting include the mass column density of each dust populations and the ISRF parameter U, as scaled from the solar neighborhood ISRF described by Mathis et al. (1983).

The model SEDs were integrated over the filter transmission[3] of each band to get photometric fluxes. The model fluxes were compared with the observed fluxes, and the smallest χ^2 value was used to determine the best-fit model. As the 3.6 and 4.5 μm flux densities are potentially contaminated by starlight, Brα line, and/or molecular hydrogen lines (Flagey et al. 2006; Churchwell et al. 2004; De Buizer & Vacca 2010), they were excluded in the SED fitting (more on this below). We note that the value found for U is primarily constrained by the band flux ratio of 70 and 160 μm, and the PAHs and VSG mass column densities are most sensitive to IRAC bands and 24 μm band, respectively.

Table 5.2 summarizes the modeling results. The best-fit dust composition is given as $Y_{\rm PAH}/Y_{\rm DUST}$ and $Y_{\rm VSG}/Y_{\rm BG}$, in which Y is the dust mass abundance for a given grain type. The visual extinction, A_V, was derived from the modeled extinction curve and is an indication of the dust column density. The median and range of the BG equilibrium temperatures, $T_{\rm eq}$, are also listed in the table and are highly dependent on the value of the modeled U. $T_{\rm eq}$ values in each region typically peak toward the center and decreases radially.

[2] `http://www.ias.u-psud.fr/DUSTEM/`
[3] `http://www.astro.caltech.edu/~capak/cosmos/filters/`

Table 5.2. Dust Properties from SED Modeling[a]

HII Region	Subregion	U[b]	$Y_{\rm PAH}/Y_{\rm DUST}$ ($\times10^{-2}$)	$Y_{\rm VSG}/Y_{\rm BG}$ ($\times10^{-2}$)	$T_{\rm eq}$ (K)	$A_{\rm V}$[c] (mag)
N63	1	267.6±16.1	4.4±4.8	33.2±4.3	$48.4^{+1.4}_{-4.5}$	0.07±0.01
	2	6.5±0.1	5.0±0.7	39.8±1.9	$25.2^{+0.7}_{-2.3}$	0.47±0.01
	3	6.7±0.2	5.8±1.1	27.8±2.2	$25.3^{+0.7}_{-2.3}$	0.33±0.01
	4	8.3±0.3	7.6±1.9	21.4±3.3	$26.2^{+0.7}_{-2.4}$	0.21±0.01
	5	9.9±0.1	8.9±0.6	6.7±0.8	$27.0^{+0.7}_{-2.4}$	0.12±0.01
	6	5.7±0.1	4.8±1.0	8.9±1.3	$24.6^{+0.7}_{-2.2}$	0.15±0.01
	7	5.0±0.1	1.2±1.0	5.3±1.0	$24.0^{+0.7}_{-2.2}$	0.21±0.01
	8	37.1±15.4	2.7±2.2	62.7±79.1	$34.1^{+1.0}_{-3.1}$	0.19±0.12
	9	6.8±0.4	6.5±2.9	7.6±3.8	$25.3^{+0.7}_{-2.3}$	0.64±0.03
	10	1.1±0.5	9.5±5.7	3.7±11.6	$18.5^{+0.5}_{-1.6}$	1.14±0.34
	11	...	...	...	...	...
	12	...	...	...	...	...
	13	9.2±0.2	5.9±0.9	87.4±4.3	$26.7^{+0.7}_{-2.4}$	0.46±0.01
	14	5.6±0.2	6.6±1.3	21.2±2.4	$24.5^{+0.7}_{-2.2}$	0.61±0.01
	15	5.8±0.3	11.2±1.7	10.5±2.9	$24.6^{+0.7}_{-2.2}$	0.54±0.02
	16	9.5±0.1	6.7±0.9	8.3±1.2	$26.8^{+0.7}_{-2.4}$	0.29±0.01
	17	21.7±0.3	7.6±2.3	5.0±2.4	$31.0^{+0.9}_{-2.8}$	0.09±0.01
	18	21.0±0.4	2.5±0.5	43.0±2.5	$30.8^{+0.9}_{-2.8}$	0.14±0.01
	19	4.0±0.1	3.6±1.1	24.5±2.1	$23.1^{+0.6}_{-2.1}$	0.40±0.01
	20	5.8±0.1	6.4±0.9	13.1±1.3	$24.6^{+0.7}_{-2.2}$	0.30±0.01
	21	3.9±0.1	5.6±0.9	6.9±1.2	$23.0^{+0.6}_{-2.1}$	0.42±0.01
	22	4.0±0.2	10.4±1.3	5.4±1.9	$23.1^{+0.6}_{-2.1}$	0.43±0.01
N180	1	14.6±0.3	5.3±1.6	41.3±3.2	$28.9^{+0.8}_{-2.6}$	0.83±0.03
	2	9.3±0.1	4.9±0.7	39.4±1.4	$26.7^{+0.7}_{-2.4}$	0.91±0.01
	3	6.3±0.2	8.2±0.9	45.5±2.8	$25.0^{+0.7}_{-2.2}$	1.25±0.03
	4	9.5±0.3	5.8±1.6	28.6±2.9	$26.8^{+0.7}_{-2.4}$	0.95±0.03
	5	7.9±0.4	10.3±2.5	4.4±3.2	$26.0^{+0.7}_{-2.3}$	0.94±0.04
	6	3.4±0.0	10.1±0.1	0.0±0.0	$22.5^{+0.6}_{-2.0}$	1.65±0.01
	7	3.2±0.1	8.3±0.5	0.7±0.6	$22.3^{+0.6}_{-2.0}$	0.97±0.01
	8	3.8±0.0	10.1±0.1	0.0±0.0	$22.9^{+0.6}_{-2.0}$	0.72±0.01
	9	2.5±0.0	8.6±0.1	0.0±0.0	$21.3^{+0.6}_{-1.9}$	1.01±0.01
	10	1.4±0.0	7.2±0.1	0.0±0.0	$19.3^{+0.5}_{-1.7}$	1.69±0.01
	11	1.9±0.0	10.2±0.0	0.0±0.0	$20.3^{+0.5}_{-1.8}$	1.08±0.01
	12	0.8±0.1	4.3±1.0	5.5±1.7	$17.5^{+0.5}_{-1.5}$	2.36±0.12
	13	1.9±0.0	10.9±0.1	0.0±0.0	$20.3^{+0.5}_{-1.8}$	0.85±0.01
	14	18.0±0.1	6.0±0.7	22.3±1.0	$30.0^{+0.8}_{-2.7}$	0.60±0.01
	15	15.6±0.2	5.8±1.1	14.8±1.4	$29.3^{+0.8}_{-2.7}$	0.47±0.01
	16	7.5±0.1	6.1±0.8	11.7±1.1	$25.7^{+0.7}_{-2.3}$	0.38±0.01
	17	9.0±0.1	5.2±0.8	9.5±1.0	$26.6^{+0.7}_{-2.4}$	0.21±0.01

Table 5.2 (cont'd)

HII Region	Subregion	U[b]	$Y_{\rm PAH}/Y_{\rm DUST}$ ($\times10^{-2}$)	$Y_{\rm VSG}/Y_{\rm BG}$ ($\times10^{-2}$)	$T_{\rm eq}$ (K)	$A_{\rm V}$[c] (mag)
	18	8.0±0.2	5.4±1.9	1.8±2.0	$26.0^{+0.7}_{-2.4}$	0.11±0.01
	19	10.9±0.2	0.0±1.7	2.3±1.6	$27.5^{+0.8}_{-2.5}$	0.03±0.01
	20	64.0±0.2	9.5±0.3	0.0±0.0	$37.5^{+1.1}_{-3.5}$	0.01±0.01
N70	1	5.6±0.1	7.8±0.7	1.7±0.9	$24.4^{+0.7}_{-2.2}$	0.48±0.01
	2	9.1±0.4	8.4±3.0	6.6±3.7	$26.6^{+0.7}_{-2.4}$	0.21±0.01
	3	5.5±0.1	5.8±0.7	14.8±1.2	$24.4^{+0.7}_{-2.2}$	0.27±0.01
	4	13.4±0.5	13.5±2.8	5.1±3.6	$28.5^{+0.8}_{-2.6}$	0.07±0.01
	5	6.9±0.2	5.0±1.7	8.3±2.2	$25.4^{+0.7}_{-2.3}$	0.08±0.01
	7	...	...	...	...	...
	8	...	...	...	...	...
	9	4.4±0.1	8.1±0.9	1.1±1.0	$23.5^{+0.6}_{-2.1}$	0.32±0.01
	10	4.9±0.1	8.5±1.2	1.1±1.4	$23.9^{+0.7}_{-2.1}$	0.19±0.01
	11	5.3±0.1	10.4±0.8	1.8±1.0	$24.3^{+0.7}_{-2.2}$	0.14±0.01
	12	5.5±0.3	8.4±2.2	3.0±2.7	$24.4^{+0.7}_{-2.2}$	0.12±0.01
	13	3.8±0.2	2.7±2.0	4.7±2.3	$22.9^{+0.6}_{-2.0}$	0.08±0.01
	14	4.4±0.1	2.0±1.5	10.6±1.9	$23.5^{+0.6}_{-2.1}$	0.05±0.01
	15	15.8±0.5	1.5±3.6	6.6±3.7	$29.3^{+0.8}_{-2.7}$	0.02±0.01
	16	4.5±0.3	10.5±2.1	4.0±3.0	$23.5^{+0.6}_{-2.1}$	0.79±0.03
	17	4.4±0.1	7.4±0.9	8.2±1.3	$23.5^{+0.6}_{-2.1}$	0.54±0.01
	18	7.0±0.2	10.3±1.1	5.3±1.4	$25.4^{+0.7}_{-2.3}$	0.26±0.01
	19	3.7±0.2	7.6±1.4	6.4±2.0	$22.8^{+0.6}_{-2.0}$	0.23±0.01
	20	16.2±0.4	4.7±2.5	19.9±3.4	$29.4^{+0.8}_{-2.7}$	0.02±0.01
	21	8.5±0.1	0.0±0.0	15.5±0.7	$26.3^{+0.7}_{-2.4}$	0.01±0.01
	22	...	...	...	...	...
	23	3.5±0.1	6.9±0.9	0.5±1.0	$22.5^{+0.6}_{-2.0}$	0.41±0.01
	24	4.5±0.1	8.1±0.9	0.5±1.0	$23.6^{+0.6}_{-2.1}$	0.20±0.01
	25	6.0±0.2	10.4±1.1	1.3±1.3	$24.8^{+0.7}_{-2.2}$	0.15±0.01
	26	6.2±0.1	9.0±1.1	4.5±1.4	$24.9^{+0.7}_{-2.2}$	0.19±0.01
	27	5.3±0.1	8.2±0.7	2.2±0.8	$24.3^{+0.7}_{-2.2}$	0.21±0.01
	28	8.2±0.2	12.4±1.5	1.8±1.9	$26.1^{+0.7}_{-2.4}$	0.16±0.01
	29	6.4±0.0	15.8±0.1	0.0±0.0	$25.0^{+0.7}_{-2.3}$	0.23±0.01
N144	1	501.3±25.9	3.6±1.9	12.6±1.5	$54.2^{+1.5}_{-5.0}$	0.14±0.01
	2	20.7±0.2	5.0±1.1	28.6±1.8	$30.7^{+0.9}_{-2.8}$	1.02±0.02
	3	25.4±0.3	8.4±2.2	31.9±3.6	$31.9^{+0.9}_{-2.9}$	1.15±0.05
	4	43.8±0.4	7.4±1.7	13.9±1.7	$35.1^{+1.0}_{-3.2}$	0.48±0.02
	5	13.1±0.4	9.3±2.2	15.2±3.1	$28.4^{+0.8}_{-2.6}$	0.78±0.03
	6	14.6±0.1	7.3±0.9	10.3±1.1	$28.9^{+0.8}_{-2.6}$	0.68±0.01
	7	20.9±0.2	9.9±1.3	4.7±1.4	$30.8^{+0.9}_{-2.8}$	0.34±0.01
	8	10.2±0.1	6.7±1.0	5.2±1.2	$27.2^{+0.8}_{-2.5}$	0.36±0.01

Table 5.2 (cont'd)

HII Region	Subregion	U[b]	$Y_{\rm PAH}/Y_{\rm DUST}$ ($\times10^{-2}$)	$Y_{\rm VSG}/Y_{\rm BG}$ ($\times10^{-2}$)	$T_{\rm eq}$ (K)	$A_{\rm V}$[c] (mag)
	9	14.5±0.2	6.6±1.1	6.1±1.3	$28.9^{+0.8}_{-2.6}$	0.19±0.01
	10	53.7±0.8	2.2±0.9	13.5±1.0	$36.4^{+1.0}_{-3.4}$	0.51±0.01
	11	4.5±0.1	3.9±0.6	20.7±1.1	$23.5^{+0.6}_{-2.1}$	0.99±0.01
	12	7.7±0.1	5.8±0.7	22.2±1.1	$25.9^{+0.7}_{-2.3}$	0.36±0.01
	13	8.3±0.1	4.2±1.0	30.1±1.8	$26.2^{+0.7}_{-2.4}$	0.23±0.01
	14	5.0±0.1	4.6±1.0	28.7±2.0	$24.0^{+0.7}_{-2.2}$	0.28±0.01
	15	3.9±0.1	5.1±1.2	33.8±3.0	$23.0^{+0.6}_{-2.1}$	0.26±0.01
	16	1.4±0.0	1.8±0.7	29.8±1.7	$19.3^{+0.5}_{-1.7}$	0.46±0.01
	17	0.9±0.0	8.2±0.7	18.7±2.3	$17.8^{+0.5}_{-1.6}$	0.46±0.01
	18	17.7±0.2	11.3±1.0	29.0±1.8	$29.9^{+0.8}_{-2.7}$	0.72±0.01
	19	15.7±0.3	11.5±1.5	29.6±2.8	$29.3^{+0.8}_{-2.7}$	0.49±0.01
	20	11.0±0.3	12.5±1.6	26.4±3.2	$27.5^{+0.8}_{-2.5}$	0.44±0.01
	21	6.2±0.1	6.3±0.9	15.7±1.5	$24.9^{+0.7}_{-2.2}$	0.40±0.01
	22	9.6±0.2	8.0±1.3	14.8±1.9	$26.9^{+0.7}_{-2.4}$	0.16±0.01
	23	5.6±0.1	5.7±0.9	10.1±1.3	$24.5^{+0.7}_{-2.2}$	0.18±0.01
	24	41.3±1.0	3.6±0.9	48.1±2.2	$34.7^{+1.0}_{-3.2}$	0.28±0.01
	25	3.3±0.1	7.4±1.0	40.6±3.2	$22.4^{+0.6}_{-2.0}$	1.27±0.03
	26	4.8±0.4	5.9±2.5	63.0±9.3	$23.9^{+0.7}_{-2.1}$	0.43±0.03
	27	5.2±0.1	5.1±0.9	45.0±2.5	$24.1^{+0.7}_{-2.2}$	0.38±0.01
	28	4.4±0.2	5.6±1.9	27.1±4.0	$23.5^{+0.6}_{-2.1}$	0.38±0.01
	29	5.3±0.2	7.7±1.2	15.4±2.1	$24.2^{+0.7}_{-2.2}$	0.39±0.01
	30	5.8±0.2	9.0±1.4	11.1±2.1	$24.6^{+0.7}_{-2.2}$	0.52±0.01
	31	7.8±0.1	6.2±1.0	10.2±1.3	$26.0^{+0.7}_{-2.3}$	0.37±0.01

[a]Using the Levenberg-Marquardt minimization method implemented in IDL (`http://www.physics.wisc.edu/~craigm/idl/fitting.html`).

[b]ISRF scaled from the solar neighborhood ISRF described in Mathis et al. (1983).

[c]The errors in the fitted A_V is approximated to be at least 0.01.

An example of the dust emission model is shown in Figure 5.8 for N180 subregion 2 (high $Y_{\rm VSG}/Y_{\rm BG}$) and subregion 6 (high $Y_{\rm PAH}/Y_{\rm DUST}$). The model emission contributed by three grain populations are presented in dashed or dotted lines, with the total emission in the solid blue line. While the model SED reproduced the photometric flux densities included in the SED fitting, it did not predict 3.6 and 4.5 μm well. In fact, for most locations of our four regions, the 4.5 μm dust emission produced by the Désert et al. (1990) model is much lower than the observed one. To explain the 3.6 and 4.5 μm discrepancy, we tested more complicated PAHs models from Draine & Li (2007) and Compiègne et al. (2011) (also implemented in `DustEM`), which have both neutral and ionized PAHs. Although the usual small discrepancy (less than a factor of 3) at 3.6 μm can be explained by adjusting the PAH ionization fraction, the 4.5 μm dust model flux is still underpredicted. Thus, for our dust modeling, we excluded the 3.6 and 4.5 μm bands from our SED fits. Due to the lack of 4-5 μm spectroscopic observations to resolve the line and continuum emission, any further interpretation is beyond the scope of this work. Therefore, we have 5 fixed parameters (two IRAC and three MIPS bands) and 4 fitted parameters ($Y_{\rm PAH}$, $Y_{\rm VSG}$, $Y_{\rm BG}$, and U).

We note that the Désert et al. (1990) modeling of VSGs differs from many recent dust models (e.g.,

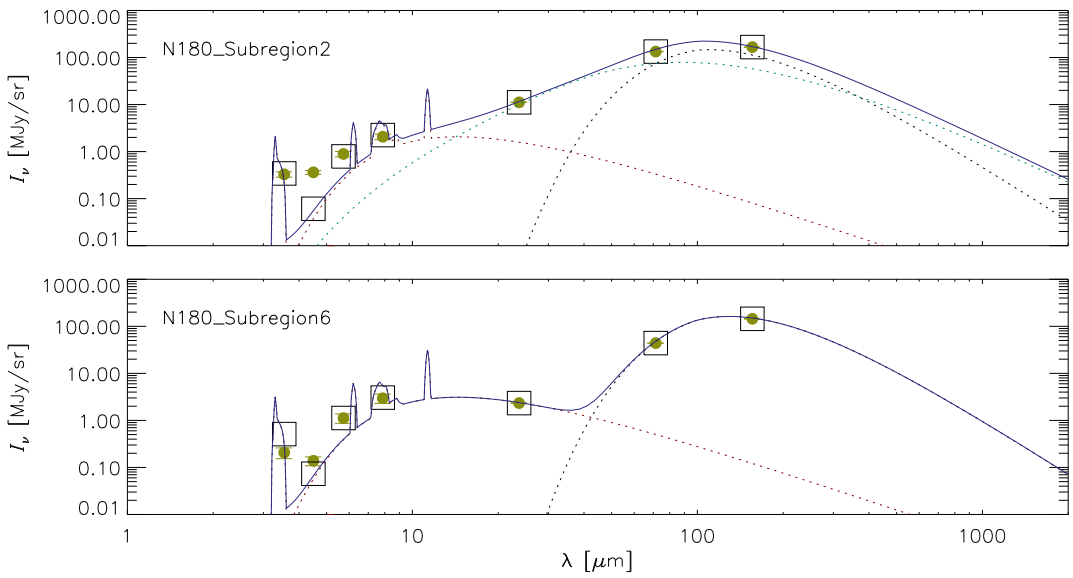

Figure 5.8 Examples of DUSTEM SED fits for subregions in N180. We present a VSG dominated subregion (top panel) and a PAH dominated subregion (bottom panel). Contributions from each of the three grains are shown with dashed lines in different colors, with maroon showing PAHs, teal showing VSGs, and black showing BGs. The sum of the emission of the three dust components is show by the solid blue line. Yellow points and error bars show points of the IRAC/MIPS photometric SED. Squares show the fitted locations at the wavelength of each IRAC/MIPS band.

Draine & Li 2007; Compiègne et al. 2010). VSGs in newer models are typically modeled by distributions of two different grain types, including a smaller grain that behaves more like PAHs. However, due to a limit in the number of bands, our data are best modeled by one VSG component, which, in the Désert et al. (1990) model, consists of "middle-sized" VSGs. This grain is highly dependent on whether or not an SED has a 24 μm excess. With only 3 grain types, we also note that BG and VSG are typically anti-correlated; thus, the change in the fraction of $Y_{\rm VSG}/Y_{\rm BG}$ may be somewhat over-exaggerated.

5.5 Analysis

For each H II region we have located massive stars throughout the region to estimate the radiation field, constructed and fitted SEDs for the radially placed subregions, and created CCDs for the subregions. The combination of the results are presented for each region in Figures 5.4-5.7.

For each figure, panel (a) shows the region as observed in the Hα line and the IRAC 8.0 μm band as well as the ISRF calculated from stars (Section 3.2). The sampled subregions are shown on top of the 8.0 μm image. Contours of H I column density are shown in red and CO column density in blue. The radiation field can be compared to the morphology of the H II region to assess radial variations of dust properties due to massive stars.

Panel (b) shows the results of the best-fit `DustEM` model for the SED of each subregion as a function of offset from the central subregion. These fitted parameters include the visual extinction (A_V), fitted ISRF (with magenta and cyan colors to show the ISRF as derived from stars for comparison), the ratio of PAH mass abundance to total dust mass abundance ($Y_{\rm PAH}/Y_{\rm DUST}$), and the ratio of VSG mass abundance to BG mass abundance ($Y_{\rm VSG}/Y_{\rm BG}$). Subregions with photometric measurements approximately equal to the background are excluded from the panel.

For panels (c) and (d) we show [3.6]-[4.5] vs [5.8]-[8.0] and [4.5]-[5.8] vs [8.0]-[24] CCDs, respectively. Note that IRAC bands 1 (3.6 μm), 3 (5.8 μm), and 4 (8.0 μm) contain PAH emission, while IRAC bands 2 (4.5 μm) and the MIPS 24 μm band do not. Therefore, in our CCDs, a subregion with a higher PAH mass fraction (i.e., higher fractional PAH emission) should have a smaller [3.6]-[4.5], a larger [4.5]-[5.8], and a lower [8.0]-[24]. In other words, we expect subregions with an increased PAH mass fraction to be toward the bottom of the [3.6]-[4.5] vs [5.8]-[8.0] CCD and toward the top left for the [4.5]-[5.8] vs [8.0]-[24] CCD. Subregions that are not present in these CCDs are those whose surface brightnesses are low and approach that of the background subregion for the H II region.

5.5.1 Classical H II Regions - N63, N180

N63

The classical HII region N63 has a central concentration of massive stars surrounded by a scattered distribution. The ISRF is centrally peaked at subregions 1, 2, 13, 18, and 19 (Figure 5.4). The SNR N63A (marked by X-ray contours in Figure 5.1) dominates emission at 24 μm (see Figure 5.2) in subregions 1, 8, and 18 due to the heated dust emission and the [O IV] 25.89 μm line (Caulet & Williams 2012, D. Segura-Cox et al. in preparation); thus, locations of these subregions on the [4.5]-[5.8] vs [8.0]-[24.0] CCD and the `DustEM` fits should be interpreted with caution. Large-scale molecular clouds as surveyed by NANTEN (Fukui et al. 2008) were undetected. However, supplemental ESO-SEST CO observations found molecular emission and are shown in Figure 5.4a (with the region observed outlined in blue, D. Segura-Cox et al. in preparation). We note that the 8.0 μm emission and the CO emission are coincident with each other.

For the CCD in Figure 5.4c, we have three subregion groups (ignoring the faint emission from subregion 7): (1) 9, 15, and 22, (2) 5, 6, 18, and 19, and (3) all others. Group 1 has the most fractional PAH emission; subregion 9 is contained within a molecular cloud, subregion 15 straddles the boundary between ionized gas and a dust lane, and subregion 22 is located just outside the H II region. These environments are where photodissociation regions (PDRs) are expected; thus, their high fractional PAH emission is not surprising. Group 2 indicates the least fractional PAH emission. Subregions 18 and 19 have a high radiation field which likely destroys the PAHs, while subregions 5 and 6 are toward the low-density edge of the H II region where the gas might be optically thin to the ionizing flux and PAHs are destroyed.

The CCD in Figure 5.4d shows a slight diagonal spread toward the top-left (most PAH). Subregions toward the center of N63 have by far the lowest fractional PAH emission and those farthest away have the highest. The fractional PAH emission appears to gradually increase radially without large jumps, likely because the PDRs are smeared by the large aperture size and line-of-sight integration for the subregions.

`DustEM` modeling shows that PAH fraction slightly increases outward from the central OB association of N63, consistent with the observations. In addition to its effect on PAH features, the OB association may also play a role in the increased $Y_{\rm VSG}/Y_{\rm BG}$ fraction (Figure 5.4b), which peaks strongly at the locations of the highest radiation field and falls off along the radiation field.

N180

N180 is a classical H II region powered by a central OB-association, whose stars are concentrated at the center of the diagonal cut on subregions 1 through 3 (Figure 5.5). Following the diagonal cut southwest, molecular gas becomes prevalent in subregions 2 through 13. Northeast of the central OB association, the

remaining subregions 14-20 contain little to no molecular gas and are located progressively further away from the massive stars.

The CCD of N180 in Figure 5.5d exhibits three major subregion groups: (1) 1-4, (2) 14-17, and (3) 5-13, where subregions 19-20 are not significantly above the background and thus not included in the CCD. Group 1, located at the peaks of the ISRF and projected within the molecular cloud (Figure 5.5a), has the highest [8.0]-[24.0] and the lowest [4.5]-[5.8] of all the subregion groups, i.e., it has the smallest PAH mass fraction.

Group 2 is located to the northeast of group 1 and is less affected by radiation from the massive stars. As the CCD indicates, PAH emission is increased in this group as compared to group 1, likely due to the fact that there is less harsh UV radiation to destroy PAHs. Moreover, PAH features are the most prevalent in group 3, whose subregions are deep in the molecular cloud and are far away from massive stars; thus, these locations have more available molecular gas and less destructive stellar radiation. The fitted results for the PAH fraction of dust agree with these results, with an overall increasing trend from the central subregions of group 1 toward group 3.

As with N63, the $Y_{\rm VSG}/Y_{\rm BG}$ fraction of N180 also peaks strongly at the locations of the highest radiation field (Figure 5.5b). Furthermore, it decreases rapidly to the southwest and more gradually to the northeast. The more dramatic decrease toward the southwest may be an indication of an increased fraction of BG inside the molecular cloud.

5.5.2 Superbubbles - N70, N144

N70

The N70 superbubble exhibits an obvious shell and a hollow interior, with the central OB association particularly dominating the ISRF in subregions 1, 2, 3, 9, and 10 (Figure 5.6). The SED flux is well-behaved compared to the other regions; fluxes generally decrease radially in each band, with the continuum bands decreasing slightly faster than PAH bands.

There are no obvious groupings in the CCDs (Figure 5.6c and 5.6d), though subregions 6 and 20 especially show signs of decreased PAH. However, these two subregions lie on the limb-brightened superbubble shell; at these locations there is increased emission at 4.5 μm (which is evident in Figure 5.2), possibly due to the Brα line incident in this band. Outside of the superbubble, however, the CCDs and `DustEM` fits show an increase in PAH emission for subregions 28 and 29, which are superimposed on CO and a small H I concentration. The central molecular cloud, however, does not show an increase in PAH emission, but the radiation is high at this location.

While other regions have `DustEM` ISRF fits similar to the ISRF as determined by stars, the ISRF com-

parison is quite different in N70. This disparity may be due to the fact that stars are centralized in the superbubble, but the sampled subregions show all dust within the line of sight. As opposed to the other H II regions, dust emission for N70 is likely coming from the shell and not the central region. Thus, a uniform distribution of dust along the hollow shell may explain why we do not see strong radial dependence on PAH or VSG.

N144

N144 is a young supperbubble containing more massive stars than N70. Of the four regions, it is the only one declared optically thin by Pellegrini et al. (2012), although N70 is optically thin at most locations as well. Indeed, N144 contains more massive stars (by number and mass) than any of our analyzed regions. Figure 5.7a-b indicates a much higher radiation field, as compared to other regions, throughout all sampled subregions. Though massive stars are located throughout N144, their concentration peaks toward the center. Subregion 1 contains a massive YSO (Gruendl & Chu 2009) which dominates *Spitzer* emission in all bands. Large-scale molecular clouds are found throughout N144, with the main clouds located toward the northwest and the south (Figure 5.7a).

As indicated on the CCD in Figure 5.7d, subregions 13, 14, 25, 26, and 27 all have minimal fractional PAH emission. These subregions are located toward optically thin locations and, other than subregion 27, are outside molecular clouds. To the west, subregions 4-9 show the most fractional PAH emission, likely due to the presence of a molecular cloud (the 8 μm band indicates that subregions 7-9 are likely still in the molecular cloud) and a reduced radiation field. Subregions 2 and 3 show a fractional PAH emission transition toward that of subregions 4-9. In the south cut, subregions deepest in the molecular cloud (29-31) have the most fractional PAH emission, with subregion 28 showing a transition from subregions 25-27.

`DUSTEM` fits affirm a steady increase in PAH mass fraction in the south and west toward molecular clouds. Subregions 18-20 indicate the highest fitted PAH mass fractions, and we note that if we use lower contours in Figure 5.7a, there is large-scale molecular gas at these locations as well.

Fits of the Y_{VSG}/Y_{BG} fraction is found to be the highest at the center, with a steady decrease toward the outer subregions. However, this decrease in Y_{VSG}/Y_{BG} is not true for the eastern cut, where the fraction increases. The eastern cut is likely encountering an optically thin region (lacking [S II]/Hα enhancement), which may be responsible for an increase in the VSG population.

5.5.3 Molecular Clouds and PAHs

As seen in N180 and N144, radially from the central OB association, the most obvious parameter that changes is the PAH mass fraction due to the presence of a (giant) molecular cloud. In order to further test if such features are genuine, we picked a molecular cloud to the northwest of N180 that is not associated with photoionized gas (i.e., no Hα emission, Figure 5.5a). The subregions in this molecular cloud are plotted as red points in the CCDs of N180 (Figure 5.5c-d). These red points are in the same vicinity in the CCD as subregions 8-13 in N180, indicating a similar composition of PAH mass fraction in both molecular clouds.

Even on the outskirts of this northwest cloud, the red points stay in the same general vicinity in the CCD; however, N180 subregions 5-7 show transitory colors between the central OB association and the molecular cloud. For this northwest cloud, it is possible that PAHs are only excited on the surface of the cloud due to starlight and thus are not modified radially. N180, on the other hand, has coexistence of molecular gas and ionized gas, and intense radiation fields break down the PAHs. Thus, the destruction of PAHs by OB stars is likely to lead to changes in PAHs radially throughout an H II region.

5.6 Discussion

We have used model fits to spatially resolved SEDs of two classical and two superbubble H II regions to determine the dust composition and properties with respect to the radiation field. In this section we discuss the individual dust components and compare the dust properties in differing H II regions and SNRs.

5.6.1 Dust

PAHs

Radiation is needed to excite PAHs; however, PAHs also can be destroyed in the presence of a strong radiation field (e.g., Madden et al. 2006; Lebouteiller et al. 2007), primarily due to high energy photons (e.g., Aitken & Roche 1985; Voit 1992). Moreover, the location of PAH and H_2 emission are strongly correlated in cool-PDRs, such as the filaments in the Horsehead Nebula (Habart et al. 2005; Compiègne et al. 2007) and ρ Ophiuchus (Habart et al. 2003). However, the locations become anti-correlated with higher radiation field, as seen in the Orion bar (Tielens et al. 1993) and in Monocerous R2 (Berné et al. 2009).

The results in this paper are consistent with these studies. We find that PAH emission is enhanced toward locations of molecular clouds except where the radiation is high. We also find that PAH emission diminished at locations that are optically thin to UV radiation

Since our regions are relatively young (no known SNRs in N144 and N180, one known in N63, and a history of one or multiple in N70), the radiation field is dominated by massive stars that produce harsh photons. Although high energy photons are the main mechanism for destroying PAHs rather than the radiation field, we will assume that the stellar content of the regions follow the same initial mass function and have similar spectral shape in their radiation field and attempt to provide an estimate of the typical U required for significant PAH destruction. For our subregions, we find that at locations where the radiation field as ascertained by massive stars is above $U \approx 30$, PAHs are no longer coincident with CO molecular gas. Our calculations of the radiation field may be highly uncertain since they can be quite dissimilar (sometimes by about an order of magnitude) to the fitted results. However, the fitted results of U are typically below those of the massive stars, so $U \approx 30$ is a fair estimate of an upper limit of the typical radiation field needed to destroy PAHs in molecular clouds. Results in Galametz et al. (2013) indicated a value consistent with ours; the modeled radiation field in the classical H II region N159 in the LMC has a drastic depletion in the fraction of PAHs for $U \gtrsim 100$.

VSGs and BGs

In all of our H II regions except N70 (whose dust is uniformly distributed about its shell), $Y_{\rm VSG}/Y_{\rm BG}$ is highest at locations where the radiation field is the strongest, as evident in Figure 5.9. However, we stress that the VSG population is highly dependent on each SED's 24 μm excess and is typically anti-correlated with the BG population.

Grain populations typically change due to both destruction (i.e., dust changes back to gas) or disruption (large grains break into smaller grains). Jones et al. (1996) showed that fast shocks (>150 km s^{-1}) likely destroy grains via sputtering, while the velocity requirement for shattering BGs with VSGs depends on the dust species, with velocities ranging from ∼1-3 km s^{-1}. In our regions, dust-dust collisions are probably uncommon due to low-densities ($n_H \sim 100$ cm^{-3}). However, O-stars are known to have wind-blown bubbles expanding at velocities of 10-15 km s^{-1} (with observations of such bubbles in N180, Nazé et al. 2001), which could lead to grain shattering.

Other possibilities of an increased $Y_{\rm VSG}$ include dust coagulation and dust erosion. Dust coagulation of the smallest grains into slightly larger VSGs could increase the 24 μm emission, but the dust in our regions are not in environments conducive to coagulation (see, e.g., Köhler et al. 2012). However, Bernard et al. (2008) suggested erosion of BGs into VSGs likely explains the LMC's 70 μm excess in neutral/ionized regions. Moreover, dust erosion is thought to be increased during star formation due to increased dust processing (Paradis et al. 2011). The central OB associations of our H II regions have a rich history of

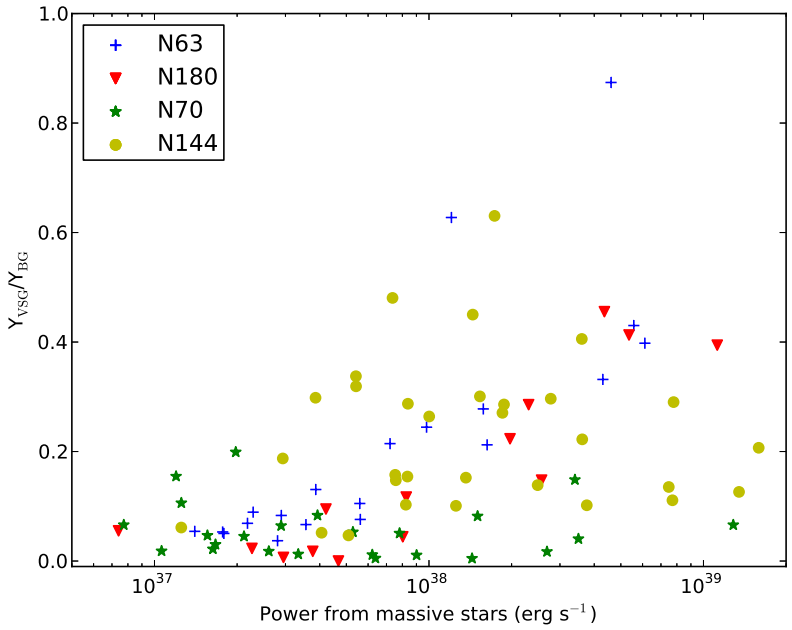

Figure 5.9 $Y_{\rm VSG}/Y_{\rm BG}$ versus the ISRF as calculated by massive stars for all 4 regions.

previous star formation, which could certainly lead to more dust processing/erosion than the areas analyzed at the macro-scale (several 100 pc; Bernard et al. 2008), leading to the increased 24 μm emission. Thus, at scales of $\sim$10 pc, BGs near OB associations may have gone through substantial erosion that has caused this increase of VSGs.

On the other hand, Pilleri et al. (2012) saw a definite decrease of "evaporating" VSGs (eVSGs) with increasing radiation field. The sources they analyzed typically had a higher radiation field ($U \gtrsim 100$) than our regions, though we still see an increase in VSGs from $U = 100$ to $U = 1000$. However, their dust model of VSGs follows more closely to the smallest grains of Li & Draine (2001) while ours follows Désert et al. (1990). Since Pilleri et al. (2012) used VSGs that are more similar to PAHs and thus have an emission spectrum at much shorter wavelengths, these eVSGs are not comparable to the VSGs modeled in this paper.

5.6.2 Dust Properties of Evolved H II Regions

We find that N70, the most evolved H II region, likely has its dust mass located in the shell. However, major differences in dust properties between classical H II regions and superbubbles are not obvious with this small sample size. Relaño et al. (2013) analyzes the SEDs of 119 H II regions in M33, categorizing them in a likely evolutionary sequence (filled, mixed, shell, and clear shell morphologies). They found that each category had similar SED features, though differed slightly between each classification. Specifically, they found that the FIR peak is located at longer wavelengths for older regions (shells and clear shells), indicating that colder

dust is likely present. Uniform cold dust temperatures are expected since gas has been pushed far away from the central heating source. This result is consistent with our analysis of N70, which shows a uniform, low fraction of Y_{VSG}/Y_{BG} compared to our less evolved H II regions that do not have the same shell geometry.

5.6.3 Comparison to SNR Studies

Changes in dust populations are commonly studied in SNRs due to their dynamic properties. Fast shocks ($\gtrsim$ 150 km s^{-1}) allow dust to reach high velocities that may cause their destruction via catastrophic shattering or sputtering (e.g., Jones et al. 1996; Micelotta et al. 2010), though VSGs and PAHs can also be created through low-velocity shattering (Jones et al. 1996). While PAHs can survive or even be produced in slow shocks, fast shocks are generally considered to destroy all PAHs in a region, except in circumstances where they can be recreated or protected by their environment (e.g., Micelotta et al. 2010; Seok et al. 2012). Additionally, harsh photons provide another mechanism of destroying the smallest grains; the radiation field in SNRs can vary drastically, though it is typically about 10-100 times the local ISRF (e.g., Andersen et al. 2011). With these different mechanisms for creation and destruction of dust, it is important to observe and model a wide range of SNRs with different shock velocities, densities, and radiation fields to test theoretical models. Moreover, dust properties of SNRs can be compared to our H II regions to provide a diagnostic of how dust changes in varying radiation fields in the absence of large shock velocities.

The *Spitzer* IR Spectrograph (IRS) has been used to study a large number of SNRs. Dust produced in supernova ejecta has been detected in young (<300 yr) SNRs (Rho et al. 2009), and PAHs are detected in SNRs (e.g., Tappe et al. 2006). Using a large spectral survey of 14 Galactic SNRs, Andersen et al. (2011) used `DustEM` (also using the Désert et al. 1990 dust models) to model the contributions of emission from BGs, VSGs, and PAHs. They found that the ratio of VSGs to BGs is 2-3 times larger in SNRs than the plane of the Galaxy, and they attribute dust shattering as the mechanism for creating the surplus of VSGs. Two of the 14 SNRs had relatively high radiation fields; fits of these regions had relatively low PAHs and virtually no VSGs. Andersen et al. (2011) suggested that these regions have high shock velocities and low densities, which can lead to destruction of VSGs and PAHs through sputtering.

With high radiation, we find that the VSG population can increase and PAHs are generally destroyed; however, fast shocks can destroy both grains. Unlike SNR regions, we find that VSG population increases where there is higher U, and there are no known fast shocks in our regions. The only region of ours that has had a history of multiple SNRs is N70, where we find a uniform, low abundance of VSG. It is possible that a past history of fast shocks has destroyed the population of VSG, and no mechanism has been available for creation of new VSGs (due to, e.g., the lack of centrally located gas since it has been blown away).

5.7 Summary

This paper is the first to examine radial SEDs on small scales (∼10 pc) across H II regions (of size-scales of 100-200 pc) in the LMC in order to evaluate the changes of dust properties due to massive stars.

We selected two classical H II regions (N63 and N180) and two superbubbles (N70 and N144). From the massive stellar population, we approximated the radiation field throughout each region. SEDs were constructed using the 7 *Spitzer* bands from the LMC (4 IRAC and 3 MIPS bands). We used CCDs and `DustEM` modeling to analyze the changes in SEDs radially throughout each H II region. The changes in the SEDs were then compared to the radiation field in order to gauge the effect of massive stars on dust properties.

Our main results are as follows:

1) We find that the PAH mass fraction increases significantly toward molecular clouds except when there is a very strong radiation field. PAHs are likely being destroyed by the radiation field (in areas with $U \gtrsim 30$), and we typically detect the PAH mass fraction increase as we leave the central OB association. As expected, optically thin areas in our H II regions also have a diminished PAH mass fraction.

2) The VSG mass fraction increases at locations of an enhanced radiation field. Expanding bubbles may be launching dust at velocities that can cause BGs to shatter into VSGs. Dust erosion of larger grains into VSGs is another possible mechanism for the enhanced 24 μm emission.

Images from the NASA/ESA Hubble Space Telescope were obtained from the data archive at the Space Telescope Science Institute. STScI is operated by the Association of Universities for Research in Astronomy, Inc. under NASA contract NAS 5-26555. This research has made use of the SIMBAD database, operated at CDS, Strasbourg, France. This research has also made use of the NASA/IPAC Infrared Science Archive, which is operated by the Jet Propulsion Laboratory, California Institute of Technology, under contract with the National Aeronautics and Space Administration.

Chapter 6

Conclusions

Presented in this thesis are diverse studies of environmental consequences of stars. Most of this dissertation focuses on the early stages of the stars life – from molecular clouds to main sequence. The discussion and/or summary for each chapter is repeated here.

6.1 The Galactic Magnetic Field's Effect in Star-Forming Regions

We have used Hertz (Dotson et al. 2010) polarization measurements in dense, star-forming clouds, to investigate whether the ordered component of the magnetic field in these clouds is correlated with location in the Galaxy. In order to obtain a single polarization percentage, angle, and intensity for each of the 52 Hertz objects (as well as the 22 complexes), the polarization information for each beam was combined into a large-scale average. With each object represented by these values, correlations with respect to location in the Galaxy (both by Galactic coordinates and spiral arm locations) were investigated.

There are three primary results for this paper.

- A meaningful polarization angle can be determined for most objects and complexes.
- No evidence was found in our data for a correlation between the polarization angle and location within the galaxy.
- The polarization angle for an object or a complex on the sky is consistent with a random distribution.

The fact that a meaningful mean direction can be identified for the magnetic field in most objects implies the existence of an ordered, large scale component of the field *within* the dense, star-forming clouds we have studied. This is consistent with the continuity of magnetic field direction on different scales within these clouds, discussed by Li et al. (2009). However, since these are star-forming clouds, feedback processes from newly formed stars can generate appreciable scatter in the magnetic field directions within each object. This may be, in part, the source of the observed angle dispersion within each data set.

We have found that there is no significant evidence for the existence of any correlation between mean polarization angle and location, which is consistent with the results by Glenn et al. (1999, see Section 2.1). The fact that objects do not seem to avoid polarization angles aligned with the Galaxy's magnetic field implies that the polarization angles detected are almost entirely created by the analyzed object rather than a large-scale, external field. This suggests that complexes as a whole may become their own dynamical system that is separate from the Galaxy. The results in this paper imply that cloud cores usually have a meaningful net field (which may correlate with other cores in the same complex; Li et al. 2009) that has no preferred direction within the Galaxy, yet are embedded in a diffuse medium in an ordered, Galactic large-scale field.

Fish et al. (2003) did a similar analysis as this paper, but with a different methodology. They analyzed the line-of-sight magnetic fields through Zeeman splitting of OH masers in massive star-forming regions; on sub-kiloparsec scales (about 0.5 kpc), two sources often had opposite line-of-sight field directions, suggesting that multiple cores in a complex tangle the magnetic fields. In some areas of the Galaxy, Fish et al. found some line-of-sight field alignment in parts of the Sagittarius arm and Norma arm on scales of about 2 kpc. Still, they also found no evidence for correlations of magnetic field directions in star-forming regions with the Galactic field or with the spiral arms on larger scales.

The cloud formation process involves instabilities on Galactic scales (Shetty & Ostriker 2008; Mouschovias et al. 2009; Tasker & Tan 2009), which are responsible for the accumulation of enough mass to form the clouds. At the same time, these instabilities generate turbulence in the interstellar medium of the Galaxy. The cloud magnetic field is thus expected to decouple from the Galactic field during the cloud formation process. Stellar feedback is an additional mechanism driving the cloud magnetic field away from alignment with the Galactic field direction. These effects are likely responsible for the dichotomy between the arm/interarm regions in terms of the ratio of strengths between the ordered and tangled components of the magnetic field observed in external galaxies (Beck 2005).

6.2 The Magnetic Field Morphology of the Class 0 Protostar L1157-mm

In this letter we present the first detection of magnetic fields in L1157-mm at two different wavelengths. Our main results are:

- We find the second instance of a full hourglass morphology in the inferred magnetic field around a low-mass protostar. This is also only the second instance around a Class 0 source. The axis of the hourglass

is nearly aligned with the axis of the outflow, with the full detection of the hourglass occurring at a resolution of ∼550 AU.

- The angle of the central magnetic field vector agrees at 350 μm and 1.3 mm and at all size-scales.
- We used two methods to calculate the plane-of-sky magnetic field throughout the central region and find values of 1.4 and 3.4 mG.

While this particular hourglass is nearly aligned with the outflow, the TADPOL survey results have shown that in general, magnetic field lines are consistent with being preferentially misaligned (perpendicular) or randomly aligned with respect to outflows (Hull et al. 2013).

The first well-defined hourglass morphology around a low-mass protostar was observed in 1997 in the Class 0 binary system NGC 1333 IRAS 4A (Girart et al. 1999); such a discovery has not been published since. Our observation of L1157-mm is arguably the best example of an hourglass shape in any star formation region to date. Characterizing such systems is an important step to better understand the role of magnetic fields in star formation.

IRAS 4A's hourglass axis of symmetry is misaligned with large scale outflow as measured by CO(3-2) (Blake et al. 1995) by 16° and is over 40° misaligned with the small scale outflow as measured by SiO(1-0) (Choi 2005). However, SHARP observations found that the large scale field in IRAS 4A coincides within 1° of the large scale outflow (Attard et al. 2009). Our observations of L1157-mm find that the hourglass axis of symmetry and northwest SHARP vectors are similarly misaligned by ∼15-30°, but the hourglass axis is more aligned with the outflow than these SHARP vectors. These results suggest the need to compare more polarimetric observations at different resolutions, which will be a future TADPOL project.

Recent high resolution Expanded Very Large Array observations detect only a single continuum source at size scales of ∼12 AU (J. J. Tobin 2013, private communication), suggesting that L1157-mm is most likely a single source. Perhaps cores with a single system are more likely to yield an hourglass detection and/or an hourglass axis aligned with the outflow.

6.3 Surveying HII Regions of Modeled Young Stellar Objects in the Large Magellanic Cloud

We have conducted a survey of free-free emission around 102 spectroscopically confirmed massive YSOs and found H II regions around 54 of the sources. We compare *Spitzer* spectral features, including estimates from

spectroscopic modeling, to measured quantities from the free-free emission. Our main results are summarized below.

- Almost all YSOs that have enough ionizing flux to produce a detectable H II regions indeed have an H II region. Moreover, masses estimated from Robitaille et al. (2007) models appear to be fairly accurate. Since mass correlates with most observed parameters, it is a crucial consideration when exploring correlations in almost any other relationship.

- The measured parameters (e.g., densities) of these regions are indicative of "dense" H II regions, though they may be harboring UC H II regions.

- More embedded (likely younger) sources are denser and less likely to be resolved, indicating evolving H II regions.

- We have found relationships between *Spitzer* spectra and continuum fluxes. Though a power-law is certainly not a perfect fit, an approximate free-free emission and mass relationship is $F_\nu \propto M^3$. There is a large spread in the data, and sources that lack emission lines in their spectra typically have lower fluxes, while some sources with emission lines have fluxes that are significantly higher than expected.

- H II regions about YSOs are likely better modeled as prolate spheroids. However, spherical geometry still provides reasonable estimates of the parameters of the region.

- The sources with the highest silicate PCA strength (and likely younger sources) tend to be unresolved and denser, indicating that these H II regions take time to evolve. We also see that massive sources are also less likely to be resolved. Since most sources with high PCA strength tend to be massive, mass may be a factor as much as age for the size of the H II region.

- More massive YSOs tend to be in denser environments, with a relationship of about $n_e \propto M^{2.3}$.

- We find the typical relationship between density and size of $n_e \propto D^{-1}$, though due to the spread of our data, we caution the relationship. The spread in the relationship is primarily due to sampling a large range of ionizing fluxes.

- YSO H II regions have ages $\geq 10^5$ yr, consistent with the extended regions of KK01. Since it is plausible that our H II contain more compact sources, our observations may be the extended subset of hierarchical structure in YSO H II regions.

6.4 Spitzer Observations of Dust Emission from HII Regions in the Large Magellanic Cloud

This paper is the first to examine radial SEDs on small scales (∼10 pc) across H II regions (of size-scales of 100-200 pc) in the LMC in order to evaluate the changes of dust properties due to massive stars.

We selected two classical H II regions (N63 and N180) and two superbubbles (N70 and N144). From the massive stellar population, we approximated the radiation field throughout each region. SEDs were constructed using the 7 *Spitzer* bands from the LMC (4 IRAC and 3 MIPS bands). We used CCDs and `DustEM` modeling to analyze the changes in SEDs radially throughout each H II region. The changes in the SEDs were then compared to the radiation field in order to gauge the effect of massive stars on dust properties.

Our main results are as follows:

1) We find that the PAH mass fraction increases significantly toward molecular clouds except when there is a very strong radiation field. PAHs are likely being destroyed by the radiation field (in areas with $U \gtrsim 30$), and we typically detect the PAH mass fraction increase as we leave the central OB association. As expected, optically thin areas in our H II regions also have a diminished PAH mass fraction.

2) The VSG mass fraction increases at locations of an enhanced radiation field. Expanding bubbles may be launching dust at velocities that can cause BGs to shatter into VSGs. Dust erosion of larger grains into VSGs is another possible mechanism for the enhanced 24 μm emission.

References

Aitken, D. K., & Roche, P. F. 1985, MNRAS, 213, 777

Allen, A., Li, Z.-Y., & Shu, F. H. 2003, ApJ, 599, 363

Attard, M., Houde, M., Novak, G., et al. 2009, ApJ, 702, 1584

Andersen, M., Rho, J., Reach, W. T., Hewitt, J. W., & Bernard, J. P. 2011, ApJ, 742, 7

Anthony-Twarog, B. J. 1982, AJ, 87, 1213

Arthur, S. J., Kurtz, S. E., Franco, J., & Albarrán, M. Y. 2004, ApJ, 608, 282

Bachiller, R., Pérez Gutiérrez, M., Kumar, M. S. N., & Tafalla, M. 2001, A&A, 372, 899

Beck, R. 2005, Magnetic Fields in the Universe: From Laboratory and Stars to Primordial Structures., 784, 343

Beck, R. 2007, EAS Publ. Ser. 23, 19

Bernard, J.-P., Reach, W. T., Paradis, D., et al. 2008, AJ, 136, 919

Berné, O., Fuente, A., Goicoechea, J. R., et al. 2009, ApJ, 706, L160

Blake, G. A., Sandell, G., van Dishoeck, E. F., et al. 1995, ApJ, 441, 689

Calzetti, D., Wu, S.-Y., Hong, S., et al. 2010, ApJ, 714, 1256

Campbell, M. F., Niles, D., Nawfel, R., Hawrylycz, M., Hoffmann, W. F., & Thronson, H. A., Jr. 1982, ApJ, 261, 550

Caulet, A., & Williams, R. M. 2012, ApJ, 761, 107

Chandrasekhar, S., & Fermi, E. 1953, ApJ, 118, 113

Chapman, N. L., Davidson, J. A., Goldsmith, P. F., et al. 2013, ApJ, 770, 151

Chiang, H.-F., Looney, L. W., & Tobin, J. J. 2012, ApJ, 756, 168

Chiang, H.-F., Looney, L. W., Tobin, J. J., & Hartmann, L. 2010, ApJ, 709, 470

Choi, M. 2005, ApJ, 630, 976

Chu, Y.-H. 1997, AJ, 113, 1815

Chu, Y.-H., & Mac Low, M.-M. 1990, ApJ, 365, 510

Churchwell, E., Whitney, B. A., Babler, B. L., et al. 2004, ApJS, 154, 322

Compiègne, M., Abergel, A., Verstraete, L., et al. 2007, A&A, 471, 205

Compiègne, M., Flagey, N., Noriega-Crespo, A., et al. 2010, ApJ, 724, L44

Compiègne, M., Verstraete, L., Jones, A., et al. 2011, A&A, 525, A103

Condon, J. J. 1992, ARA&A, 30, 575

Cox, A. N. (ed.) 2000, Allen's Astrophysical Quantities (New York: Springer)

Crutcher, R. M. 1999, ApJ, 520, 706

Crutcher, R. M. 2012, ARA&A, 50, 29

Crutcher, R., Heiles, C., & Troland, T. 2003, in Turbulence and Magnetic Fields in Astrophysics, ed. E. Falgarone & T. Passot (Lecture Notes in Physics, Vol. 614; Berlin: Springer), 155

Dame, T. M., & Thaddeus, P. 1985, ApJ, 297, 751

Davies, R. D., Elliott, K. H., & Meaburn, J. 1976, MmRAS, 81, 89

Davis, L. J., & Greenstein, J. L. 1951, ApJ, 114, 206

De Buizer, J. M., & Vacca, W. D. 2010, AJ, 140, 196

de Jager, C., & Nieuwenhuijzen, H. 1987, A&A, 177, 217

de Zeeuw, P. T., Hoogerwerf, R., de Bruijne, J. H. J., Brown, A. G. A., & Blaauw, A. 1999, AJ, 117, 354

Désert, F.-X., Boulanger, F., & Puget, J. L. 1990, A&A, 237, 215

Dopita, M. A., Fischera, J., Crowley, O., et al. 2006, ApJ, 639, 788

Draine, B. T. 2011, ApJ, 732, 100

Draine, B. T., & Li, A. 2007, ApJ, 657, 810

Dotson, J. L., Vaillancourt, J. E., Kirby, L., Hildebrand, R. H., & Davidson, J.A. 2010, ApJS, 186, 406

Eritsian, M. H. & Pogossian, H. M. 1996, Astrophysics, 39, 327

Feast, M. 1999, New Views of the Magellanic Clouds, 190, 542

Franco, J., Kurtz, S. E., García-Segura, G., & Hofner, P. 2000, Ap&SS, 272, 169

Fish, V. L., Reid, M. J., Argon, A. L., & Menten, K. M. 2003, ApJ, 596, 328

Fiedler, R. A., & Mouschovias, T. C. 1993, ApJ, 415, 680

Flagey, N., Boulanger, F., Verstraete, L., et al. 2006, A&A, 453, 969

Fosalba, P., Lazarian, A., Prunet, S., & Tauber, J.A., 2002, ApJ, 564, 762

Fukui, Y., Kawamura, A., Minamidani, T., et al. 2008, ApJS, 178, 56

Galametz, M., Hony, S., Galliano, F., et al. 2013, MNRAS, 431, 1596

Galli, D., & Shu, F. H. 1993, ApJ, 417, 243

Garay, G., & Lizano, S. 1999, PASP, 111, 1049

Garmany, C. D., Massey, P., & Parker, J. W. 1994, AJ, 108, 1256

Gruendl, R. A., & Chu, Y.-H. 2009, ApJS, 184, 172

Genzel, R., et al. 1981, ApJ, 247, 1039

Girart, J. M., Beltrán, M. T., Zhang, Q., Rao, R., & Estalella, R. 2009, Science, 324, 1408

Girart, J. M., Crutcher, R. M., & Rao, R. 1999, ApJ, 525, L109

Girart, J. M., Rao, R., & Marrone, D. P. 2006, Science, 313, 812

Glenn, J., Walker, C. K., & Young, E. T. 1999, ApJ, 511, 812

Gorjian, V., Werner, M. W., Mould, J. R., et al. 2004, ApJS, 154, 275

Gruendl, R. A., & Chu, Y.-H. 2009, ApJS, 184, 172

Gwinn, C. R., Moran, J. M., & Reid, M. J. 1992, ApJ, 393, 149

Habart, E., Boulanger, F., Verstraete, L., et al. 2003, A&A, 397, 623

Habart, E., Abergel, A., Walmsley, C. M., Teyssier, D., & Pety, J. 2005, A&A, 437, 177

Habets, G. M. H. J., & Heintze, J. R. W. 1981, A&AS, 46, 193

Habing, H. J., & Israel, F. P. 1979, ARA&A, 17, 345

Han, J. L., Manchester, R. N., Lyne, A. G., Qiao, G. J., & van Straten, W. 2006, ApJ, 642, 868

Heiles, C. 2000, AJ, 119, 923

Helfand, D. J., Gotthelf, E. V., Halpern, J. P., Camilo, F., Semler, D. R., Becker, R. H., & White, R. L. 2007, ApJ, 665, 1297

Henize, K. G. 1956, ApJS, 2, 315

Herbst, W., & Racine, R. 1976, AJ, 81, 840

Hildebrand, R.H. 1988, Astrophys. Lett. Commun., 26, 275

Hinshaw, B., et al. 2009, ApJ, 180, 225

Imai, H., et al. 2007, PASJ, 59, 1107

Hull, C. L. H., Plambeck, R. L., Bolatto, A. D., et al. 2013, ApJ, 768, 159

Hunt, L. K., & Hirashita, H. 2009, A&A, 507, 1327

Indebetouw, R., Johnson, K. E., & Conti, P. 2004, AJ, 128, 2206 (IJC04)

Johnson, H. L., & Morgan, W. W. 1953, ApJ, 117, 313

Johnson, H. L. 1966, ARA&A, 4, 193

Jones, A. P., Tielens, A. G. G. M., & Hollenbach, D. J. 1996, ApJ, 469, 740

Kennicutt, R. C., Jr., & Hodge, P. W. 1986, ApJ, 306, 130

Kenyon, S. J., Dobrzycka, D., & Hartmann, L. 1994, AJ, 108, 1872

Kim, K.-T., & Koo, B.-C. 2001, ApJ, 549, 979 (KK01)

Klare, G. & Neckel, T. 1977, A&AS, 27, 215

Koch, P. M., Tang, Y.-W., & Ho, P. T. P. 2012, ApJ, 747, 79

Köhler, M., Stepnik, B., Jones, A. P., et al. 2012, A&A, 548, A61

Kun, M. 1998, ApJS, 115, 59

Kurtz, S. 2005, Massive Star Birth: A Crossroads of Astrophysics, 227, 111

Kurtz, S., Churchwell, E., & Wood, D. O. S. 1994, ApJS, 91, 659

Kurtz, S. E., Watson, A. M., Hofner, P., & Otte, B. 1999, ApJ, 514, 232

Kwon, W., Looney, L. W., Crutcher, R. M., & Kirk, J. M. 2006, ApJ, 653, 1358

Launhardt, R., & Henning, T. 1997, A&A, 326, 329

Lawton, B., Gordon, K. D., Babler, B., et al. 2010, ApJ, 716, 453

Lazarian, A. 2007, J. Quant. Spec. Radiat. Transf., 106, 225

Lebouteiller, V., Brandl, B., Bernard-Salas, J., Devost, D., & Houck, J. R. 2007, ApJ, 665, 390

Lejeune, T., & Schaerer, D. 2001, A&A, 366, 538

Li, A., & Draine, B. T. 2001, ApJ, 554, 778

Li, H., Dowell, C. D., Goodman, A., Hildebrand, R., & Novak, G. 2009, ApJ, 704, 891

Li, H., Dowell, C. D., Kirby, L., Novak, G., & Vaillancourt, J. E. 2008, ApOpt, 47, 422

Li, H., Griffin, G. S., Krejny, M., Novak, G., Loewenstein, R. F., Newcomb, M. G., Calisse, P. G., & Chuss, D. T. 2006, ApJ, 648, 340

Loinard, L. 2012, in IAU Symp. 289, Advancing the Physics of Cosmic Distances, ed. R. de Gris & G. Bono (Cambridge: Cambridge Univ. Press), 36

Looney, L. W., Tobin, J. J., & Kwon, W. 2007, ApJ, 670, L131

Lucke, P. B., & Hodge, P. W. 1970, AJ, 75, 171

Madden, S. C., Galliano, F., Jones, A. P., & Sauvage, M. 2006, A&A, 446, 877

Madore, B. F. 1982, ApJ, 253, 575

Mamajek, E. E. 2008, Astron. Nachr., 329, 10

Martín-Hernández, N. L., Vermeij, R., & van der Hulst, J. M. 2005, A&A, 433, 205

Martins, F., Schaerer, D., & Hillier, D. J. 2005, A&A, 436, 1049

Massey, P. 1993, Massive Stars: Their Lives in the Interstellar Medium, 35, 168

Massey, P., Garmany, C. D., Silkey, M., & Degioia-Eastwood, K. 1989, AJ, 97, 107

Mathewson, D. S., & Ford, V. L. 1970, MmRAS, 74, 139

Mathewson, D. S., Ford, V. L., Dopita, M. A., et al. 1983, ApJS, 51, 345

Mathis, J. S., Mezger, P. G., & Panagia, N. 1983, A&A, 128, 212

Matthews, B. C., McPhee, C. A., Fissel, L. M., & Curran, R. L. 2009, ApJS, 182, 143

McKee, C. F. & Ostriker, E. C. 2007, ARA&A, 45, 565

Meixner, M., et al. 2006, AJ, 132, 2268

Menten, K. M., Reid, M. J., Forbrich, J., & Brunthaler, A. 2007, A&A, 474, 515

Mezger, P. G., & Henderson, A. P. 1967, ApJ, 147, 471

Micelotta, E. R., Jones, A. P., & Tielens, A. G. G. M. 2010, A&A, 510, A36

Miville-Deschênes, M. A. & Lagache, G. 2005, ApJS, 157, 302

Moffat, A. F. J., Jackson, P. D., & Fitzgerald, M. P., 1979, A&AS, 38, 197

Mouschovias, T. C., & Ciolek, G. E. 1999, in NATO ASIC Proc. 540, The Origin of Stars and Planetary Systems, ed. C. J. Lada & N. D. Kylafis (Dordrecht: Kluwer), 305 Proc. 540, The Origin of Stars and Planetary Systems, ed. C. J. Lada & N. D. Kylafis, 305

Mouschovias, T. C., Kunz, M. W., & Christie, D. A. 2009, MNRAS, 397, 14

Nazé, Y., Chu, Y.-H., Points, S. D., et al. 2001, AJ, 122, 921

Neckel, T. 1978, A&A, 69, 5 1993, ApJ, 405, 706

Odenwald S. F., & Schwartz P. R, 1993, ApJ, 405, 706

Oey, M. S. 1996, ApJ, 465, 231

Ossenkopf, V., & Henning, T. 1994, A&A, 291, 943

Ostriker, E. C., Stone, J. M., & Gammie, C. F. 2001, ApJ, 546, 980

Panagia, N. 1973, AJ, 78, 929

Panagia, N., & Walmsley, C. M. 1978, A&A, 70, 411

Paradis, D., Reach, W. T., Bernard, J.-P., et al. 2011, AJ, 141, 43

Park, B.-G., & Sung, H. 2002, AJ, 123, 892

Pellegrini, E. W., Oey, M. S., Winkler, P. F., et al. 2012, ApJ, 755, 40

Peters, T., Banerjee, R., Klessen, R. S., et al. 2010, ApJ, 711, 1017

Peters, T., Mac Low, M.-M., Banerjee, R., Klessen, R. S., & Dullemond, C. P. 2010, ApJ, 719, 831

Pilleri, P., Montillaud, J., Berné, O., & Joblin, C. 2012, A&A, 542, A69

Povich, M. S., et al. 2007, ApJ, 660, 346

Rao, R., Girart, J. M., Marrone, D. P., Lai, S.-P., & Schnee, S. 2009, ApJ, 707, 921

Reach, W. T., Megeath, S. T., Cohen, M., et al. 2005, PASP, 117, 978

Reid, M., et al. 2009, ApJ, 700, 137

Relaño, M., Verley, S., Pérez, I., et al. 2013, A&A, 552, A140

Rho, J., Jarrett, T. H., Reach, W. T., Gomez, H., & Andersen, M. 2009, ApJ, 693, L39

Rieke, G. H., Blaylock, M., Decin, L., et al. 2008, AJ, 135, 2245

Robitaille, T. P., Whitney, B. A., Indebetouw, R., & Wood, K. 2007, ApJS, 169, 328

Rodriguez, L. F., Carral, P., Moran, J. M., & Ho, P. T. P. 1982, ApJ, 260, 635

Salpeter, E. E. 1955, ApJ, 121, 161

Sault, R. J., Teuben, P. J., & Wright, M. C. H. 1995, Astronomical Data Analysis Software and Systems IV, 77, 433

Schleuning, D. A. 1998, ApJ, 493, 811

Seale, J. P., Looney, L.W., Chu, Y.-H., Gruendl, R. A., Brandl, B., Rosie Chen, C.-H. R., Brandner, W., & Blake, G. A. 2009, ApJ, 699, 150 (SL09)

Seok, J. Y., Koo, B.-C., & Onaka, T. 2012, ApJ, 744, 160

Shetty, R., & Ostriker, E. C. 2008, ApJ, 684, 978

Shinnaga, H., Phillips, T. G., Furuya, R. S., & Cesaroni, R. 2008, ApJ, 682, 1103

Slater, C. T., Oey, M. S., Li, A., et al. 2011, ApJ, 732, 98

Smith, R. C., & MCELS Team 1999, IAUS No. 190, New Views of the Magellanic Clouds, 28

Smith, R. C., & MCELS Team 1999, IAUS No. 190, New Views of the Magellanic Clouds, 28

Smith, L. J., Norris, R. P. F., & Crowther, P. A. 2002, MNRAS, 337, 1309

Sofue, Y., Klein, U., Beck, R., & Wielebinski, R. 1986, Ap&SS, 119, 191

Tang, Y.-W., Ho, P. T. P., Koch, P. M., & Rao, R. 2010, ApJ, 717, 1262

Tang, Y.-W., Ho, P. T. P., Koch, P. M., et al. 2009, ApJ, 700, 251

Tappe, A., Rho, J., & Reach, W. T. 2006, ApJ, 653, 267

Tasker, E. J., & Tan, J. C. 2009, ApJ, 700, 358

Tassis, K., Dowell, C. D., Hildebrand, R. H., Kirby, L., & Vaillancourt, J. E., 2009, MNRAS, 399, 1681

Tielens, A. G. G. M., Meixner, M. M., van der Werf, P. P., et al. 1993, Science, 262, 86

Tobin, J. J., Bergin, E. A., Hartmann, L., et al. 2013, ApJ, 765, 18

Tobin, J. J., Hartmann, L., Chiang, H.-F., et al. 2012, Nature, 492, 83

Vaidya, K., Chu, Y.-H., Gruendl, R. A., Chen, C.-H. R., & Looney, L. W. 2009, ApJ, 707, 1417

Vaillancourt, J. E. 2006, PASP, 118, 1340

Vaillancourt, J. E., & Matthews, B. C. 2012, ApJS, 201, 13

van der Marel, R. P., & Cioni, M.-R. L. 2001, AJ, 122, 1807

van Hoof, P. A. M. 2000, MNRAS, 314, 99

Voit, G. M. 1992, MNRAS, 258, 841

Walker, M. F. 1956, ApJS, 2, 365

Walsh, A. J., Hyland, A. R., Robinson, G., & Burton, M. G. 1997, MNRAS, 291, 261

Warren, J. S., Hughes, J. P., & Slane, P. O. 2003, ApJ, 583, 260

Wilson, T.L., Mezger, P.G., Gardner, F.F., & Milne, D.K., 1970, A&A, 6, 364

Wink, J. E., Wilson, T. L., & Bieging, J. H. 1983, ApJ, 127, 211

Wong, T., Hughes, A., Ott, J., et al. 2011, ApJS, 197, 16

Wood, D. O. S., & Churchwell, E. 1989a, ApJS, 69, 831 (WC89)

Wood, D. O. S., & Churchwell, E. 1989b, ApJ, 340, 265

Xu, Y., Reid, M.J., Zheng, X.W., & Menten, K.M. 2006, Science, 311, 54

Zaritsky, D., Harris, J., Thompson, I. B., & Grebel, E. K. 2004, AJ, 128, 1606

Zinnecker, H., & Yorke, H. W. 2007, ARA&A, 45, 481